

Dissertation  
submitted to the  
Combined Faculties for the Natural Sciences and for Mathematics  
of the Ruperto-Carola University of Heidelberg, Germany,  
for the degree of  
Doctor of Natural Sciences

presented by

Diplom-Physiker : Gati, Rudolf  
Born in : Budapest, Hungary  
Oral examination : the 16<sup>th</sup> of May 2007



**Bose-Einstein Condensates**  
**in a Single**  
**Double Well Potential**

**Referees: Prof. Dr. Markus K. Oberthaler**

**PD Dr. Thomas Gasenzer**



## **Bose-Einstein Kondensate in einem einzelnen Doppelmuldenpotential**

In der vorliegenden Arbeit werden die experimentelle Realisierung eines einzelnen bosonischen Josephsonkontaktes beschrieben und die damit durchgeführten Untersuchungen diskutiert. Um diesen neuartigen Josephsonkontakt zu erzeugen, wird ein 87-Rubidium Bose-Einstein Kondensat in einem Doppelmuldenpotential in zwei Materiewellenpakete zerteilt, welche durch das quantenmechanische Tunneln der Atome durch die Barriere miteinander kohärent gekoppelt sind. Der Zustand des Systems lässt sich mit Hilfe zweier dynamischer Variablen charakterisieren, dem Besetzungszahlunterschied der beiden Mulden und dem Phasenunterschied zwischen ihnen. Die Untersuchung des dynamischen Verhaltens des Josephsonkontaktes zeigt, dass zwei deutlich voneinander getrennte Regime existieren, das Plasma-Oszillations Regime, in welchem Teilchen aus einer Mulde in die andere und wieder zurück tunneln, und das Self Trapping Regime, in welchem die Tunneldynamik eingefroren zu sein scheint. Des Weiteren wird das Verhalten dieses Josephsonkontaktes bei verschiedenen Temperaturen betrachtet. Es zeigt sich, dass die relative Phase zwischen den zwei Materiewellenpaketen in Steady State nicht konstant Null ist, sondern je nach Temperatur und Tunnelkopplung Fluktuationen unterliegt. Durch das Messen der Fluktuationen bei der gleichzeitigen Kenntnis der Tunnelkopplung lässt sich die Temperatur der atomaren Wolke bestimmen. Damit ist ein neues Verfahren zur Temperaturmessung realisiert, welches auch in einem Temperaturbereich eingesetzt werden kann, in der herkömmliche Methoden keine sinnvollen Resultate liefern.

## **Bose-Einstein Condensates in a Single Double Well Potential**

The subject of this work is the experimental implementation of a single bosonic Josephson junction and the discussion of the performed investigations. To generate this new kind of Josephson junction a 87-Rubidium Bose-Einstein condensate is split in a double well potential into two matter wave packets, which are coupled coherently to each other via quantum mechanical tunneling of atoms through the barrier. The state of the system can be described by two dynamical variables, the population imbalance of the two wells and their phase difference. The investigation of the dynamical response of the Josephson junction shows, that two dynamical regimes can be identified, the plasma oscillation regime, where atoms tunnel back and forth between the wells, and the self trapping regime, where no tunneling is found. Furthermore, the investigation at finite temperature reveals, that the relative phase in steady state is not locked to zero but fluctuates according to its temperature and the tunneling coupling. By measuring the fluctuations and calculating the tunneling coupling it is possible to deduce the temperature of the atomic cloud. With this a new method for thermometry is realized, which also works in a regime, where the standard methods can not be applied.



---

# Contents

<b>1</b>	<b>Introduction</b>	<b>1</b>
<b>2</b>	<b>Basic theory of the Bosonic Josephson Junction</b>	<b>7</b>
2.1	The Bose-Einstein condensate . . . . .	7
2.1.1	The weakly interacting Bose gas . . . . .	8
2.1.2	Properties of Bose-Einstein condensates in a harmonic trapping potential . . . . .	9
2.1.3	Momentum distribution of a degenerate Bose gas . . . . .	11
2.1.4	Temperature measurement of a degenerate Bose gas . . . . .	13
2.2	Two mode approximation - the Bose Hubbard model . . . . .	14
2.2.1	Energy spectrum of the Bose-Hubbard Hamiltonian . . . . .	16
2.2.2	Atom number fluctuations and coherence . . . . .	17
2.2.3	Rabi, Josephson and Fock regime . . . . .	20
2.3	The phase operator . . . . .	20
2.3.1	Phase states . . . . .	23
2.3.2	Comparison of the different phase operators . . . . .	25
2.3.3	Momentum distribution in the double well . . . . .	26
2.3.4	Matter wave interference - projection onto $SU(2)$ coherent states . . . . .	28
2.4	Mean field description - a mechanical analogue . . . . .	29
2.4.1	Gross-Pitaevskii equation and the two mode model . . . . .	31
2.4.2	Properties in steady state . . . . .	33
2.4.3	Properties in steady state at finite temperature . . . . .	34
2.4.4	Dynamical properties . . . . .	35
2.5	Summary of the theoretical background . . . . .	35
<b>3</b>	<b>Experimental realization of a single bosonic Josephson junction</b>	<b>37</b>
3.1	Experimental apparatus . . . . .	38
3.1.1	Laser systems . . . . .	38
3.1.2	Laser induced potential for ultracold neutral atoms . . . . .	40
3.1.3	Ultra-stable harmonic trapping potential . . . . .	41
3.1.4	Actively stabilized periodic potential . . . . .	43
3.1.5	Double well potential . . . . .	45
3.1.6	Imaging the density distribution at small atom numbers . . . . .	47
3.2	Calibration of the experimental parameters . . . . .	49
3.2.1	Magnification . . . . .	50
3.2.2	Optical resolution . . . . .	50
3.2.3	Particle numbers . . . . .	51
3.2.4	Parameters of the harmonic trap . . . . .	51

3.2.5	Parameters of the periodic potential . . . . .	54
3.3	Experimental access to the observables . . . . .	55
3.3.1	Density distribution - population imbalance . . . . .	55
3.3.2	Momentum distribution - relative phase . . . . .	56
<b>4</b>	<b>Properties of and fluctuations in the bosonic Josephson junction in steady state</b>	<b>59</b>
4.1	Zero temperature limit . . . . .	59
4.1.1	Asymmetric double well potential . . . . .	60
4.1.2	Steady state population imbalance in the asymmetric double well . . .	60
4.2	Steady state fluctuations at finite temperature . . . . .	61
4.2.1	Low temperature limit . . . . .	62
4.2.2	High temperature limit . . . . .	62
4.2.3	Experimental observation of thermal fluctuations in steady state . . .	63
4.2.4	Thermalization and thermometry . . . . .	67
4.2.5	Application of the noise thermometer . . . . .	68
<b>5</b>	<b>Dynamical properties of the bosonic Josephson junction</b>	<b>71</b>
5.1	Dynamical regimes . . . . .	72
5.1.1	Plasma oscillations . . . . .	73
5.1.2	Self trapping . . . . .	73
5.1.3	Phase plane portrait . . . . .	74
5.1.4	$\pi$ -Phase modes . . . . .	74
5.2	Experimental observation of the dynamical response . . . . .	74
<b>6</b>	<b>Conclusions and Outlook</b>	<b>81</b>
6.1	Experimental results . . . . .	81
6.2	Outlook . . . . .	82
	<b>Appendix</b>	<b>85</b>
A	Heat Capacity close to the critical temperature . . . . .	85
B	Numerical solution of the Gross-Pitaevskii equation in 3-D . . . . .	86
C	Tunneling coupling and on-site interaction energy deduced from 3-D GPE . .	88
D	Rubidium-87 . . . . .	89
	<b>Bibliography</b>	<b>91</b>

---

# 1 Introduction

Quantum mechanics as one of the foundations of modern physics naturally incorporates the fascinating wave nature of massive particles. The existence of these matter waves was postulated in 1924 by de Broglie [1] and experimentally demonstrated in 1927 by Davisson and Germer [2]. The interference of matter waves, in analogy to the interference of photons, has been and still is the basis of many fundamental tests of quantum mechanics. But the interference of massive particles is not only interesting from a fundamental point of view, but with this technique also a wide range of applications became accessible, in particular for high precision measurements.

The application of ultracold atoms for interferometry can provide due to their short wave length (compared to electrons and neutrons) a high degree of accuracy. The first signals of atom interferometers were observed in 1991 in several groups [3, 4, 5, 6]. In the early atom interferometers a beam of cold atoms or molecules was used and the interference patterns were build up point after point, due to the interference of every particle with itself.

A completely different situation is encountered with Bose-Einstein condensates. The possibility of condensing massive bosonic particles into a single quantum mechanical state was predicted by A. Einstein in 1924 [7] based on a work of S. N. Bose on the statistical properties of photons [8]. The first experimental observation of Bose-Einstein condensation in 1995 [9, 10, 11] was made possible by the development of novel cooling techniques (laser cooling and evaporative cooling) of dilute vapors of neutral atoms.

As in Bose-Einstein condensates all particles occupy the same quantum mechanical state, they are coherent sources of matter waves in analogy to a laser for light. The interference of these coherent matter waves can be directly achieved by merging two wave packets which were initially separated in a double well trap. The first observation of the interference of two independent Bose-Einstein condensates in 1997 [12] was followed by extensive theoretical but also experimental investigations.

Due to the high coherence of Bose-Einstein condensates, they are naturally suited as high precision sensors. Such a sensor is e.g. realized by trapping two Bose-Einstein condensates in a double well potential and investigating the evolution of the relative phase in the presence of external perturbations. However, if the two Bose-Einstein condensates are decoupled from each other, already small perturbations lead to the loss of the coherence between them, due to their extremely low energies, making their application difficult. By realizing a tunable coupling between the two Bose-Einstein condensates, the sensitivity to such external perturbations can be made adjustable over a wide range. This is the case, if the two Bose-Einstein condensate are not separated completely but there is a finite probability of particles tunneling from one to the other well. With this, a coherent coupling is implemented and results in an additional energy scale, which is easily tunable over a wide range. By adjusting this energy to be comparable to the external energy scales, e.g. to the thermal energy scale of the background gas, the phase difference between the two Bose-Einstein condensates will be

sensitive to the external perturbations. By monitoring the evolution of the relative phase or its fluctuations, the external perturbation can be investigated with high accuracy.

### Josephson junctions

Furthermore, the coherent coupling of two macroscopic matter waves gives rise to fundamentally new effects, which rely on the tunneling of massive particles between the two macroscopic matter waves. This fact has been conceived by the Nobel laureate Brian D. Josephson in 1962 [13], when he predicted the counterintuitive effect that a direct current can flow between two superconductors, which are connected via a very thin insulating layer, although no external voltage is present (DC Josephson effect). Furthermore, if an external voltage is applied to these 'Josephson junctions', an alternating current with a frequency depending only on the external voltage can be observed across the junction (AC Josephson effect).

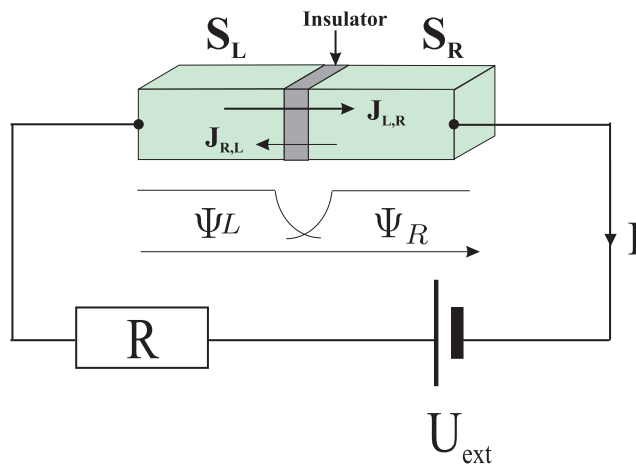


Figure 1.1: A sketch of the superconducting Josephson junction. The superconducting tunnel junction is provided by a thin insulating layer with a typical thickness of 1nm between the two superconductors  $S_L$  and  $S_R$ .  $J_{L,R}$  and  $J_{R,L}$  denote the tunneling current densities in both directions. The weakly overlapping macroscopic wavefunctions are indicated by  $\Psi_L$  and  $\Psi_R$ . Tunneling Cooper pairs are replaced by the external current source  $U_{\text{ext}}$ , which therefore suppresses charge-imbalances across the junction.

Fig. 1.1 shows a ketch of a superconducting Josephson junction. The two superconductors  $S_L$  and  $S_R$  are separated via a thin insulating barrier, through which the superconducting particles (Cooper pairs) can tunnel in both directions. The current densities are indicated by  $J_{L,R}$  and  $J_{R,L}$ . The external voltage  $U_{\text{ext}}$  replaces the missing charges and thus suppresses any charge-imbalances across the junction.

The physical situation of the Josephson junction can be described by two macroscopic wave functions ( $\Psi_L$  and  $\Psi_R$  displayed in Fig. 1.1), which correspond to the density of the Cooper pairs in the superconductors, and a potential barrier in between, which results from the insulating layer. If the height of the barrier is comparable to the chemical potential of the Cooper pairs, the amplitude of the wave functions within the barrier will drop rapidly to zero. However, if the barrier is not too high, the wave functions still have a small spatial overlap leading to a tunneling coupling of the two superconductors, i.e. a weak link.

The DC Josephson effect corresponds in this description to two coupled wave functions at the same chemical potentials. A quantum mechanical phase difference between the two leads to a direct current of particles through the barrier, where the direction and the magnitude

---

of the current depend on the phase difference.

The AC Josephson effect describes two wave functions at different chemical potentials. The quantum mechanical phases of both evolve according to their local energies at different rates and thus the phase difference between them winds up. According to the DC Josephson effect, a phase difference is directly connected to a tunneling of particles and with this the winding up of the phase leads to an oscillating current. The frequency of the current depends only on the rate of the phase evolution and is thus connected to the energy difference between the two chemical potential.

Very soon after the first experimental proof of principle [14], the Josephson effects found their way to various applications such as voltage standards (Shapiro effect) and ultrasensitive magnetic field sensors (SQUIDS). Also fundamental questions on quantum physics were and are extensively studied theoretically as well as experimentally with Josephson junctions in different configurations [15, 16], ranging from ultra small junctions to long junction arrays.

Since the Josephson junction dynamics 'only' relies on the existence of two weakly coupled macroscopic quantum states, a similar behavior has been observed in experiments with two superfluid Helium baths coupled through nano-apertures. The first superfluid Josephson junctions were generated with superfluid  $^3\text{He}$  in 1997 [17, 18, 19] and with  $^4\text{He}$  2001 [20].

With the advent of Bose-Einstein condensates of weakly interacting gases a new experimental system has become available for the quantitative investigation of the Josephson effects in a very well controllable environment. This was proposed already in 1986 [21], but only the recent development of an ultrastable double well potential for neutral atoms, as will be discussed within the scope of this thesis, made the experimental investigation of the Josephson effect possible.

Furthermore, also other questions from solid states physics could and can be tackled by confining Bose-Einstein condensates in periodic potentials. A very good control over the experimental parameters such as potential depths, lattice spacings, but also the strength of the interparticle interactions make the detailed investigations of many effects possible [22].

### **Predicted effects in bosonic Josephson junctions**

The geometry of a double well potential leads to an energy spectrum, in which the energy difference between the first two single particle mean field states is much smaller than the difference to all energetically higher lying states. Thus, the system can be reduced to two mean field orbitals in which the particles are located, if only low energetic excitations or low temperatures are of interest. With this, the Hilbert space of the many body problem is reduced to a dimension equal to the number of particles plus one (e.g. [23, 24]), making exact numeric calculations possible. Furthermore, the description of the bosonic Josephson junction can be reduced to a mean field two mode model, if the coupling between the two matter wave packets is adjusted such that the quantum mechanical uncertainties become negligible. Here the particles can occupy one of two localized matter wave packets, either in the left or the right well, and the state of the bosonic Josephson junction is determined by the population and the phase of these two modes (e.g. [25, 26, 27, 28]).

Starting with the theoretical discussion of the bosonic Josephson junction in 1986 [21], a tremendous amount of theoretical work was focused on different aspects of this simple quantum system. Topics like steady state properties at zero temperature [29, 30, 31] and at finite temperature [32], but also dynamical properties like low energetic excitations (Josephson plasmons [33]) or collapse and revival phenomena [34, 35, 36] have been studied extensively.

## Bosonic Josephson junction arrays

The first experimental tests of Josephson dynamics with Bose-Einstein condensates were performed in Josephson junction arrays, as in contrast to the single junction a lower degree of stability of the experimental system is required. Josephson junction arrays can be implemented by confining a Bose-Einstein condensate in a periodic potential. If the potential is deep enough, the atoms are localized within the wells and can move from well to well only via quantum mechanical tunneling. The theoretical description of two neighboring sites in a 1-D array is similar to that of a single Josephson junction but here also the coupling to the next sites has to be taken into account. Due to the coupling of all sites not only local effects but also global coherent phenomena appear.

The linear Josephson tunneling dynamics with Bose-Einstein condensates was observed in a Josephson junction array superimposed onto a shallow harmonic trapping potential in 2001 in the group of M. Inguscio [37]. Due to a shift of the harmonic potential a small external force was acting onto the atoms leading to a collective tunneling motion through the lattice. The local dynamics can be understood in terms of the AC Josephson effect, leading to a global oscillating current of atoms through the junction array. In these experiments, it was possible to measure the critical tunneling current of atoms as a function of the barrier height.

The observation of nonlinear dynamics in a Josephson junction array was discussed in 2005 [38]. In these experiments the non-linear expansion of a Bose-Einstein condensate in a periodic potential was investigated. The experiments showed that macroscopic quantum self trapping develops if the interaction energy of the atoms is above a critical value. This effect is in close analogy to self trapping in a double well system, where the relative phase of two adjacent sites evolves rapidly due to a large population imbalance and leads to the loss of the time averaged flux of atoms through the barrier.

## A single bosonic Josephson junction

The most direct way to generate a bosonic Josephson junction is the realization of a double well potential for a Bose-Einstein condensate. If the barrier is high enough, i.e. comparable to the chemical potential of the atoms, the Bose-Einstein condensate is split into two localized matter wave packets, and if the barrier is not too high, particles can tunnel from well to well leading to a coherent coupling. However, this realization demands a very high degree of stability of the potential shape, as the tunneling current depends exponentially on the barrier height.

The main goal of the work, which is presented in this thesis, was the experimental implementation of such a double well potential for Bose-Einstein condensates and the observation of the dynamical response as well as the steady state properties at finite temperature. So far, this work showed the only proof, that a Josephson junction can be realized with Bose-Einstein condensates. Furthermore, the comparison with different theoretical approaches revealed, that the behavior of the system can be understood quantitatively in terms of a mean field model in the relevant parameter range.

Our investigations showed also, that the dynamical response of the bosonic Josephson junction can be divided into two regimes, the plasma oscillation regime, where atoms tunnel back and forth between the wells, and the self trapping regime, where the tunneling is suppressed. The two dynamical regimes are accessible by initiating the dynamics with a population imbalance below a critical value (plasma oscillations) and with a population imbalance above (self trapping).

---

Furthermore, the investigation of the steady state properties at finite temperature revealed, that the dynamical variables are not locked to zero, as is expected from the ground state of the system, but show fluctuations. The amount of fluctuations are directly related to the thermal energy scale and the coupling constants. In the relevant parameter range, the distribution of the dynamical variables can be estimated using the Boltzmann distribution leading to a scaling behavior of the amount of fluctuations with a single parameter. For the relative phase this parameter is the ratio of the tunneling coupling and the thermal energy scale. Hence, by measuring the fluctuations and calculating the tunneling coupling, the temperature of the atoms can be predicted accurately. The applicability of the phase fluctuation thermometer was demonstrated by observing the heating up of a degenerate Bose gas in a 3-D harmonic trapping potential.

### **Other types of bosonic Josephson junctions**

Another promising method for generating a double well potential for neutral atoms was presented in the group of J. Schmiedmayer in 2005. Their approach is the application of radio-frequency dressed state potentials on an atom chip [39], which couples two atomic hyperfine levels to each other, in analogy to optical dipole traps, where two electronic states are addressed. Recently, these potentials were employed for coherent splitting of a Bose-Einstein condensate and for matter wave interference experiments [40].

A further possibility to realize a weak link between two spatially separated Bose-Einstein condensates was demonstrated in 2005 in the group of W. Ketterle [41]. They generated a double well potential, in which the direct spatial tunneling between the two Bose-Einstein condensates was excluded. By turning on a moving periodic potential (two Bragg beams) atoms were coherently coupled out from both Bose-Einstein condensates at a specific momentum. The momentum was chosen, such that the out-coupled atoms from the first Bose-Einstein condensates could reach the second. Here, according to the phase difference of the two coherent sources, the atoms either continued moving or were coupled into the second Bose-Einstein condensate. Due to this coherent exchange of particles a relative phase developed between the two Bose-Einstein condensates, and they became weakly coupled to each other.

In the literature, not only the external Josephson effect but also internal Josephson effects are discussed. Here, a two-component Bose-Einstein condensate is considered, where the two species (e.g. hyperfine levels) are coupled to each other (e.g. Raman coupling). The system exhibits similar dynamics as in the case of the external Josephson effect [42, 43]. Furthermore, the internal Josephson effect is not only predicted for purely bosonic systems, but also for the case of a four component degenerate Fermi system, where the four components are coupled to two types of BCS-pairs (in analogy to Cooper pairs for electrons). Josephson oscillations can be realized, if the two resulting superfluids are coupled via laser field [44]. Even in the case of a two component Fermi system in the vicinity of a narrow Feshbach resonance, Josephson dynamics is anticipated due to the tunneling of molecular Bosons into BCS-pairs and vice versa [45].

### **Publications on the bosonic Josephson junction**

The main results of our work were published in:

- Dynamics of the bosonic Josephson junction: [46] Direct observation of tunneling and nonlinear self-trapping in a single bosonic Josephson junction, M. Albiez, R.

Gati, J. Fölling, S. Hunsmann, M. Cristiani and M.K. Oberthaler. *Phys. Rev. Lett.* **95**(1):010402 (2005).

- Overview over the experimental setup and the experimental procedure: [47] Realization of a single Josephson junction for Bose-Einstein condensates, R. Gati, M. Albiez, J. Fölling, B. Hemmerling, and M.K. Oberthaler. *App. Phys. B* **82**:207 (2006)
- Finite temperature effects in steady state in the bosonic Josephson junction: [48] Noise Thermometry with Two Weakly Coupled Bose-Einstein Condensates, R. Gati, B. Hemmerling, J. Fölling, M. Albiez, and M. K. Oberthaler. *Phys. Rev. Lett.* **96**(13):130404 (2006)
- Application of the bosonic Josephson junction for thermometry: [49] A primary noise thermometer for ultracold bose gases, R. Gati, J. Esteve, B. Hemmerling, T.B. Ottenstein, J. Appmeier, A. Weller, and M. K. Oberthaler *N. J. Phys.*, **8**:189, 2006.

## Outline

The first part of the presented work (Chapter 2) is devoted to the discussion of the basic theory of the bosonic Josephson junction. A summary of the theoretical background of Bose-Einstein condensates is followed by the discussion of the Bose-Hubbard model, where the Hilbert space of the many body system is reduced to a size which can be handled numerically. To be able to interpret the experimentally accessible observables in the many body picture, it is necessary to introduce a phase operator, which is discussed in the next section. Afterwards, the mean field description is discussed, which allows for an intuitive insight into the properties of the Josephson junction in form of a mechanical analogue. The main properties of the bosonic Josephson junction can be directly extracted from this simple picture.

The second part (Chapter 3) consists of the description of the experimental apparatus followed by a discussion on the relevant parameters and how those are calibrated for the experiments. A brief presentation of the properties of the double well potential and the experimental access to the quantum mechanical observables closes this chapter.

The third part (Chapter 4) deals with the steady state properties of the bosonic Josephson junction. Here, the behavior of the dynamical variables is investigated in the zero temperature regime, where the steady state population of different asymmetric double well potentials is measured, and in the finite temperature regime, where thermally induced fluctuations of the relative phase are observed. Furthermore, the comparison of the thermally induced fluctuations to the theoretical prediction reveals, that the measurement of the phase fluctuations is applicable for thermometry. In order to prove the principle, the temperature of a degenerate Bose gas is observed during heating up.

The last part (Chapter 5) describes the dynamical properties of the bosonic Josephson junction at zero temperature. Two major dynamical regimes can be distinguished, the plasma oscillation regime, where the population imbalance and the relative phase oscillate around a zero mean value and the self trapping regime, where the population imbalance is locked and the relative phase winds up. Experimentally, the dynamics is triggered by preparing an initial population imbalance in an asymmetric double well and quickly removing the asymmetry. With different initial population imbalances both dynamical regimes become accessible.

---

## 2 Basic theory of the Bosonic Josephson Junction

A Josephson junction consists of a weak link between two macroscopic matter wave functions. A possible experimental implementation of the bosonic version of such a Josephson junction (BJJ) is the realization of a double well potential for a Bose-Einstein condensate (BEC), where the single macroscopic wave function of the condensed atoms is split into two spatially localized matter wave packets, which are connected to each other via tunneling of particles through the barrier. For the physical understanding of the BJJ the underlying theory will be discussed in this chapter, starting with the theoretical background of the degenerate quantum gases, followed by the theory of the two mode model, which is a formal description of the weak link. In the last part of the chapter I point out, that the complex quantum field theoretical description can be reduced to a very simple form, where it becomes analogous to a mechanical system leading to a straightforward and intuitive understanding of the behavior of the BJJ.

### 2.1 The Bose-Einstein condensate

A system consisting of  $N$  indistinguishable Bosons (i.e. particles with integer spin) confined in a box-shaped or a harmonic trapping potential can be described by a quantum mechanical wave function which is symmetric under the exchange of any two particles. Bosons follow the Bose-Einstein statistics [7, 8] and their distribution at finite temperature is given by the Bose-Einstein distribution [50]

$$N_i(T) = f(E_i, T) = \left( \exp \left( \frac{E_i - \mu}{k_B T} \right) - 1 \right)^{-1}, \quad (2.1)$$

where  $k_B$  is the Boltzmann constant,  $N_i$  is the population and  $E_i$  the energy of the  $i$ -th eigenstate,  $T$  is the temperature and  $\mu$  is the chemical potential defined by the normalization condition for the total number of particles  $N = \sum_i N_i(\mu)$ . For large particle numbers and low temperature, the chemical potential becomes comparable to the ground state energy and the normalization condition can be written as

$$N = N_0 + N_{\text{th}} = N_0 + \sum_{i>0} N_i(T) = N_0 + \sum_{i>0} \left( \exp \left( \frac{E_i - E_0}{k_B T} \right) - 1 \right)^{-1}, \quad (2.2)$$

where  $E_0$  is the energy of the ground state. According to Eq. 2.2 in a 3-D system at any finite temperature only a finite number of particles can be stored in energy levels above the ground state. By increasing the number of Bosons or by decreasing the temperature, this restriction can only be met if the additional particles are located in the ground state. Thus, depending on the external potential and the experimental parameters, a critical temperature  $T_c$  can be

defined, below which the population of the ground state becomes macroscopic  $N_0 \gg N_{i>0}$ . This macroscopic population of the ground state is called Bose-Einstein condensation and the particle ensemble populating the ground state is called a Bose-Einstein condensate.

### 2.1.1 The weakly interacting Bose gas

Neutral bosonic atoms used for BEC experiments interact with each other. In general, the only relevant interatomic interaction<sup>1</sup> is the van-der-Waals interaction, which should for an accurate description of the atomic Bose-Einstein condensates be also taken into account [52].

The Hamiltonian of weakly interacting particles in an external potential can be written as [53, 54]

$$\hat{H} = \int \left( -\frac{\hbar^2}{2m} \hat{\Psi}^\dagger(\mathbf{r}) \nabla^2 \hat{\Psi}(\mathbf{r}) \right) d\mathbf{r} + \int \left( \hat{\Psi}^\dagger(\mathbf{r}) V_{\text{ext}}(\mathbf{r}) \hat{\Psi}(\mathbf{r}) \right) d\mathbf{r} + \frac{1}{2} \int \left( \hat{\Psi}^\dagger(\mathbf{r}) \hat{\Psi}^\dagger(\mathbf{r}') V_{\text{int}}(\mathbf{r}' - \mathbf{r}) \hat{\Psi}(\mathbf{r}) \hat{\Psi}(\mathbf{r}') \right) d\mathbf{r}' d\mathbf{r}, \quad (2.3)$$

where  $\hat{\Psi}^\dagger(\mathbf{r})$  ( $\hat{\Psi}(\mathbf{r})$ ) is the field operator creating (annihilating) a particle at the point  $\mathbf{r}$ . Furthermore,  $m$  is the mass of the particles,  $V_{\text{ext}}$  is the external potential and  $V_{\text{int}}$  is the atom-atom interaction potential. For sufficiently low temperatures and low densities the only relevant interactions are low energetic two body collisions. In this limit the collisions are described in terms of s-wave scattering. Here, the atom-atom interaction potential is approximated by its ( $q = 0$ )-Fourier component  $V_{\text{int}}(\mathbf{r}' - \mathbf{r}) \approx g\delta(\mathbf{r}' - \mathbf{r})$  with  $g = \frac{4\pi\hbar^2 a}{m}$ , where  $a$  is the s-wave scattering length. This approximation is valid if the effective range of interaction is much smaller than the typical distance between the atoms. Inserting the approximated interaction potential into Eq. 2.3 the Hamiltonian becomes

$$\hat{H} = \int \left( -\frac{\hbar^2}{2m} \hat{\Psi}^\dagger(\mathbf{r}) \nabla^2 \hat{\Psi}(\mathbf{r}) \right) d\mathbf{r} + \int \left( \hat{\Psi}^\dagger(\mathbf{r}) V_{\text{ext}}(\mathbf{r}) \hat{\Psi}(\mathbf{r}) \right) d\mathbf{r} + \frac{g}{2} \int \left( \hat{\Psi}^\dagger(\mathbf{r}) \hat{\Psi}^\dagger(\mathbf{r}) \hat{\Psi}(\mathbf{r}) \hat{\Psi}(\mathbf{r}) \right) d\mathbf{r}. \quad (2.4)$$

For large atom numbers, if quantum mechanical fluctuations are negligible ( $\langle N_0^2 \rangle - \langle N_0 \rangle^2 \ll \langle N_0 \rangle^2$ ), the Bogoliubov approximation can be applied. Here the operator  $\hat{\Psi}(\mathbf{r})$  is replaced by a complex field  $\Psi_0(\mathbf{r})$  and a fluctuation operator  $\hat{\Psi}'(\mathbf{r})$  leading to  $\hat{\Psi}(\mathbf{r}) = \Psi_0(\mathbf{r}) + \hat{\Psi}'(\mathbf{r})$ . For the conditions given above the expectation value of  $\hat{\Psi}'(\mathbf{r})$  is small and can be neglected. By applying the Heisenberg equation to the wave function, we find the Gross-Pitaevskii equation (GPE)

$$i\hbar \frac{\partial}{\partial t} \Psi(\mathbf{r}) = \left( -\frac{\hbar^2}{2m} \nabla^2 + V_{\text{ext}}(\mathbf{r}) + gN_0 |\Psi(\mathbf{r})|^2 \right) \Psi(\mathbf{r}) \quad \text{with} \quad \int |\Psi(\mathbf{r})|^2 d\mathbf{r} = 1. \quad (2.5)$$

The GPE is a nonlinear Schrödinger equation describing the temporal evolution of the wave function of the BEC at  $T = 0$ . The nonlinearity in this equation results from the interaction of the particle with the other particles in the BEC, which can effectively be described by a mean field potential. As in this picture all particles occupy the same quantum state, the density distribution of the Bose-Einstein condensate is given by  $n(\mathbf{r}) = N_0 |\Psi(\mathbf{r})|^2$ .

<sup>1</sup>In certain cases, the (magnetic or electric) dipole-dipole interaction has also to be taken into account, as in the case of Chromium Bose-Einstein condensates, in which the magnetic dipole-dipole interaction plays in certain situations an important role [51].

Care has to be taken as the GPE describes a single particle in the vicinity of all other particles and thus, the energy associated to the GPE is the chemical potential  $\mu$  and not the energy per particle  $E_0$ . The chemical potential is the derivative of the total energy with respect to the number of particles  $\mu = \partial(N_0 \cdot E_0)/\partial N_0$ . Thus, the two quantities  $\mu$  and  $E_0$  are only equal if the interatomic interaction is negligible, otherwise they are given by

$$\mu = \int \Psi^*(\mathbf{r}) \left( -\frac{\hbar^2}{2m} \nabla^2 + V_{\text{ext}}(\mathbf{r}) + gN_0 |\Psi(\mathbf{r})|^2 \right) \Psi(\mathbf{r}) d\mathbf{r}, \quad (2.6)$$

$$E_0 = \int \Psi^*(\mathbf{r}) \left( -\frac{\hbar^2}{2m} \nabla^2 + V_{\text{ext}}(\mathbf{r}) + \frac{gN_0}{2} |\Psi(\mathbf{r})|^2 \right) \Psi(\mathbf{r}) d\mathbf{r}. \quad (2.7)$$

The discrepancy of the two equations can be understood by considering that the interaction energy in the chemical potential results from the interaction of a particle with all other particles, leading to the energy  $g(N_0 - 1) \approx gN_0$  for large atom numbers. However, for the total interaction energy, the number of possible pairs has to be taken into account, which is  $gN_0(N_0 - 1)/2 \approx gN_0^2/2$ . Dividing by the number of particles leads to the expression for the energy per particle given above.

The particles can interact with each other either attractively ( $a < 0$ ) or repulsively ( $a > 0$ ), but as the atomic species used in the experiments ( $^{87}\text{Rb}$ ) interacts repulsively, I will in the following concentrate on the discussion of the case ( $a > 0$ ) only.

### 2.1.2 Properties of Bose-Einstein condensates in a harmonic trapping potential

For low energies and low temperatures, the external potential usually realized in experimental setups is approximately described by a 3-D harmonic trapping potential  $V_{\text{ext}} = \frac{1}{2}m \sum_{i=x,y,z} \omega_i^2 r_i^2$ . In the case of non-interacting Bosons the ground state density distribution in the 3-D trap corresponds to a 3-D Gaussian distribution

$$\Psi(\mathbf{r}) = \frac{1}{\pi^{3/4} (\sigma_x \sigma_y \sigma_z)^{1/2}} \cdot e^{-\frac{x^2}{2\sigma_x^2} - \frac{y^2}{2\sigma_y^2} - \frac{z^2}{2\sigma_z^2}}, \quad (2.8)$$

where  $\sigma_i = \sqrt{\frac{\hbar}{m\omega_i}}$ . The ground state energy per particle is

$$E_0^{\text{lin}} = \frac{\hbar}{2} \sum \omega_i, \quad (2.9)$$

and the excitation energy spectrum is governed by

$$E^{\text{lin}} = E_0^{\text{lin}} + \hbar \sum n_i \omega_i \quad \text{with} \quad n_i \in \mathbb{N}, \quad (2.10)$$

which corresponds to a density of states of

$$g(E) = \frac{E^2}{2(\hbar\bar{\omega})^3} \quad \text{with} \quad \bar{\omega} = (\omega_x \omega_y \omega_z)^{1/3}. \quad (2.11)$$

For weakly interacting Bosons, if the interaction energy is low enough and can be neglected, the general properties of the BEC can be understood by considering non-interacting particles. The relevant thermodynamical quantities are calculated from the density of states (Eq. 2.11) and the Bose-Einstein distribution (Eq. 2.1) [54].

The number of particles in the excited states of the 3-D harmonic trap at a temperature below the critical temperature is given by

$$N_{\text{th}} = \int_0^\infty dE \cdot g(E)f(E) = \frac{1}{(\hbar\bar{\omega})^3} \zeta(3)(k_B T)^3 = N \left( \frac{T}{T_c} \right)^3, \quad (2.12)$$

with  $\zeta(x) = \sum_{n=1}^\infty n^{-x}$  being the Riemann zeta function. The condensate fraction is

$$N_0 = N - N_{\text{th}} = N \left( 1 - \left( \frac{T}{T_c} \right)^3 \right). \quad (2.13)$$

Here, the critical temperature is defined by the condition  $N_{\text{th}}(T_c) = N$  and is given by

$$k_B \cdot T_c = \hbar\bar{\omega} \left( \frac{N}{\zeta(3)} \right)^{1/3} \approx 0.94 \hbar\bar{\omega} N^{1/3}. \quad (2.14)$$

The energy stored in the degenerate Bose gas, its heat capacity and its entropy can be calculated using similar arguments

$$E = \int_0^\infty dE \cdot E \cdot g(E)f(E) = \frac{3}{(\hbar\bar{\omega})^3} \zeta(4)(k_B T)^4 = N 3 k_B \frac{\zeta(4)}{\zeta(3)} \frac{T^4}{T_c^3}, \quad (2.15)$$

$$C = \frac{\partial E}{\partial T} = 4 \frac{E}{T} = N 12 k_B \frac{\zeta(4)}{\zeta(3)} \left( \frac{T}{T_c} \right)^3, \quad (2.16)$$

$$S = C/3 = N 4 k_B \frac{\zeta(4)}{\zeta(3)} \left( \frac{T}{T_c} \right)^3 \quad \text{from} \quad C = T \frac{\partial S}{\partial T}. \quad (2.17)$$

In the high temperature limit, the heat capacity approaches the classically expected value of  $C(T \gg T_c) = 3Nk_B$ . At the critical temperature, the heat capacity is not continuous but has a jump, which is related to the fact, that the chemical potential below the critical temperature is zero but it is finite above. A short discussion on the heat capacity close to the transition temperature and above can be found in Appendix A.

### Strongly anisotropic harmonic trapping potential

In a strongly anisotropic trap, the behavior of a Bose gas at low temperature is fundamentally different from the isotropic case [55]. In a 1-D ( $\omega_x \ll \omega_y \approx \omega_z$ ) or a 2-D trap ( $\omega_x \gg \omega_y \approx \omega_z$ ) low energetic excitations exist, such that  $\min(\hbar\omega_i) \ll k_B T \ll k_B T_c$  where  $T_c$  is defined by Eq. 2.14. This leads to the macroscopic population of low lying excited states even at temperatures far below  $T_c$  [56, 57] and hence, to a reduction of the coherence. For low densities, the system can even change its character from 3-D to quasi 1-D or 2-D by freezing out excitations into the direction of the strong confinement. In the 1-D case no Bose-Einstein condensation can be reached, only the coherence length of the system can be increased to become larger than the size of the cloud. In 2-D, not only Bose-Einstein condensation [58] but also the so-called Berezinskii-Kosterlitz-Thouless crossover [57] exists and in the intermediate regime of the cross-over, the behavior of the ground state wave function is dominated by thermal processes.

### Thomas-Fermi approximation

The GPE (Eq. 2.5) can be solved analytically either in the linear limit  $g \rightarrow 0$  or in the Thomas-Fermi limit (TFL), where the total energy is dominated by the interaction energy. In the TFL, the density distribution is broadened with respect to the non-interacting case in order to reduced the density and with it the interaction energy. However, the broadening of the density distribution leads to an increase of the stored potential energy. Furthermore, the broadening of the real space distribution also results in a narrowing of the momentum distribution and a reduction of the kinetic energy. Thus, the wave function is described by the balance of the potential energy and the interaction energy and the kinetic energy becomes unimportant. The negligence of the kinetic term is called the Thomas-Fermi approximation

$$\mu\Psi(\mathbf{r}) = (V_{\text{ext}}(\mathbf{r}) + g \cdot N_0|\Psi(\mathbf{r})|^2) \Psi(\mathbf{r}), \quad (2.18)$$

leading to

$$n(\mathbf{r}) = N_0|\Psi(\mathbf{r})|^2 = \begin{cases} \frac{\mu - V_{\text{ext}}(\mathbf{r})}{gN_0} & \text{if } \mu - V_{\text{ext}}(\mathbf{r}) \geq 0 \\ 0 & \text{if } \mu - V_{\text{ext}}(\mathbf{r}) < 0, \end{cases} \quad (2.19)$$

where  $\mu$  is defined by the normalization condition  $\int |\Psi(\mathbf{r})|^2 d\mathbf{r} = 1$ .

In a 3-D harmonic trap the density distribution is parabolic and the chemical potential and the energy per particle are given by

$$\mu = \frac{\hbar\bar{\omega}}{2} \left( \frac{15N_0a}{\bar{\sigma}} \right)^{2/5}, \quad (2.20)$$

$$E_0 = \frac{E}{N_0} = \frac{5}{7}\mu, \quad (2.21)$$

with  $\bar{\sigma} = \sqrt{\hbar/m\bar{\omega}}$ . The size of the cloud is then defined by the Thomas-Fermi radii (TFR)

$$R_i^2 = \frac{2\mu}{m\omega_i^2}. \quad (2.22)$$

The Thomas-Fermi approximation is intrinsically not valid close to the TFR, as here the density is low and thus the kinetic energy is not negligible, leading to a smoothing of the wave function at the edge.

### 2.1.3 Momentum distribution of a degenerate Bose gas

Information about the degenerate Bose gas can be obtained by projecting its wave function either into real space corresponding to the density distribution or into momentum space corresponding to the momentum distribution. The density can be measured by e.g. using absorption imaging techniques, where the particles are illuminated with resonant light and the resulting loss of photons from the coherent beam is resolved spatially (see Sec. 3.1.6). The momentum distribution can also be measured by using the same absorption imaging technique. Here, the density distribution is not measured directly in the trapping potential but after ballistic expansion. For this, the external confining potential is turned off and the particles are released from the trap. During the free evolution the distribution expands due to the stored kinetic and interaction energy. The far field is reached, as soon as the size of the resulting density distribution is much larger than the initial size of the cloud.

### Free expansion of a non-interacting BEC at zero temperature

In the linear case, the wave function of a single particle in the ground state of the 3-D harmonic trap is given by Eq. 2.8. The corresponding wave function in momentum space is obtained by Fourier transformation and is given by

$$\tilde{\Psi}(\mathbf{p}) = \frac{1}{\pi^{3/4}(\sigma_{px}\sigma_{py}\sigma_{pz})^{1/2}} \cdot e^{-\frac{p_x^2}{2\sigma_{px}^2} - \frac{p_y^2}{2\sigma_{py}^2} - \frac{p_z^2}{2\sigma_{pz}^2}}, \quad (2.23)$$

where  $\sigma_{pi} = \sqrt{m\hbar\omega}$ . In time of flight experiments, the density distribution broadens according to the momentum distribution after releasing the matter wave packet from the trap. The temporal evolution is governed by

$$\Psi(\mathbf{r}, t) = \frac{1}{\pi^{3/4}(\sigma_x(t)\sigma_y(t)\sigma_z(t))^{1/2}} \cdot e^{-\frac{x^2}{2\sigma_x(t)^2} - \frac{y^2}{2\sigma_y(t)^2} - \frac{z^2}{2\sigma_z(t)^2}}, \quad (2.24)$$

with  $\sigma_i(t)^2 = \sigma_i^2 + (\sigma_{pi}t/m)^2 = \hbar/m\omega_i + \hbar\omega_i t^2/m$ . This relation shows that the expansion velocity in the direction of high confinement is large and thus a wave packet released from an anisotropic trap will invert its aspect ratio during its ballistic expansion.

### Free expansion in the Thomas-Fermi limit

The free expansion of a matter wave packet in the Thomas-Fermi limit is discussed in [59, 60, 61]. The temporal evolution of the TFR (Eq. 2.22) is described by differential equations, where scaling parameters  $\lambda_i$  are introduced to account for the expansion

$$\begin{aligned} R_i(t) &= \lambda_i R_i(0) \\ \text{with } \frac{\partial^2 \lambda_i}{\partial t^2} &= \frac{\omega_i(0)^2}{\lambda_i \lambda_x \lambda_y \lambda_z}. \end{aligned} \quad (2.25)$$

If the three trapping frequencies are equal, the differential equations lead to a constant expansion velocity with  $R(t) \approx 0.8\omega R(0)t$  in the far field. For cylindrical symmetry and large aspect ratios the temporal evolution is discussed in [59].

### Free expansion of a non-interacting BEC at finite temperature

The expansion of a degenerate Bose gas at finite temperature can be described in two different ways. In general, if the interaction is weak enough, in the far field the density distribution corresponds to the momentum distribution and results from the Bose-Einstein distribution of the particles in the trapping potential. However, a direct fitting of the profile with the appropriate momentum distribution is time-consuming.

In order to reduce the effort, the full distribution is split into two parts, the BEC fraction at zero temperature consisting of the particles in the ground state and the thermal cloud, resulting from the particles in the excited states. The thermal cloud is approximately given in terms of an ideal classical gas [62]. At finite temperature the distribution of a classical gas in the 3-D harmonic trap is given by the Boltzmann distribution

$$f_{\text{cl}}(\mathbf{r}, \mathbf{p}) = \frac{N\omega_x\omega_y\omega_z}{(2\pi k_B T)^3} \exp\left(-m\frac{\omega_x^2 x^2 + \omega_y^2 y^2 + \omega_z^2 z^2}{2k_B T} - \frac{p_x^2 + p_y^2 + p_z^2}{2mk_B T}\right), \quad (2.26)$$

leading to the density distribution

$$n_{\text{cl}}(\mathbf{r}) = \frac{N\omega_x\omega_y\omega_z m^{3/2}}{(2\pi k_B T)^{3/2}} \exp\left(-m \frac{\omega_x^2 x^2 + \omega_y^2 y^2 + \omega_z^2 z^2}{2k_B T}\right). \quad (2.27)$$

By turning off the trapping potential, the cloud is released and expands according to the Maxwell-Boltzmann velocity distribution. The resulting temporal evolution of the classical gas is then given by

$$n_{\text{cl},t}(\mathbf{r}) = \frac{N}{\pi^{3/2} (\sigma_x(t)\sigma_y(t)\sigma_z(t))} \cdot e^{-\frac{x^2}{2\sigma_x(t)^2} - \frac{y^2}{2\sigma_y(t)^2} - \frac{z^2}{2\sigma_z(t)^2}}, \quad (2.28)$$

with

$$\sigma_i(t)^2 = \frac{k_B T}{m\omega_i^2} + \frac{k_B T}{m} t^2 = \sigma_i(0)^2 + (\bar{v}t)^2, \quad (2.29)$$

where  $\bar{v}$  is the mean velocity of the particles. It is important to note, that for low temperatures in the case of a degenerate Bose gas, a correction has to be taken into account. The correction results from the fact, that the chemical potential of the degenerate Bose gas is higher (slightly below the ground state energy) than for a classical gas, which is below the minimum of the trapping potential. With this, there is an additional amount of energy converted into kinetic energy, which corresponds to the real chemical potential, and makes the expansion velocity of the classical gas always faster than the expansion velocity of a BEC at zero temperature.

#### 2.1.4 Temperature measurement of a degenerate Bose gas

The temperature of the bosonic particles is usually deduced from the density distribution after a free expansion. If the temperature of the gas is above the critical temperature for Bose-Einstein condensation, the velocity distribution of a thermal (classical) gas has a Gaussian profile and after a time of flight it can be fitted with the Maxwell-Boltzmann distribution given in Eq. 2.28. The temperature is obtained directly from the measured waist  $\sigma_m$  after a given time of flight  $t_{\text{tof}}$  and is given by

$$k_B T = \frac{\sigma_m^2 m}{1/\omega_i^2 + t_{\text{tof}}^2}. \quad (2.30)$$

Also the temperature of a degenerate Bose gas can be deduced from the distribution after ballistic expansion. As the expansion velocity of the ground state is always smaller than the velocity of the thermal components a bimodal distribution becomes visible in the expansion measurements. The distribution consists of a broad background corresponding to the thermal cloud and a peak in the center corresponding to the condensed particles. The distribution might be fitted with a bimodal distribution consisting of a Gaussian distribution (Eq. 2.28) for the thermal component and either a Gaussian profile (Eq. 2.24) or a Thomas-Fermi profile (Eq. 2.25) for the condensed particles. The temperature is then either derived from the average expansion velocity or from the ratio of the condensed fraction and the total number of atoms according to (from Eq. 2.13)

$$T = T_c \cdot \left(1 - \frac{N_0}{N}\right)^{1/3}. \quad (2.31)$$

This method for thermometry starts to fail when the number of particles in the thermal cloud becomes too small to be observed. Due to the cubic dependence of the thermal fraction

on the temperature already at  $T_c/2$ , only about 10% of the particles are located in the excited states. For lower temperatures, this number decreases rapidly making the application of the time of flight method for the measurement of very low temperatures extremely difficult.

However, thermometry far below the critical temperature is still possible by introducing a new method, where not the expansion of a single degenerate Bose gas is observed, but the fluctuations of the interference patterns of two initially coupled Bose-Einstein condensates. This method will be discussed in the Sec. 4.2.5 in more detail.

## 2.2 Two mode approximation - the Bose Hubbard model

Bose-Einstein condensates at low temperature can be used to realize a bosonic Josephson junction. For this, a weak link has to be prepared, which is present if the energy difference between the first two single particle eigenstates of the trapping potential is much smaller than the difference to all other energetically higher lying states. This situation can be reached by implementing a double well potential for Bose-Einstein condensates consisting of an overall confinement and a barrier in the center. If the barrier height is comparable to the chemical potential of the atoms, the first two single particle levels will be quasi degenerate and for low energetic excitations, only these two states will play a role.

The ground state of the double well potential is well defined and can be calculated by solving the Gross-Pitaevskii equation numerically if a mean field description is appropriate (see Appendix B). The mean field description is only valid for large atom numbers and in the Josephson regime (see Sec. 2.2.3), where the quantum mechanical uncertainty of the atom numbers is small and a relative phase between the matter wave packets in the two wells can be defined. If the mean field description fails, more detailed approaches e.g. [63, 64] might be able to describe the system accurately.

In the linear case, if the particles do not interact with each other, not only the ground state but also the first excited state is well defined and corresponds to the single particle excited state. However, if the interatomic interactions are relevant, the definition of the first excited single particle state is not obvious. Different possibilities are e.g. the wave function of a single excited particle, while all other particles are populating the ground state, the first Bogoliubov excited state [33], or the first excited single particle state, which is populated with all particles. These different possibilities arise from the fact, that the wave function of the first excited single particle state depends on the population of all states. Thus, if only very small energetic excitations are considered, corresponding to only a few existing excitations, the Bogoliubov description can be applied. However, if the energy scale is high enough to create a number of excitations comparable to the total number of particles, the first excited state should be calculated by populating this state with all particles. For our description we are going to consider the two wave functions  $\Phi_g$  (ground state) and  $\Phi_e$  (first single particle excited state), which are both solutions of the Gross-Pitaevskii equation (Eq. 2.5) with the chemical potential  $\mu_g$  and  $\mu_e$  respectively

$$\mu_{g,e}\Phi_{g,e} = -\frac{\hbar^2}{2m}\nabla^2\Phi_{g,e} + (V_{\text{dw}} + gN|\Phi_{g,e}|^2)\Phi_{g,e}, \quad (2.32)$$

where  $V_{\text{dw}}$  is the 3-D double well potential,  $g = \frac{4\pi\hbar^2 a}{m}$  is the coupling constant and  $a$  is the s-wave scattering length of the particles.

If the relevant energy scale is much lower than the energy needed to transfer a macroscopic population to higher lying single particle excited states, the full many body Hamiltonian can

be reduced to an effective Hamiltonian describing the particles only in these two states. Thus, the two mode approximation and the resulting two mode model can be applied for investigating the steady state properties of the BJJ and for low energetic excitations. Following the derivation presented in [24] or in [30] the relevant many particle energy functional is given by

$$\hat{H} = \hat{H}_0 + \hat{H}_{\text{int}}, \quad (2.33)$$

$$\hat{H}_0 = \int d\mathbf{r} \left( -\frac{\hbar^2}{2m} \hat{\Psi}^\dagger \nabla^2 \hat{\Psi} + \hat{\Psi}^\dagger V_{\text{dw}} \hat{\Psi} \right), \quad (2.34)$$

$$\hat{H}_{\text{int}} = \frac{g}{2} \int d\mathbf{r} \hat{\Psi}^\dagger \hat{\Psi}^\dagger \hat{\Psi} \hat{\Psi}. \quad (2.35)$$

We can rewrite the wave function  $\hat{\Psi}$  by applying the two mode approximation with

$$\hat{\Psi} = \hat{c}_g \Phi_g + \hat{c}_e \Phi_e \quad \text{with} \quad \int d\mathbf{r} |\Phi_{g,e}|^2 = 1, \quad (2.36)$$

and with  $\hat{c}_g^\dagger$  and  $\hat{c}_e^\dagger$  ( $\hat{c}_g$  and  $\hat{c}_e$ ) being the creation (annihilation) operators for a particle in the ground and the excited state. The operators obey the standard bosonic commutation relation  $[\hat{c}_i, \hat{c}_j^\dagger] = \delta_{ij}$ . A more direct and convenient choice for the basis are atom number states in the left and the right well (Fock states) with the corresponding creation operators  $\hat{c}_l = \frac{1}{\sqrt{2}}(\hat{c}_g + \hat{c}_e)$  and  $\hat{c}_r = \frac{1}{\sqrt{2}}(\hat{c}_g - \hat{c}_e)$ . In this basis,  $\hat{\Psi}$  is given by

$$\hat{\Psi} = \hat{c}_l \frac{\Phi_g + \Phi_e}{\sqrt{2}} + \hat{c}_r \frac{\Phi_g - \Phi_e}{\sqrt{2}}. \quad (2.37)$$

By inserting Eq. 2.37 into Eq. 2.34 we find

$$\begin{aligned} \hat{H}_0 &= (\hat{c}_l^\dagger \hat{c}_l + \hat{c}_r^\dagger \hat{c}_r) \frac{E_g + E_e}{2} + (\hat{c}_l^\dagger \hat{c}_r + \hat{c}_r^\dagger \hat{c}_l) \frac{E_g - E_e}{2} \\ &= N \frac{E_g + E_e}{2} + (\hat{c}_l^\dagger \hat{c}_r + \hat{c}_r^\dagger \hat{c}_l) \frac{E_g - E_e}{2}, \end{aligned} \quad (2.38)$$

with

$$E_{g,e} = \int d\mathbf{r} \left( -\frac{\hbar^2}{2m} \Phi_{g,e}(\mathbf{r}) \nabla^2 \Phi_{g,e}(\mathbf{r}) + \Phi_{g,e}(\mathbf{r}) V_{\text{dw}}(\mathbf{r}) \Phi_{g,e}(\mathbf{r}) \right), \quad (2.39)$$

and substituting into Eq. 2.35 we find

$$\begin{aligned} \hat{H}_{\text{int}} &= \hat{c}_l^\dagger \hat{c}_l^\dagger \hat{c}_l \hat{c}_l [s]^4 + \hat{c}_r^\dagger \hat{c}_r^\dagger \hat{c}_r \hat{c}_r [a]^4 + (\hat{c}_l^\dagger \hat{c}_l^\dagger \hat{c}_r \hat{c}_r + \hat{c}_l^\dagger \hat{c}_r^\dagger \hat{c}_l \hat{c}_r \\ &+ \hat{c}_l^\dagger \hat{c}_r^\dagger \hat{c}_r \hat{c}_l + \hat{c}_r^\dagger \hat{c}_l^\dagger \hat{c}_l \hat{c}_r + \hat{c}_r^\dagger \hat{c}_l^\dagger \hat{c}_r \hat{c}_l + \hat{c}_r^\dagger \hat{c}_r^\dagger \hat{c}_l \hat{c}_l) [s]^2 [a]^2 \\ &+ (\hat{c}_l^\dagger \hat{c}_l^\dagger \hat{c}_l \hat{c}_r + \hat{c}_l^\dagger \hat{c}_l^\dagger \hat{c}_r \hat{c}_l + \hat{c}_l^\dagger \hat{c}_r^\dagger \hat{c}_l \hat{c}_l + \hat{c}_r^\dagger \hat{c}_l^\dagger \hat{c}_l \hat{c}_l) [s]^3 [a] \\ &+ (\hat{c}_l^\dagger \hat{c}_r^\dagger \hat{c}_r \hat{c}_r + \hat{c}_r^\dagger \hat{c}_l^\dagger \hat{c}_r \hat{c}_r + \hat{c}_r^\dagger \hat{c}_r^\dagger \hat{c}_l \hat{c}_r + \hat{c}_r^\dagger \hat{c}_r^\dagger \hat{c}_r \hat{c}_l) [s] [a]^3, \end{aligned} \quad (2.40)$$

with

$$[s]^i [a]^j = \frac{1}{4} \int d\mathbf{r} (\Phi_g(\mathbf{r}) + \Phi_e(\mathbf{r}))^i \cdot (\Phi_g(\mathbf{r}) - \Phi_e(\mathbf{r}))^j. \quad (2.41)$$

After some algebra and using the commutation relations (e.g.  $\hat{c}_r^\dagger \hat{c}_l^\dagger \hat{c}_l \hat{c}_l = \hat{c}_r^\dagger \hat{c}_l \cdot \hat{c}_l^\dagger \hat{c}_l - \hat{c}_r^\dagger \hat{c}_l$ ) the two mode Hamiltonian can be rewritten to the form

$$\hat{H}_{2M} = \frac{E_c}{8} (\hat{c}_r^\dagger \hat{c}_r - \hat{c}_l^\dagger \hat{c}_l)^2 - \frac{E_j}{N} (\hat{c}_l^\dagger \hat{c}_r + \hat{c}_r^\dagger \hat{c}_l) + \frac{\delta E}{4} (\hat{c}_l^\dagger \hat{c}_r + \hat{c}_r^\dagger \hat{c}_l)^2, \quad (2.42)$$

with the parameters

$$E_c = 8\kappa_{g,e}, \quad (2.43)$$

$$E_j = \frac{N}{2}(\mu_e - \mu_g) - \frac{N(N+1)}{2}(\kappa_{e,e} - \kappa_{g,g}), \quad (2.44)$$

$$\delta E = \frac{\kappa_{g,g} + \kappa_{e,e} - 2\kappa_{g,e}}{4} \quad (2.45)$$

$$\text{where } \kappa_{i,j} = \frac{g}{2} \int d\mathbf{r} |\Phi_i|^2 |\Phi_j|^2, \quad (\text{with } i, j = g, e). \quad (2.46)$$

The term proportional to the tunneling coupling ( $E_j$ ) describes the tunneling of particles from one well to the other, the term proportional to the charging energy (or onsite-interaction energy  $E_c$ ) corresponds to the local interaction within the two wells, and the term proportional to  $\delta E$  takes additional two particle processes like two particle tunneling into account. In our experimental parameter range, this term is less than  $10^{-5} \cdot E_j/N$  and less than  $10^{-3} \cdot E_c/8$ . Its effect on the experimentally observable quantities is too small and will thus be neglected for the following discussions. In this limit, the two mode Hamiltonian Eq. 2.42 is given by

$$\hat{H}_{2M} = \frac{E_c}{2} \hat{n}^2 - E_j \hat{\alpha}_+, \quad (2.47)$$

with

$$\begin{aligned} \hat{n} &= (\hat{c}_r^\dagger \hat{c}_r - \hat{c}_l^\dagger \hat{c}_l)/2, \\ \hat{\alpha}_+ &= \frac{\hat{c}_r^\dagger \hat{c}_l + \hat{c}_l^\dagger \hat{c}_r}{N}. \end{aligned} \quad (2.48)$$

Here,  $\hat{n}$  is the population imbalance (i.e. atom number difference) operator and  $\hat{\alpha}_+$  the tunneling operator. Eq. 2.47 is usually referred to as the Bose-Hubbard Hamiltonian for the double well system. Note, that the atom number operator corresponds to the population difference divided by two. This is due to the fact that the transfer of one particle from one well to the other changes the population imbalance by two and leads in the Gross-Pitaevskii limit to the canonically conjugate variables  $n$  and  $\phi$  as will be discussed in Sec.2.4.1.

### 2.2.1 Energy spectrum of the Bose-Hubbard Hamiltonian

Within the two mode approximation, the Bose-Hubbard Hamiltonian is an exact description of the bosonic Josephson junction and can be solved for particle numbers at which typically our experiments are performed ( $N < 10000$ ).

In this context, the wave function, which describes the state of the system, is defined as an  $(N+1)$ -dimensional vector. In the left/right basis (l/r basis), every entry in the vector corresponds to a single atom number state, where the first entry is the state with  $n = N/2$  corresponding to  $N$  particles in the right well and 0 particles in the left well and the last entry to  $n = -N/2$  corresponding to 0 particles in the right well and  $N$  particles in the left well.

In this basis, the operators can be written in form of  $(N + 1) \times (N + 1)$ -matrices:

$$\hat{n} = \begin{pmatrix} N_0/2 & 0 & 0 & \dots & 0 \\ 0 & N_0/2 - 1 & 0 & \dots & 0 \\ 0 & 0 & N_0/2 - 2 & \dots & 0 \\ \dots & \dots & \dots & \dots & \dots \\ 0 & 0 & 0 & \dots & -N_0/2 \end{pmatrix} \quad (2.49)$$

$$\hat{n}^2 = \begin{pmatrix} (N_0/2)^2 & 0 & 0 & \dots & 0 \\ 0 & (N_0/2 - 1)^2 & 0 & \dots & 0 \\ 0 & 0 & (N_0/2 - 2)^2 & \dots & 0 \\ \dots & \dots & \dots & \dots & \dots \\ 0 & 0 & 0 & \dots & (-N_0/2)^2 \end{pmatrix} \quad (2.50)$$

$$\hat{\alpha}_+ = \begin{pmatrix} 0 & \sqrt{N}/N & 0 & 0 & \dots \\ \sqrt{N}/N & 0 & \sqrt{2(N-1)}/N & 0 & \dots \\ 0 & \sqrt{2(N-1)}/N & 0 & \sqrt{3(N-2)}/N & \dots \\ 0 & 0 & \sqrt{3(N-2)}/N & 0 & \dots \\ \dots & \dots & \dots & \dots & \dots \end{pmatrix} \quad (2.51)$$

$$\hat{H}_{2M} = \begin{pmatrix} \frac{E_c}{2}(N_0/2)^2 & -\frac{E_j}{N}\sqrt{N} & 0 & \dots \\ -\frac{E_j}{N}\sqrt{N} & \frac{E_c}{2}(N_0/2 - 1)^2 & -\frac{E_j}{N}\sqrt{2(N-1)} & \dots \\ 0 & -\frac{E_j}{N}\sqrt{2(N-1)} & \frac{E_c}{2}(N_0/2 - 2)^2 & \dots \\ \dots & \dots & \dots & \dots \end{pmatrix}. \quad (2.52)$$

As mentioned above, the limited size of the Hilbert space allows exact numerical diagonalization of the two mode Hamiltonian. A typical energy spectrum of the many body system at typical experimental parameters is shown in Fig. 2.1 (a). At low energy ( $E < 2E_j$ ), the spectrum is almost linear and the level spacing is approximately given by the plasma frequency

$$\omega_p = \frac{1}{\hbar} \sqrt{E_j \left( E_c + \frac{4E_j}{N^2} \right)}, \quad (2.53)$$

as indicated by the straight dashed line (see also Fig. 2.1 (b), where the energy difference between adjacent atom number states is shown). The corresponding eigenstates are coherent superpositions of atom number states and are similar to the discretized characteristic wave functions of the harmonic oscillator with a Gaussian envelope multiplied by the Hermite polynomials. For higher lying states ( $E > 2E_j$ ), the eigenenergies are grouped two by two. Each doublet of almost degenerate eigenstates consists of a symmetric and an antisymmetric combination of two well defined atom number states. However, even for a very small asymmetry of the trapping potential, the degeneracy is lifted and the two eigenstates become spatially localized states, one in the left well, one in the right well. The energy of these states is dominated by the charging energy term and thus increases quadratically with the eigenstate label  $i$  as indicated by the dashed curve with  $E_i = E_j + i^2 \cdot E_c/8$ .

### 2.2.2 Atom number fluctuations and coherence

Two important properties of the eigenstates of the Bose-Hubbard Hamiltonian are their atom number fluctuations and their coherence, as discussed in different publications, see for

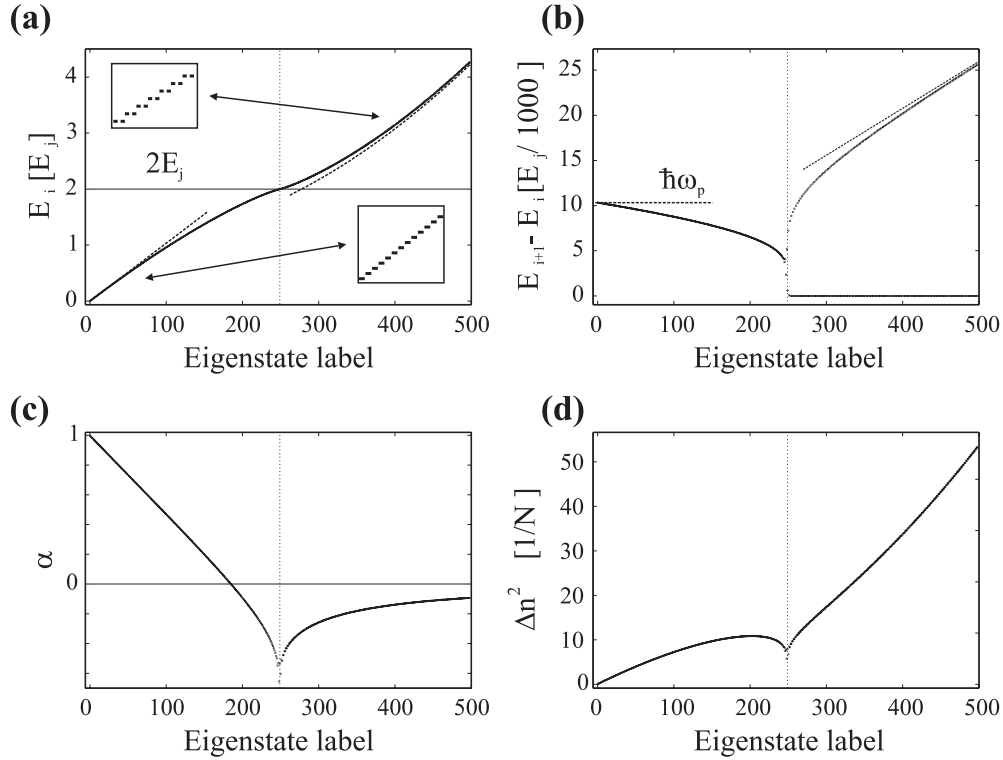


Figure 2.1: First 500 energy eigenvalues and eigenstates of the two mode Hamiltonian in the Josephson regime ( $E_c = 0.016$  nK,  $E_j = 149$  nK and 1150 atoms). (a) shows the eigenenergy spectrum. For the lower eigenstates the energy increases linearly with the plasma energy  $E_i = \hbar\omega_p \cdot i$  (dashed line). For higher eigenstates the energy increases quadratically with  $E_i = E_j + i^2 \cdot E_c/8$  (dashed curve) and every energy eigenvalue corresponds to two degenerate modes. The transition between the two regimes takes place at  $2E_j$ . (b) shows eigenenergy differences as a function of the eigenstate label. The two regimes are again indicated by dashed lines. Above  $2E_j$ , the energy difference splits into two separated curves corresponding to the degeneracy of the higher states. In (c), the coherence of the eigenstates  $\alpha = \langle \hat{c}_l^\dagger \hat{c}_r + \hat{c}_r^\dagger \hat{c}_l \rangle / N$  is shown. It reveals, that for low energies the states are coherent but for higher energies the coherence decreases, becomes negative and then approaches zero. (d) is a plot of the atom number fluctuations which are small for low energies but increase for higher energies.

example [30, 65, 66, 67, 68, 69]. The fluctuation of the atom number difference is defined as

$$\Delta n^2 = \langle \hat{n}^2 \rangle - \langle \hat{n} \rangle^2 = \left\langle \left( \frac{\hat{c}_r^\dagger \hat{c}_r - \hat{c}_l^\dagger \hat{c}_l}{2} \right)^2 \right\rangle - \left\langle \left( \frac{\hat{c}_r^\dagger \hat{c}_r - \hat{c}_l^\dagger \hat{c}_l}{2} \right) \right\rangle^2, \quad (2.54)$$

and is a measure for the number of occupied atom number states. Small fluctuations correspond to well defined atom numbers in both wells.

The coherence can be quantitatively defined in terms of the first order spatial correlation function  $g^{(1)}(\mathbf{r}, \mathbf{r}')$ . In the two mode approximation, it follows from Eq. 2.36 that the first order spatial correlation function does not depend on the difference  $(\mathbf{r} - \mathbf{r}')$  and thus is constant in space [30]. With this, the coherence factor  $\alpha$  can be defined as the uniform value

of the spatial correlation function

$$\begin{aligned}\alpha &= g^{(1)}(\mathbf{r}, \mathbf{r}') = \frac{\langle \hat{\Psi}^\dagger(\mathbf{r}') \hat{\Psi}(\mathbf{r}) \rangle}{\sqrt{\langle \hat{\Psi}^\dagger(\mathbf{r}') \hat{\Psi}(\mathbf{r}') \rangle \langle \hat{\Psi}^\dagger(\mathbf{r}) \hat{\Psi}(\mathbf{r}) \rangle}} \\ &= \frac{\langle \hat{c}_l^\dagger \hat{c}_r + \hat{c}_r^\dagger \hat{c}_l \rangle}{N} = \frac{\langle \hat{c}_g^\dagger \hat{c}_g - \hat{c}_e^\dagger \hat{c}_e \rangle}{N} = \langle \hat{\alpha}_+ \rangle.\end{aligned}\quad (2.55)$$

In Fig. 2.1 (c) and (d), the coherence and the fluctuations of the atom number difference of the eigenstates for typical experimental parameters are shown. The first eigenstates show a high degree of coherence and only a small amount of atom number fluctuations. With increasing energy, however, the coherence decreases and becomes negative. Its lowest value is reached at  $2E_j$ . A negative coherence can be interpreted as the population inversion of the two relevant states in analogy to e.g. a negative temperature of a spin system. In this case, the distribution of the relative phases is localized around  $\pi$ . The atom number fluctuations increase initially slowly, are then slightly reduced again close to  $2E_j$  and increase faster above.

The coherence is directly connected to the relative population difference between the ground and the first excited single particle state, and is a measure for the coupling between the atom number states. The eigenstates of the tunneling operator  $\hat{\alpha}_+$  are the 'SU(2) coherent states', which can be written in the  $1/r$  basis as [70, 71, 72]

$$|c\rangle = \frac{1}{\sqrt{N! \cdot N^N}} \left( \psi_l \hat{c}_l^\dagger + \psi_r \hat{c}_r^\dagger \right)^N |vac\rangle, \quad (2.56)$$

where  $\psi_{l,r}$  are complex multiplier and account for the population and the 'phase' of the two modes and  $|vac\rangle$  is the vacuum state. The state with the highest possible coherence fulfills  $\hat{\alpha}_+|c\rangle = 1|c\rangle$  and corresponds to  $\psi_l = \psi_r = \sqrt{N}/2$ . This state is the ground state of the double well potential in the non-interacting limit and corresponds to all particles occupying the ground state of the potential.

The coherence factor  $\alpha = \langle \hat{\alpha}_+ \rangle$  defined in Eq. 2.55 can also be understood as the mean fringe visibility of ensemble averaged interference patterns. These interference patterns can be visualized either as the interference of the two matter wave packets originating from the two wells, or equivalently as the density distribution of the ensemble after ballistic expansion. As discussed in Sec. 2.1.3 the density distribution is transformed during free expansion and its shape becomes similar to the momentum distribution. In steady state, the ensemble averaged momentum distribution (see Sec. 2.3.3) is given by

$$\langle \hat{\rho}(\mathbf{k}) \rangle = \frac{N}{2} \left( |\Phi_g|^2 + |\Phi_e|^2 + \langle \hat{\alpha}_+ \rangle (|\Phi_g|^2 - |\Phi_e|^2) \right). \quad (2.57)$$

The equivalence between the coherence factor and the mean fringe visibility can be established by approximating the momentum distribution of the ground state by  $\Phi_g(\mathbf{k}) = f(\mathbf{k}) \cdot \cos(\mathbf{k} \cdot \mathbf{d}_{sw})$  (Eq. 2.76) and the first excited state by  $\Phi_e(\mathbf{k}) = f(\mathbf{k}) \cdot \sin(\mathbf{k} \cdot \mathbf{d}_{sw})$  (Eq. 2.77), where  $f(\mathbf{k})$  is an envelope function and  $\mathbf{d}_{sw}$  is the vector connecting the maxima of the two localized matter wave packets. With this the approximated momentum distribution can be written as (see Sec. 2.3.3)

$$\langle \hat{\rho}(\mathbf{k}) \rangle \approx \frac{N|f(\mathbf{k})|^2}{2} \left( 1 + \langle \hat{\alpha}_+ \rangle \cdot \cos(2\mathbf{k} \cdot \mathbf{d}_{sw} - \phi) \right), \quad (2.58)$$

where  $\phi = \phi_l - \phi_r$  is the phase difference between the left and the right matter wave packet, as will be discussed in Sec. 2.4. In Eq. 2.58,  $\langle \hat{\alpha}_+ \rangle$  corresponds to the visibility of the momentum

distribution which is also the visibility of the interference patterns, if the interactions do not perturb the distribution during expansion. A discussion on how interference patterns are obtained experimentally is given in Sec. 3.3.

### 2.2.3 Rabi, Josephson and Fock regime

The properties of the ground state of the Bose-Hubbard Hamiltonian (Eq. 2.42) depend strongly on the ratio of the local interaction energy and the tunneling coupling  $E_c/E_j$ . For strong interaction the ground states is a well defined atom number state and the coherence is low. In the case of strong tunneling coupling the coherence is high and the state is a coherent superposition of many atom number states. The transition between the two regimes is shown in Fig. 2.2 (a), where the coherence (upper graph) and the atom number fluctuations (lower graph) are plotted as a function of  $E_c/E_j$ . Fig. 2.2 (b) shows the distribution of atom number states (upper part) and the ensemble averaged momentum distributions (lower graphs) for three different ratios of  $E_c/E_j$ . It becomes evident that by increasing the ration  $E_c/E_j$  the atom number fluctuations vanish before the coherence of the system is decreased. The atom number fluctuations start to vanish for  $E_c/E_j > N^{-2}$ , however the visibility of the averaged interference patterns and thus the coherence starts only to decrease for  $E_c/E_j > 1$ . By noticing this property of the ground state of the BJJ three regimes can be distinguished, where (1) the coherence is very high and the atom number fluctuations are large, (2) the coherence is high and the atom number fluctuations are small and (3) the coherence is low and the atom number fluctuations vanish. It is convenient to define these three regimes in terms of the ratio  $E_c/E_j$  [33, 73].

- (1) *Rabi* regime :  $E_c/E_j \ll N^{-2}$
- (2) *Josephson* regime :  $N^{-2} \ll E_c/E_j \ll 1$
- (3) *Fock* regime :  $1 \ll E_c/E_j$

The *Rabi* regime corresponds to the non-interacting limit, where the system consists of  $N$  independent particles. The distribution of atom number states is Poissonian and the coherence is very high allowing for the definition of a relative phase between the matter wave packets within the two wells. The *Josephson* regime can be understood as the 'classical' regime. Here the fluctuations of the atom numbers are small and the coherence is high leading to a relative phase with only small quantum mechanical uncertainty. In this regime, for large atom numbers, the operators might be exchanged by complex numbers and the state of the system described in terms of a mean field model. In the *Fock* regime, the Josephson junction is dominated by the interaction energy. Therefore, the eigenstates have a well defined atom number in each well and as the coherence vanishes, the phase is completely undefined. In this regime, the ground state can not be described by a single condensate, where the single particle density matrix has only one macroscopic eigenvalue [52], but corresponds to a fragmented state, where the single particle density matrix has two macroscopic eigenvalues [29, 30, 31].

## 2.3 The phase operator

The mean field description can be used to approximate the bosonic Josephson junction if the coherence of the system is high and a relative phase between the two matter wave packets is

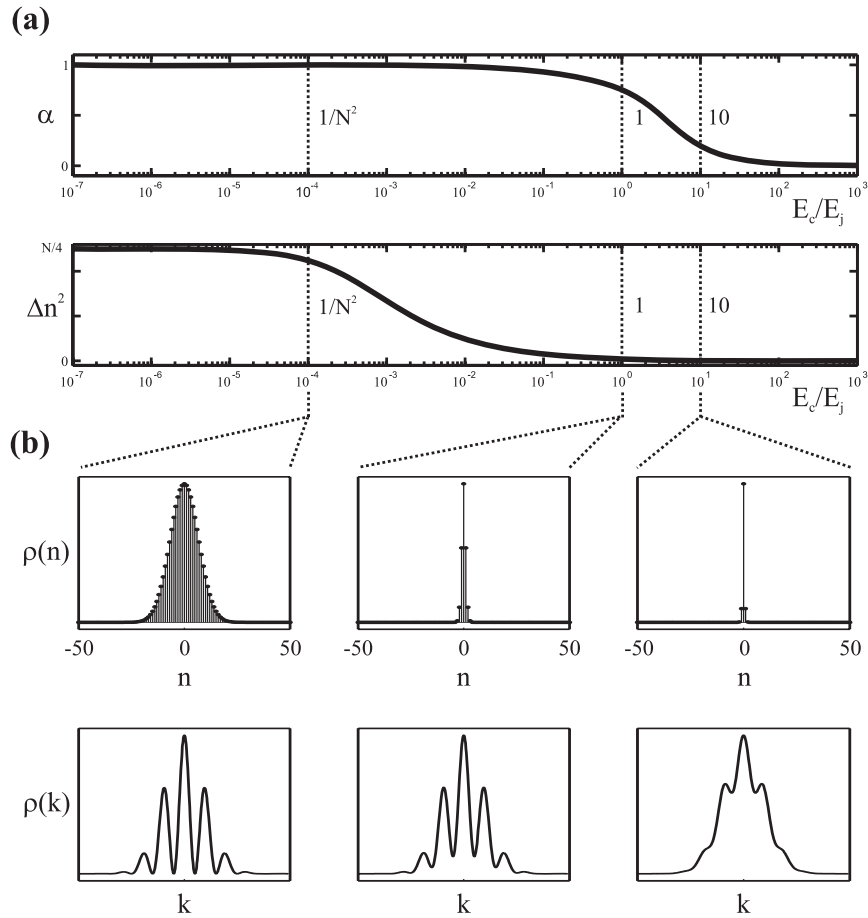


Figure 2.2: Properties of the bosonic Josephson junction for  $N = 100$ . The upper graph in (a) shows the coherence factor  $\alpha$  as a function of  $E_c/E_j$ . The coherence starts to decrease at  $E_c/E_j \gtrsim 1$ . The lower graph in (a) is a plot of the population imbalance fluctuations  $\Delta n^2$  as a function of  $E_c/E_j$ . The fluctuations start to decrease at  $E_c/E_j \gtrsim N^{-2}$ . (b) shows the distribution of atom number states (upper part) and the ensemble averaged momentum distributions (lower graphs) for three different ratios of  $E_c/E_j$ . The visibility of the modulation of the momentum distribution is directly related to the coherence factor. At  $E_c/E_j = N^{-2}$  the atom number fluctuations are large ( $\Delta n \approx \sqrt{N}/2$ ) and the visibility is almost perfect ( $\alpha \approx 1$ ). At  $E_c/E_j = 1$  the atom number fluctuations are strongly reduced but the visibility is still high. At  $E_c/E_j = 10$  the atom number fluctuations are reduced further and the visibility starts to vanish.

well defined. However, in the context of the many body description, it is not straight forward to understand the meaning of a phase and to define a phase operator. To get an idea on the role of the phase in the Bose-Hubbard formalism, it is instructive to revert to a discussion by Dirac concerning the properties of the electromagnetic field [74]. He pointed out that in the quantized electromagnetic field, the photon number and the phase of the field are conjugate variables. They obey the canonical commutation relation

$$[\hat{\phi}, \hat{N}] = -i \quad (\text{leading to } \Delta N \times \Delta \phi \geq 1/2). \quad (2.59)$$

In experiments, only periodic functions of the phase can be measured and thus new phase operators should be introduced [75] by defining the creation and annihilation operators in

terms of lowering  $\widehat{e^{i\phi}}$  and raising operators  $\widehat{e^{-i\phi}}$

$$\begin{aligned}\hat{a} &= \widehat{e^{i\phi}} \widehat{N}^{1/2}, \\ \hat{a}^\dagger &= \widehat{N}^{1/2} \widehat{e^{-i\phi}},\end{aligned}\tag{2.60}$$

With this, also the cosine and sine operators are introduced [76]. They obey the expected commutations relations

$$\begin{aligned}\left[\widehat{\cos\phi}, \widehat{N}\right] &= i \cdot \widehat{\sin\phi}, \\ \left[\widehat{\sin\phi}, \widehat{N}\right] &= -i \cdot \widehat{\cos\phi}.\end{aligned}\tag{2.61}$$

For large atom numbers, these operators must reproduce the classical expectation values for  $\cos\phi$  and  $\sin\phi$ . However, these conditions are not sufficient to define the operators, also the trigonometric identity has to be fulfilled [77, 78]

$$\langle \widehat{\cos\phi}^2 \rangle + \langle \widehat{\sin\phi}^2 \rangle = 1.\tag{2.62}$$

Usually not the phase of an electromagnetic field but the relative phase between two overlapping electromagnetic fields is measured. Thus, it is useful to define the relative phase operator of two fields, which is approximated in terms of creation and annihilation operators of the two fields by

$$\widehat{\cos\phi} = \frac{\hat{c}_1^\dagger \hat{c}_2 + \hat{c}_2^\dagger \hat{c}_1}{\sqrt{N(N+2) - 4\langle \hat{n}^2 \rangle}}\tag{2.63}$$

$$\widehat{\sin\phi} = \frac{(\hat{c}_1^\dagger \hat{c}_2 - \hat{c}_2^\dagger \hat{c}_1)}{i\sqrt{N(N+2) - 4\langle \hat{n}^2 \rangle}},\tag{2.64}$$

where  $\hat{c}_1^\dagger$  and  $\hat{c}_2^\dagger$  are the creation operators of photons in the two electromagnetic fields and the normalization factor  $\sqrt{N(N+2) - 4\langle \hat{n}^2 \rangle}$  is a consequence of the trigonometric identity (Eq. 2.62).

The same arguments are also applicable to atomic systems leading to the definition of a relative phase operator between two Bose-Einstein condensates. In the limit of large atom numbers ( $N(N+2) \approx N^2$ ), equal population of both modes  $\langle \hat{n} \rangle = 0$ , and small atom number fluctuations ( $\Delta n^2 \ll N^2$ ), the expectation value of the phase operators  $\widehat{\cos\phi}$  and  $\widehat{\sin\phi}$  become equivalent to the tunneling operators

$$\langle \widehat{\cos\phi} \rangle \approx \langle \hat{\alpha}_+ \rangle\tag{2.65}$$

$$\langle \widehat{\sin\phi} \rangle \approx \langle \hat{\alpha}_- \rangle,\tag{2.66}$$

where the second tunneling operator is defined as

$$\hat{\alpha}_- = \frac{(\hat{c}_l^\dagger \hat{c}_r - \hat{c}_r^\dagger \hat{c}_l)}{iN}.\tag{2.67}$$

In general, however, the eigenstates of the Bose-Hubbard Hamiltonian do not correspond to 'phase states', which means that  $\langle \widehat{\cos\phi}^2 \rangle - \langle \widehat{\cos\phi} \rangle^2 \neq 0$  and thus, the state is not characterized by a single phase, but by a phase distribution. This can be directly seen from the

expectation value of the sine operator. For eigenstates of the Bose-Hubbard Hamiltonian  $\langle \cos\phi \rangle$  varies between  $-1$  and  $1$  as expected for  $\cos\phi$  for  $-\pi \leq \phi \leq \pi$  but  $\langle \sin\phi \rangle = 0$  for all eigenstates. Thus, the distribution of phases in the case of eigenstates is always symmetric due to the symmetry of the Hamiltonian<sup>2</sup>.

Only a coherent superposition of different eigenstates might have a non-vanishing value of  $\langle \sin\phi \rangle$ . The coherent superposition of non-degenerate eigenstates however, is not static but evolves in time. Thus, a relative phase ( $\phi \neq 0$  and  $\phi \neq \pm\pi$ ) is always connected to kinetic energy and with it to a flux of particles from one to the other well.

Note that care has to be taken with this formulation of the phase operator. There are difficulties arising from the definition, e.g.  $e^{i\hat{\phi}}$  is not unitary as  $e^{i\hat{\phi}}|0\rangle = 0$  and thus the phase operator is not hermitian. Furthermore, due to the commutation relation the matrix elements of the phase operator in the atom number basis are not well defined, as  $\langle n|\hat{\phi}|n'\rangle(n' - n) = -i\delta_{n,n'}$ . Thus, the operator  $\hat{\phi}$  corresponds only approximately to the phase operator. However, if  $\hat{\phi}$  appears in combination with the atom number operator (in terms of creation and annihilation operators) the expectation values are always well behaved.

### 2.3.1 Phase states

To overcome the difficulties discussed above, the phase operator might be defined in terms of a projection onto phase states instead. The phase states can be directly found by realizing that conjugate variables are connected via a Fourier-transformation. In the discrete atom number basis, the phase state with the relative phase  $\phi$  between the two matter wave packets in the left and the right well is given by

$$|\phi\rangle = \frac{1}{\sqrt{F_\phi}} \sum_{n=-N/2}^{N/2} \exp(in\phi) |n\rangle, \quad (2.68)$$

where  $F_\phi$  is a normalization constant. With this relation, the atom number states can be expressed in the phase basis as

$$|n\rangle = \frac{1}{\sqrt{F_n}} \sum_{m=0}^N \exp(-in\phi_m) |\phi_m\rangle, \quad (2.69)$$

where  $F_n$  is the normalization of the states,  $\phi_m = \phi_0 + 2\pi m/(N+1)$  are  $N+1$  orthogonal phase states, and  $\phi_0$  is an arbitrary phase defining the range in which the phase is defined. In the following we will set for simplicity  $\phi_0 = -\pi$  to access the range  $\phi \in [-\pi, \pi]$ .

The phase states can also be understood as the 'phase'-part of the SU(2) coherent states (E.q 2.56), which are given by

$$|c_\phi\rangle = \frac{\left(e^{-i\frac{\phi}{2}} \hat{c}_l^\dagger + e^{i\frac{\phi}{2}} \hat{c}_r^\dagger\right)^N}{\sqrt{2^N N!}} |vac\rangle = \sum_{n=-N/2}^{N/2} \sqrt{\frac{N!}{2^N (N/2 - n)! (N/2 + n)!}} \exp(in\phi) |n\rangle, \quad (2.70)$$

where  $\phi$  is the relative phase between the left and the right well as discussed in [79]. Here, the exponential corresponds to a phase between adjacent atom number states and the square-root term to an envelope function. With this, the phase of a phase state can be understood as a constant phase between all neighboring atom number states. In principle, due to their structure, SU(2) coherent states could also be used to define phase states.

<sup>2</sup>This can also be seen from the GP Hamilton function Eq. 2.87 or Eq. 2.93, where the phase appears only as  $\cos\phi$  and is symmetric around  $\phi = 0$ .

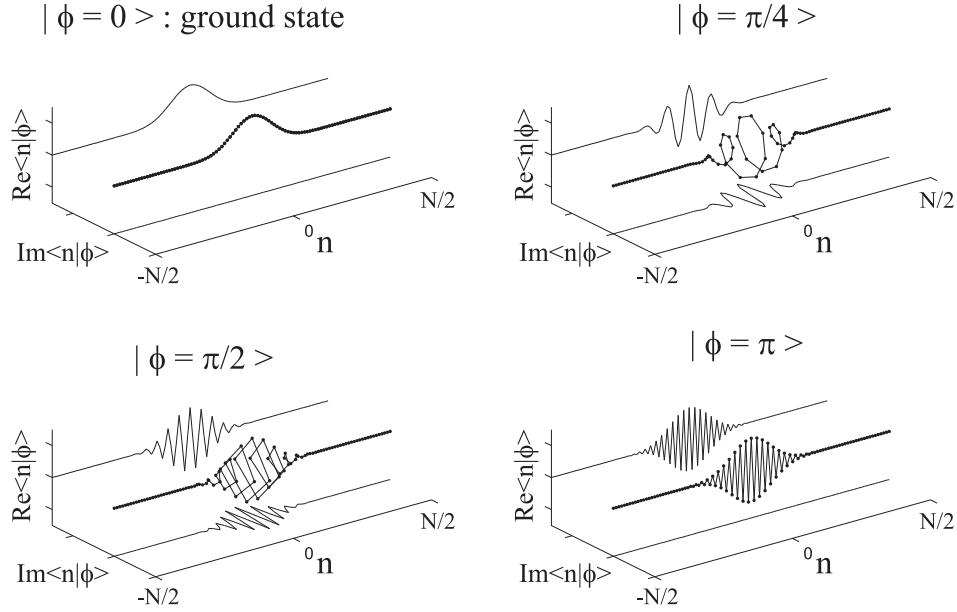


Figure 2.3: SU(2) coherent states. The real and the imaginary parts of the projection of the phase states  $|\phi\rangle$  onto the number states  $|n\rangle$  is shown for four different phases. The phase of the states  $\phi$  corresponds to a fixed phase difference between adjacent atom number states.

The real and the imaginary parts of the projection of four typical SU(2) coherent states onto the  $1/r$  basis are shown in Fig. 2.3. The envelope of the states has a Poissonian profile (resulting from the binomial distribution) and a constant phase relation between adjacent atom number states, where the phase difference directly corresponds to the phase of the state.

The problem with the application of the SU(2) coherent states as phase states is their envelope. If a population imbalance  $\langle \hat{n} \rangle \neq 0$  is present, the envelope of the states is shifted, leaving the phase structure unchanged

$$\begin{aligned}
 |\phi_{\langle \hat{n} \rangle}\rangle &= \frac{1}{\sqrt{N!N^N}} \left( \sqrt{N_1} \exp(i\phi) \hat{c}_l^\dagger + \sqrt{N - N_1} \exp(-i\phi) \hat{c}_r^\dagger \right)^N |vac\rangle \\
 &= \sum_{n=-N/2}^{N/2} \sqrt{\frac{N!}{(N/2 - n)! (N/2 + n)!}} \times \\
 &\quad \sqrt{\frac{1}{(N_1/N)^{N/2-n} \cdot (1 - N_1/N)^{N/2+n}}} \exp(in\phi) |n\rangle, \tag{2.71}
 \end{aligned}$$

where  $\langle \hat{c}_l^\dagger \hat{c}_l \rangle = N_1/N$  is the expectation value of the population of the left well and  $\langle \hat{c}_r^\dagger \hat{c}_r \rangle = 1 - N_1/N$  the expectation value for the right well. Thus, a large population imbalance will lead to a large shift of the envelope function and the overlap integrals will become very small, even if the coherence of the state is high. To overcome this problem and to define feasible phase states, all amplitudes should be set to the same value, which leads exactly to the definition of the phase states from above (Eq. 2.68).

The phase distribution for any state can be calculated by a projection onto the phase states via  $n(\phi_m) = |\langle \phi_m | \Psi \rangle|^2$ . Typical distributions of the relative phase for the many body ground state for different  $E_c/E_j$  are shown in Fig. 2.4. In steady state the expectation value

of  $\hat{\phi}$  is zero and the width of the distribution increases with  $E_c$ . In the Rabi regime,  $\Delta\phi$  is small and decreases with the number of particles. In the Fock regime, the phase fluctuation increases to its maximal value  $\Delta\phi \lesssim \pi/\sqrt{3}$  corresponding to a random distribution and an undefined phase.

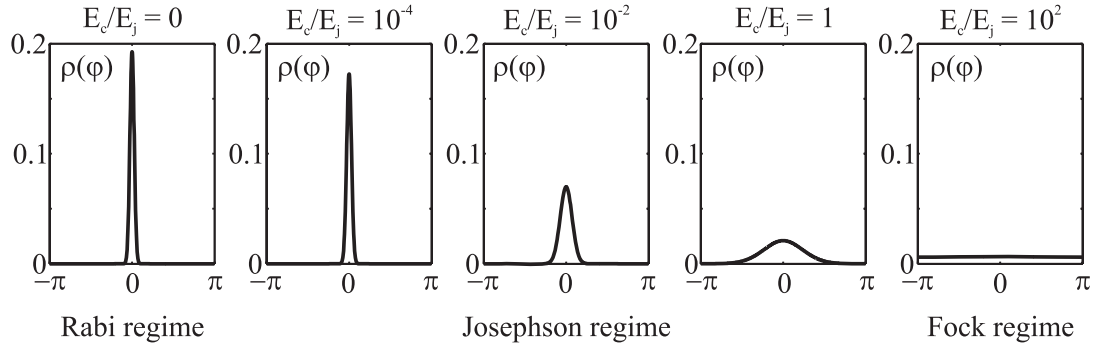


Figure 2.4: Distribution of the relative phases for different ratio of  $E_c/E_j$  for  $N = 100$ . The five graphs show typical distribution of the relative phase for the three regimes, the Rabi regime on the left, the Josephson regime in the center and the Fock regime on the right. In the Rabi regime the width of the distribution is only determined by the number of particles. In the Josephson regime also the ratio of the interaction energy and the coupling strength plays a role. In the Fock regime the relative phase becomes random.

Expectation values depending on the relative phase can be calculated using the distribution function. The expectation values of e.g. the phase operator  $\hat{\phi}$ , the phase fluctuation operator  $\hat{\phi}^2$  and the cosine of the phase operator  $\cos \hat{\phi}$  are

$$\begin{aligned}
 \langle \hat{\phi} \rangle &= \sum_{m=0}^N \phi |\langle \phi_m | \Psi \rangle|^2, \\
 \langle \hat{\phi}^2 \rangle &= \sum_{m=0}^N \phi^2 |\langle \phi_m | \Psi \rangle|^2, \\
 \langle \cos \hat{\phi} \rangle &= \sum_{m=0}^N \cos \phi |\langle \phi_m | \Psi \rangle|^2.
 \end{aligned} \tag{2.72}$$

The expectation values of  $\langle \cos \hat{\phi} \rangle$  and  $\langle \widehat{\cos \phi} \rangle$  become equivalent for large atom numbers. However, numerically it is much easier to compute the second quantity, as here only one expectation value has to be calculated rather than the projection of the state onto the phase basis. Thus, the computation of the projection is only necessary, if the expectation value of the phase or the phase distribution itself are of relevance. If only the cosine and the sine operators are involved, the definitions Eq. 2.63 and Eq. 2.64 should be considered, as will be discussed in the following section.

### 2.3.2 Comparison of the different phase operators

The necessity of defining the phase operator as  $\widehat{\cos \phi}$  rather than  $\hat{\alpha}_+$  can be seen in Fig. 2.5. In this graph the expectation values of the two operators are shown for different phase states and for three different imbalances. In the symmetric case, both expectation values ( $\widehat{\cos \phi}$  dotted line and  $\hat{\alpha}_+$  dashed line) agree well with the classical expectation of  $\cos \phi$  (solid line).

However, for imbalanced states the value of  $\hat{\alpha}_+$  is reduced until for large imbalances the expectation value vanishes.  $\langle \widehat{\cos\phi} \rangle$  stays very close to the classical limit until almost all particles are in average in one well. Thus, the definition of the cosine operator in terms of Eq. 2.61 is a good approximation for the phase of the state, even in the case of an imbalance between the two modes. The same discussion is also valid for the expectation value of the sine operator  $\widehat{\sin\phi}$  and the second tunneling operator  $\hat{\alpha}_-$ .

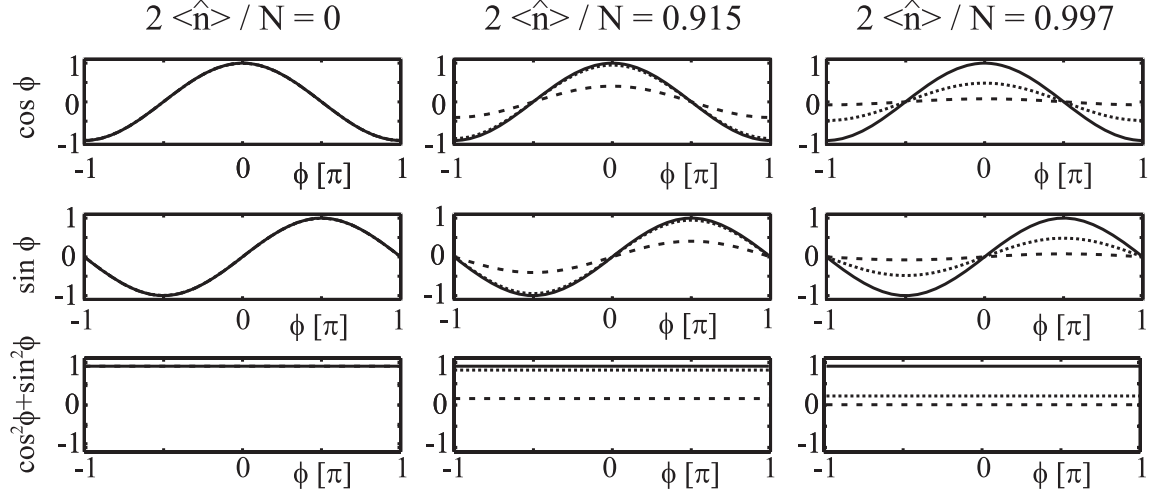


Figure 2.5: Expectation values for  $\hat{\alpha}_+$ ,  $\widehat{\cos\phi}$ ,  $\hat{\alpha}_-$  and  $\widehat{\sin\phi}$  for the SU(2) coherent states for three different population imbalances. The upper part compares the expectation values of  $\hat{\alpha}_+$  (dashed line) and  $\widehat{\cos\phi}$  (dotted line) with the classical value of  $\cos\phi$  (solid line). The central part shows the expectation values of  $\hat{\alpha}_-$  (dashed line),  $\widehat{\sin\phi}$  (dotted line) and the classical value  $\sin\phi$  (solid line). The graphs reveals, that the operators  $\widehat{\cos\phi}$  and  $\widehat{\sin\phi}$  correspond to the phase of the states even for situations, where the atom number difference is large. However, for large population imbalances the expectation value of  $\hat{\alpha}_+$  and  $\hat{\alpha}_-$  are strongly affected. The lower graphs show  $\langle \widehat{\alpha}_+ \rangle^2 + \langle \widehat{\alpha}_- \rangle^2$  (dotted line) and  $\langle \widehat{\cos\phi} \rangle^2 + \langle \widehat{\sin\phi} \rangle^2$  (dashed line). The phase operators are close to the classically expected value of one (solid line) also for situations, where the population imbalance is not zero.

The lower graphs in Fig. 2.5 show the trigonometric identity  $\cos^2\phi + \sin^2\phi$  (the classical expectation is one, indicated by the solid line). The identity stays close to one for  $\widehat{\cos\phi}$  and  $\widehat{\sin\phi}$  but deviates for  $\hat{\alpha}_+$  and  $\hat{\alpha}_-$ . The value of the latter quantity  $\langle \widehat{\alpha}_+ \rangle^2 + \langle \widehat{\alpha}_- \rangle^2$  corresponds to the visibility of a single interference pattern as will be discussed in the next section and agrees very well with the classical expectation of  $\nu = 2\sqrt{N_1 N_2}/N^2$ .

### 2.3.3 Momentum distribution in the double well

The relative phase between two localized matter wave packets in a double well potential can not be measured directly. However, as the phase is connected to the momentum distribution of the particles, it is revealed in interference experiments. The momentum distribution is given by

$$\langle \hat{\rho}(\mathbf{k}) \rangle = \langle \hat{\Psi}^\dagger(\mathbf{k}) \hat{\Psi}(\mathbf{k}) \rangle. \quad (2.73)$$

Applying the two mode approximation by rewriting the wave function as

$$\hat{\Psi}(\mathbf{k}) = \frac{\hat{c}_l}{\sqrt{2}} \left( \Phi_g(\mathbf{k}) + \Phi_e(\mathbf{k}) \right) + \frac{\hat{c}_r}{\sqrt{2}} \left( \Phi_g(\mathbf{k}) - \Phi_e(\mathbf{k}) \right), \quad (2.74)$$

where  $\Phi_g(\mathbf{k}), \Phi_e(\mathbf{k})$  are the wave functions of the ground and the first excited state in momentum space, leads to the resulting momentum distribution

$$\begin{aligned}
 \langle \hat{\rho}(\mathbf{k}) \rangle &= \frac{N}{2} (|\Phi_g|^2 + |\Phi_e|^2) - \langle \hat{n} \rangle (\Phi_g^* \Phi_e + \Phi_g \Phi_e^*) \\
 &+ \frac{\langle \hat{c}_l^\dagger \hat{c}_r + \hat{c}_l \hat{c}_r^\dagger \rangle}{2} (|\Phi_g|^2 - |\Phi_e|^2) \\
 &- \frac{\langle \hat{c}_l^\dagger \hat{c}_r - \hat{c}_l \hat{c}_r^\dagger \rangle}{2} (\Phi_g^* \Phi_e - \Phi_g \Phi_e^*) \\
 &= \frac{N}{2} \left( |\Phi_g|^2 + |\Phi_e|^2 - \frac{2 \langle \hat{n} \rangle}{N} (\Phi_g^* \Phi_e + \Phi_g \Phi_e^*) \right. \\
 &\left. + \langle \hat{\alpha}_+ \rangle (|\Phi_g|^2 - |\Phi_e|^2) - i \langle \hat{\alpha}_- \rangle (\Phi_g^* \Phi_e - \Phi_g \Phi_e^*) \right). \tag{2.75}
 \end{aligned}$$

If the state has high coherence ( $\alpha \approx 1$ ), the expectation values  $\langle \hat{\alpha}_+ \rangle$  and  $\langle \hat{\alpha}_- \rangle$  are equivalent to  $\cos \phi$  and  $\sin \phi$  as discussed in Sec. 2.3. If the coherence is reduced, the expectation values are still proportional to  $\cos \phi$  and  $\sin \phi$  but at a reduced amplitude. This reduction is described in terms of an additional numeric factor, which can be understood as the ideal visibility<sup>3</sup> of the interference patterns.

Due to the fact that the two functions  $|\Phi_g|^2 - |\Phi_e|^2$  and  $i(\Phi_g \Phi_e^* - \Phi_g^* \Phi_e)$  are orthogonal, the relative phase is directly revealed in the momentum distribution. The role of the relative phase in the interference experiments can be visualized by considering large atom numbers and a symmetric double well. Here, the ground state wave function is symmetric with a spatially constant phase leading to a real and symmetric momentum distribution

$$\Phi_g(\mathbf{k}) = f(\mathbf{k}) \cdot \cos(\mathbf{k} \cdot \mathbf{d}_{sw}), \tag{2.76}$$

with  $f(\mathbf{k})$  being an envelope function and  $\mathbf{d}_{sw}$  is the vector associated with the distance between the maxima of the two matter wave packets. The envelope is typically of Gaussian shape. The wave function of the first excited state is antisymmetric leading to an imaginary and antisymmetric momentum distribution

$$\Phi_e(\mathbf{k}) = f(\mathbf{k}) \cdot i \sin(\mathbf{k} \cdot \mathbf{d}_{sw}). \tag{2.77}$$

With this, the resulting total momentum distribution is given by

$$\begin{aligned}
 \langle \hat{\rho}(\mathbf{k}) \rangle &= \frac{N|f(\mathbf{k})|^2}{2} \left( 1 + \langle \hat{\alpha}_+ \rangle (2 \cos^2(\mathbf{k} \cdot \mathbf{d}_{sw}) - 1) - i \langle \hat{\alpha}_- \rangle 2i \cos(\mathbf{k} \cdot \mathbf{d}_{sw}) \sin(\mathbf{k} \cdot \mathbf{d}_{sw}) \right) \\
 &= \frac{N|f(\mathbf{k})|^2}{2} \left( 1 + \langle \hat{\alpha}_+ \rangle \cos(2\mathbf{k} \cdot \mathbf{d}_{sw}) + \langle \hat{\alpha}_- \rangle \sin(2\mathbf{k} \cdot \mathbf{d}_{sw}) \right) \\
 &= \frac{N|f(\mathbf{k})|^2}{2} \left( 1 + \nu \cdot \cos \phi \cos(2\mathbf{k} \cdot \mathbf{d}_{sw}) + \nu \cdot \sin \phi \sin(2\mathbf{k} \cdot \mathbf{d}_{sw}) \right) \\
 &= \frac{N|f(\mathbf{k})|^2}{2} \left( 1 + \nu \cdot \cos(2\mathbf{k} \cdot \mathbf{d}_{sw} - \phi) \right), \tag{2.78}
 \end{aligned}$$

where  $\langle \hat{\alpha}_+ \rangle = \nu \cdot \cos \phi$  and  $\langle \hat{\alpha}_- \rangle = \nu \cdot \sin \phi$  corresponds to the decomposition of the expectation values into an amplitude and a mean relative phase. The visibility  $\nu$  corresponds to

<sup>3</sup>Ideal in this context refers to the highest experimentally achievable visibility without additional experimental uncertainties.

the amplitude of the modulation in the interference patterns and the relative phase  $\phi$  to the position of the interference peaks with respect to the envelope function  $f(\mathbf{k})$ .

Also the role of the tunneling operators can be understood from this discussion. Their expectation values might be decomposed into the product of two operators, namely the phase operator and the visibility operator

$$\langle \hat{\alpha}_+ \rangle = \langle \hat{\nu} \rangle \times \langle \widehat{\cos\phi} \rangle \quad (2.79)$$

which rewritten in terms of creation and annihilation operators are given by

$$\left\langle \frac{\hat{c}_l^\dagger \hat{c}_r + \hat{c}_r^\dagger \hat{c}_l}{N} \right\rangle = \left\langle \frac{\sqrt{N(N+2) - \langle \hat{n}^2 \rangle}}{N} \right\rangle \times \left\langle \frac{\hat{c}_l^\dagger \hat{c}_r + \hat{c}_r^\dagger \hat{c}_l}{\sqrt{N(N+2) - \langle \hat{n}^2 \rangle}} \right\rangle. \quad (2.80)$$

Thus, the coherence in steady state is equivalent to the visibility of the interference patterns as  $\langle \widehat{\cos\phi} \rangle \approx 1$ , however in general the visibility can only be accessed by the sum of both expectation values squared

$$\langle \hat{\nu} \rangle^2 \approx \langle \hat{\alpha}_+ \rangle^2 + \langle \hat{\alpha}_- \rangle^2 = \langle \hat{\nu} \rangle^2 \times \langle \widehat{\cos\phi} \rangle^2 + \langle \hat{\nu} \rangle^2 \times \langle \widehat{\sin\phi} \rangle^2. \quad (2.81)$$

### 2.3.4 Matter wave interference - projection onto SU(2) coherent states

The eigenstates of the bosonic Josephson junction correspond to the symmetric population of phase states around zero. Thus, the measurement of interference patterns from steady state should according to this argument always lead to a relative phase of zero. The width of the phase distribution might only affect the visibility of the resulting patterns. However, in interference experiments not the original momentum distribution is measured, but the state is altered during the measurement process. The measurement of a single interference pattern results in the projection of the states onto SU(2) coherent states as was as pointed out in [80, 81]. Even in the case of two initial Fock states, where no relative phase can be defined, the interference experiments will lead to the observation of patterns with very high visibility, which is a consequence of the interference measurement process itself. The two condensates in the Fock states are expressed in the atom number basis as  $|N_1, N_2\rangle$ . In the most simple description, the interference experiment acts as a 50:50 beam splitter, after which the particles are detected either in the symmetric channel (+) :  $(\hat{c}_l + \hat{c}_r)$  or in the antisymmetric channel (-) :  $(\hat{c}_l - \hat{c}_r)$ . The detection of the first particle in the (+) channel will lead to the state

$$(\hat{c}_l + \hat{c}_r)|N_1, N_2\rangle = \sqrt{N_1}|N_1 - 1, N_2\rangle + \sqrt{N_2}|N_1, N_2 - 1\rangle. \quad (2.82)$$

The detection of the second particle in the same channel will lead to the state

$$\begin{aligned} (\hat{c}_l + \hat{c}_r) & \left( \begin{array}{l} \sqrt{N_1}|N_1 - 1, N_2\rangle + \sqrt{N_2}|N_1, N_2 - 1\rangle \\ = \sqrt{N_1(N_1 - 1)}|N_1 - 2, N_2\rangle \\ + 2\sqrt{N_1 N_2}|N_1 - 1, N_2 - 1\rangle \\ + \sqrt{N_2(N_2 - 1)}|N_1, N_2 - 2\rangle, \end{array} \right) \end{aligned} \quad (2.83)$$

and so on. With this the atom number states with an undefined phase are projected during the measurement with every detected particle further and further onto SU(2) coherent states, for which a relative phase is well defined.

The extension of this description to a multichannel detection method corresponds to the additional consideration of factors resulting from the path and the probability differences (if  $\langle \hat{n} \rangle \neq 0$ ) for atoms arriving from one or the other well. The measurement thus leads to a projection operator of the form  $(\psi_l \hat{c}_l + \psi_r \hat{c}_r)$  (see Eq. 2.56). With this, the measurement of the interference of two matter waves can be described by the projection of the initial states onto SU(2) coherent states defined in Eq. 2.56. Thus, a clear interference structure is always anticipated for single realizations of interference experiments.

The discussion above shows, that any measured interference pattern reveals a single relative phase. The relative phase is chosen randomly according to the probability distribution, even if the distribution was not localized around a certain value. With this, by repeating the interference experiments the distribution of the relative phases can be mapped out. Expectations values are then calculated by averaging over the respective quantities according to the phase distribution. However, the calculation of the phase distribution in the Bose-Hubbard picture is time-consuming as the density matrix has to be projected onto the phase states. In order to reduce the computation time, if only the sine and/or the cosine operators are involved, also the operators  $\widehat{\sin\phi}$  and  $\widehat{\cos\phi}$  lead to accurate results, even in the case of large population imbalances.

## 2.4 Mean field description - a mechanical analogue

Within the many body two mode model it is possible to calculate all relevant quantities exactly. However, more insight into the behavior of the BJJ can be gained by using a mean field description, where for large atom numbers and in the case of only small quantum mechanical uncertainties of the population imbalance and the relative phase, the creation and annihilation operators might be exchanged by their expectation values. In this description all condensed particles occupy the same quantum mechanical wave function leading to the reduction of the many body Hamiltonian to the Hamiltonian of a single particle. Thus, the mean field model is ideally suited to describe the BJJ in the Josephson regime for large atom numbers, as here both fluctuations  $\Delta n^2 = \langle \hat{n}^2 \rangle - \langle \hat{n} \rangle^2$  and  $\Delta \phi = \langle \hat{\phi}^2 \rangle - \langle \hat{\phi} \rangle^2$  are small<sup>4</sup>. As already mentioned, at these conditions the first two eigenstates can be calculated by solving the Gross-Pitaevskii equation numerically (see Appendix B).

The wave functions in the double well potential in real and in momentum space are compared in Fig. 2.6 (a) and (b) with the corresponding wave functions in a harmonic trap, where the barrier height in the double well potential is set to zero. The structure of the energy spectrum for barrier heights comparable to or much larger than the chemical potential can be understood by this simple picture. The ground state of the harmonic potential as shown in Fig. 2.6 (a) upper graph has a maximum in the center of the trap (dashed line). Its energy is strongly affected if the potential barrier is raised and is split into two localized modes (solid line). The first excited state shown in Fig. 2.6 (b) upper graph has a node in the center and thus the barrier changes the energy of this state only slightly. For high barriers the probability distribution of atoms in the two states become very similar, and differ only in the central region leading to a small energy splitting between these two states. Furthermore, the momentum distributions of the two states are very similar for large barrier heights as shown in Fig. 2.6 (a) and (b) lower graphs, where both wave functions in momentum space have the same envelope but differ only in their symmetry and are approximately expressed

<sup>4</sup>In the Fock regime the mean field description does not hold as the relative phase is not well defined. In the Rabi regime care has to be taken if using the mean field description for finite temperature.

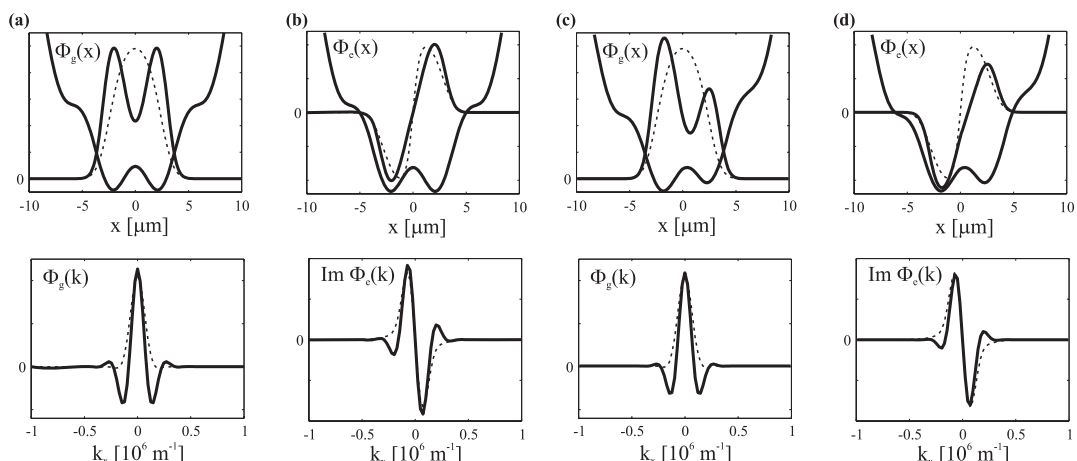


Figure 2.6: First two eigenstates of the double well potential calculated by solving the Gross-Pitaevskii equation in 3-D in a symmetric and an asymmetric potential. The wave functions are shown in real space (upper parts) and in momentum space (lower parts) for  $N = 1150$  and  $\omega_x = 2\pi \times 78$  Hz,  $\omega_y = 2\pi \times 90$  Hz,  $\omega_z = 2\pi \times 66$  Hz,  $V_0/h = 420$  Hz,  $|\mathbf{d}_{sw}| = 5.2\mu\text{m}$ . The asymmetry is generated by moving the periodic potential by  $\Delta x = 500\text{nm}$  with respect to the harmonic potential. The solid lines correspond to the ground state wave function in the symmetric double well (a), the first excited state in the symmetric double well (b), the ground state in the asymmetric double well (c), and the first excited state in the asymmetric double well (d). The dashed lines show the corresponding wave functions in the harmonic trap at  $V_0 = 0$ .

by Eq. 2.76 and Eq. 2.77. This is also expected if the BJJ is considered to be analogous to a double slit for coherent light.

Fig. 2.6 (c) and (d) depict similar plots for the ground state wave function and the first excited state wave function in an asymmetric double well potential. The solid lines in the upper graphs correspond to the wave functions in real space and in the lower graphs to the wave functions in momentum space. The corresponding wave function in the harmonic trap are indicated by the dashed lines. The asymmetry results for both states in a change of the local amplitudes and an increase of the population of the lower well. The wave functions in the momentum space are only slightly affected by the asymmetry.

The observable quantities are not the wave functions but the density and the momentum distribution. Both wave functions in the symmetric case, if considered independently, lead approximately to the same density distribution, i.e. equal population of the left and the right well. In order to be able to describe atom number differences and relative phases between the two wells in the mean field picture, a more convenient choice for the two modes are the coherent superpositions of the ground and the first excited state, namely the left and the right matter wave packets, with the wave functions  $\Phi_l = (\Phi_g + \Phi_e)/\sqrt{2}$  and  $\Phi_r = (\Phi_g - \Phi_e)/\sqrt{2}$ . With this, the full wave function of the BJJ can be written as

$$\Psi = \psi_l \Phi_l + \psi_r \Phi_r = \sqrt{N_l} e^{i\phi_l} \Phi_l + \sqrt{N_r} e^{i\phi_r} \Phi_r, \quad (2.84)$$

where  $\psi_{l,r}$  are complex multiplier,  $N_{l,r}$  is the population of the localized modes and  $\phi_{l,r}$  the phases. The resulting density distribution is

$$n(\mathbf{r}) = N_l |\Phi_l(\mathbf{r})|^2 + N_r |\Phi_r(\mathbf{r})|^2 + \sqrt{N_l N_r} \left( e^{i(\phi_l - \phi_r)} \Phi_l(\mathbf{r}) \Phi_r(\mathbf{r})^* + e^{i(-\phi_l + \phi_r)} \Phi_l(\mathbf{r})^* \Phi_r(\mathbf{r}) \right). \quad (2.85)$$

The overlap between the two wave functions for large barrier heights is small leading to  $\Phi_l \Phi_r^* \approx 0$  and thus to the density distribution  $n(\mathbf{r}) = N_l |\Phi_l(\mathbf{r})|^2 + N_r |\Phi_r(\mathbf{r})|^2$  consisting of  $N_l$  particles in the left well and  $N_r$  in the right well.

The momentum distribution is obtained from the wave function in momentum space leading to the same functional dependence

$$n(\mathbf{k}) = N_l |\Phi_l(\mathbf{k})|^2 + N_r |\Phi_r(\mathbf{k})|^2 + \sqrt{N_l N_r} \left( e^{i(\phi_l - \phi_r)} \Phi_l(\mathbf{k}) \Phi_r(\mathbf{k})^* + e^{i(-\phi_l + \phi_r)} \Phi_l(\mathbf{k})^* \Phi_r(\mathbf{k}) \right), \quad (2.86)$$

however, the overlap of the wave function in momentum space can not be neglected. The first two terms add up to an envelope and the interference term gives rise to a modulation of this envelope by equidistantly spaced peaks, where the position of these interference peaks depends on the relative phase as discussed in Sec. 2.3.3.

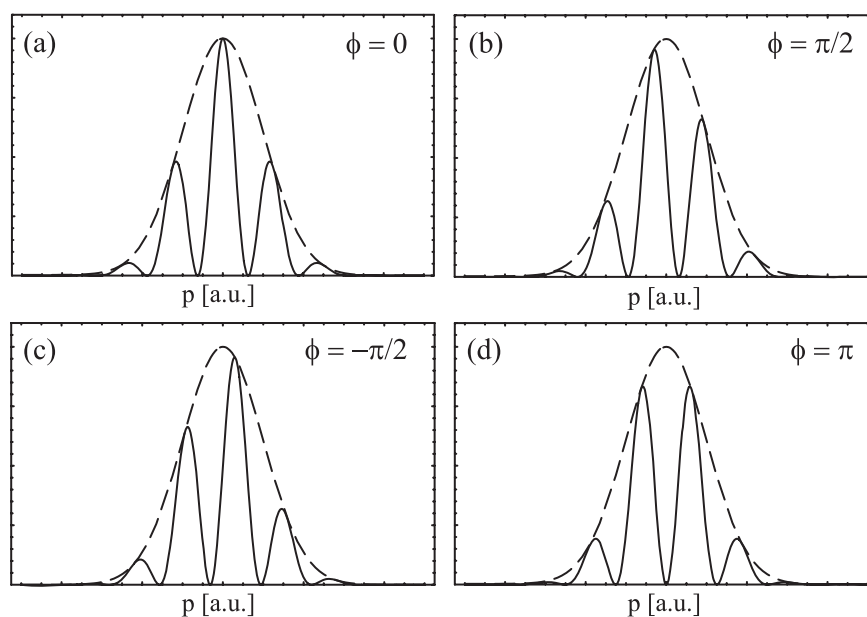


Figure 2.7: Typical momentum distribution at four different relative phases calculated using Eq. 2.78, a zero population imbalance and a Gaussian profile for the envelope (dashed lines). (a) corresponds to the momentum distribution at  $\phi = 0$ , (b) to  $\phi = \pi/2$ , (c) to  $\phi = -\pi/2$  and (d) to  $\phi = \pi$ . The momentum distributions reveal, that the position of the interference peaks with respect to the envelope give information about the relative phase of the two interfering matter waves.

Four typical momentum distributions in a symmetric double well potential are shown in Fig. 2.7. (a) corresponds to the momentum distribution at  $\phi = 0$  which is the momentum distribution of the ground state wave function. (b) and (c) correspond to the relative phase of  $\phi = \pi/2$  and  $\phi = -\pi/2$  and (d) to  $\phi = \pi$ , which is the momentum distribution of the first excited state. If the population imbalance is not zero, the visibility of the interference patterns is reduced.

### 2.4.1 Gross-Pitaevskii equation and the two mode model

The mean field description is not only useful to visualize the density and the momentum distribution of a state but in the Josephson regime, for large atom numbers and far below the critical temperature, it can also be applied to derive a simpler two mode Hamilton function.

Following the derivation in [24] and starting with the Gross-Pitaevskii equation (Eq. 2.5) the two mode Gross-Pitaevskii Hamilton function is of the form

$$\begin{aligned}
 H_{\text{GP-2M}} &= \frac{E_{\text{c-GP}}}{2} n^2 - E_{\text{j-GP}} \sqrt{1 - \frac{4n^2}{N^2}} \cos(\phi) \\
 &+ \frac{\delta E_{\text{GP}}}{2} \left(1 - \frac{4n^2}{N^2}\right) \cos(2\phi), \tag{2.87}
 \end{aligned}$$

where

$$\begin{aligned}
 n &= \frac{N_r - N_l}{2}, \\
 \phi &= \phi_l - \phi_r. \tag{2.88}
 \end{aligned}$$

$n$  is the population imbalance and  $\phi$  is the relative phase. The coupling constants are given by

$$E_{\text{c-GP}} = \frac{2}{N} \frac{10\gamma_{g,e} - \gamma_{g,g} - \gamma_{e,e}}{4}, \tag{2.89}$$

$$E_{\text{j-GP}} = \frac{N}{2} \left( \mu_e - \mu_g - \frac{\gamma_{e,e} - \gamma_{g,g}}{2} \right), \tag{2.90}$$

$$\delta E_{\text{GP}} = \frac{N}{2} \frac{\gamma_{g,g} + \gamma_{e,e} - 2\kappa_{g,e}}{4}, \tag{2.91}$$

$$\text{with } \gamma_{i,j} = gN \int d\mathbf{r} |\Phi_i(\mathbf{r})|^2 |\Phi_j(\mathbf{r})|^2, \quad (\text{with } i, j = g, e). \tag{2.92}$$

For large  $N$  and small  $\delta E$  the Bose-Hubbard and the Gross-Pitaevskii constants are approximately equal. In this limit, the Hamilton function can be written in analogy to Eq. 2.47 as

$$H_{\text{GP-2M}} = \frac{E_c}{2} n^2 - E_j \sqrt{1 - \frac{4n^2}{N^2}} \cos \phi, \tag{2.93}$$

where  $n^2 \Leftrightarrow \langle n \rangle^2$  and  $\sqrt{1 - \frac{4n^2}{N^2}} \cos \phi \Leftrightarrow \langle \hat{\alpha}_+ \rangle$ . The expectation value of the tunneling operator, as discussed before, is the product of the expectation values of the cosine operator and the visibility operator, which is reflected in the latter correspondence.

This formalism is very useful in order to gain intuitive insight into the properties of the BJJ, as Eq. 2.93 does not only describe the BJJ in the mean field model but also a single particle in a sinusoidal potential, where the height of the potential decreases with the momentum of the particle. In this picture the population imbalance corresponds to the momentum of the particle, the relative phase to the position coordinate, the mass is  $E_c^{-1}$  and the potential height is  $E_j \sqrt{1 - \frac{4n^2}{N^2}}$ . A sketch of this model is shown in Fig. 2.8 (a), where the ground state wave function of the particle in the periodic potential is plotted. However, for small  $n$  and  $\phi$  the Hamilton function can be simplified to the Hamilton function describing a single particle in a parabolic potential

$$H_{\text{simplified}} = \left( E_c + \frac{4E_j}{N^2} \right) \frac{n^2}{2} + \frac{E_j}{2} \phi^2, \tag{2.94}$$

where the potential becomes independent of the momentum.

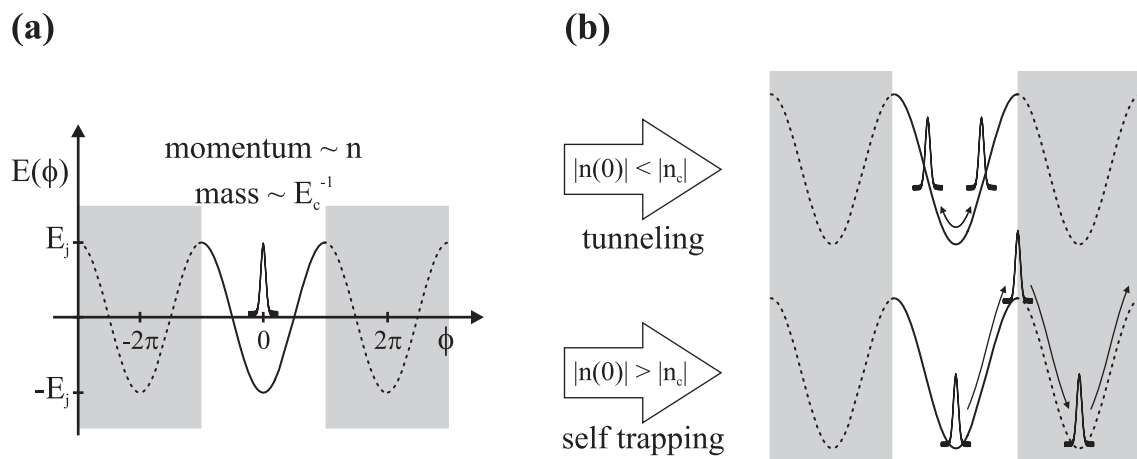


Figure 2.8: Mechanical analogue to the bosonic Josephson junction. The Hamilton function Eq. 2.94 does not only describe two coupled matter waves in the Josephson regime, but also a single particle in a sinusoidal potential where the population imbalance is connected to the momentum and the relative phase to the position of the particle. Here the mass of the particle is  $1/E_c$  and the periodic potential has a height of  $2E_j$ . (a) shows a sketch of the ground state wave function of the single particle in the potential, which is extended beyond the definition of  $\phi \in [-\pi, \pi]$  (dashed line in the gray shaded area). The dynamical response of the BJJ can be visualized with this analogue. In (b), the two expected dynamical regimes are shown. The upper graph corresponds to an initial kick, which is smaller than a critical value, leading to oscillations of the particle around its equilibrium position. If the kick is large enough such that the particle can reach the potential maxima as shown in the lower graph, the particle will continue moving through the periodic potential.

## 2.4.2 Properties in steady state

The quantization of the simplified classical Hamilton function (Eq. 2.94) allows for an intuitive understanding of the steady state properties of the BJJ. It reveals that the position and the momentum are not perfectly defined but show a quantum mechanical uncertainty of (see e.g. [32])

$$\Delta n^2 = \frac{1}{2} \sqrt{\frac{E_j}{E_c + 4E_j/N^2}} \quad , \quad \Delta \phi^2 = \frac{1}{2} \sqrt{\frac{E_c + 4E_j/N^2}{E_j}} \quad . \quad (2.95)$$

Furthermore, the product of the fluctuations leads to an uncertainty relation of the form

$$\Delta n^2 \times \Delta \phi^2 = (\langle \hat{n}^2 \rangle - \langle \hat{n} \rangle^2) \times (\langle \hat{\phi}^2 \rangle - \langle \hat{\phi} \rangle^2) \geq 1/4, \quad (2.96)$$

where the equality is valid for the ground state. The comparison of this uncertainty relation with the exact calculation using the Bose-Hubbard model is shown in Fig. 2.9. The solid lines were calculated with  $N=100$  and the dashed line is the prediction of the GP two mode model. (a) shows the comparison of the atom number fluctuations, (b) the phase fluctuations and (c) the uncertainty relation. In the Rabi and the Josephson regime the agreement is excellent as in this regimes the mean field description is an accurate approximation, however in the Fock regime the product vanishes, as the fluctuation of the atom numbers becomes arbitrarily small but the fluctuation of the phase is bound.

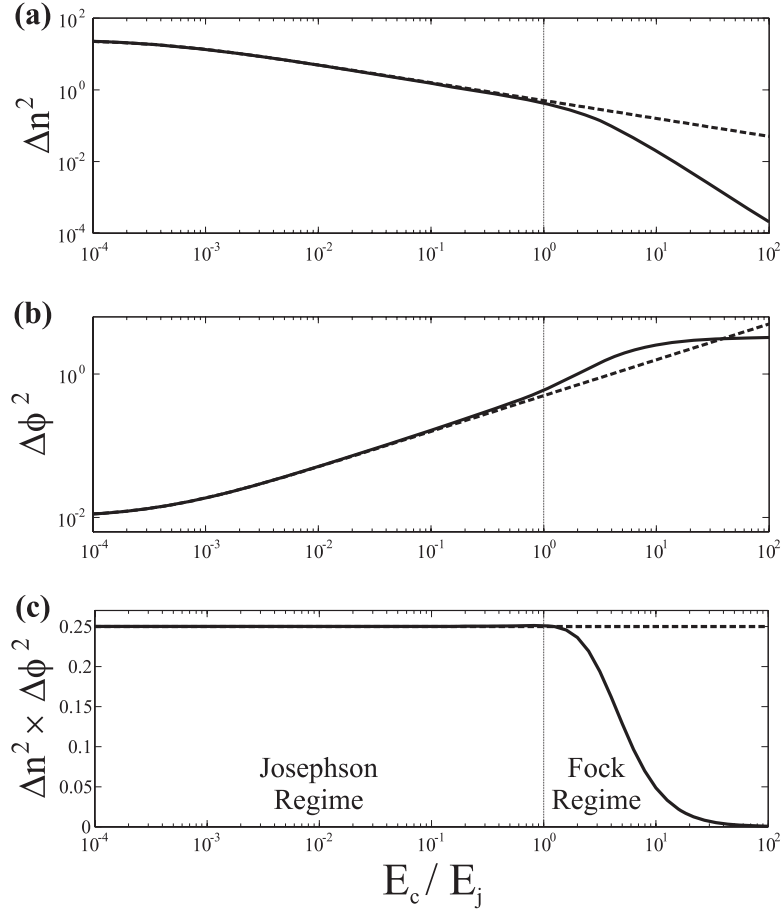


Figure 2.9: Uncertainty relation for the conjugate variables  $n$  and  $\phi$ . The solid lines in (a) and (b) show the fluctuations of the atom numbers and the relative phase respectively and compare them with the classical predictions (dashed lines). In (c) the product (solid line)  $\Delta n^2 \times \Delta \phi^2$  demonstrates the uncertainty principle, which connects the two variables in the Rabi and the Josephson regime. The expected value is  $1/4$  (dashed line). In the Fock regime, the product vanishes, as the fluctuation of the atom number difference tends to zero but the fluctuation of the phase is bound (below  $\pi$ ).

### 2.4.3 Properties in steady state at finite temperature

The finite temperature properties in steady state can be deduced from the mechanical analogue as well. The amount of thermally induced fluctuations of the two dynamical variables might be estimated by using the simplified classical Hamilton function (Eq. 2.94), neglecting the quantum mechanical uncertainties and populating the potential according to the Boltzmann distribution, leading to the fluctuations

$$\Delta n_{\text{th}}^2 = \langle n^2 \rangle_{\text{th}} - \langle n \rangle_{\text{th}}^2 = \frac{k_B T}{E_c + \frac{4E_j}{N^2}} \quad , \quad \Delta \phi_{\text{th}}^2 = \langle \phi^2 \rangle_{\text{th}} - \langle \phi \rangle_{\text{th}}^2 = \frac{k_B T}{E_j} . \quad (2.97)$$

The product of the thermally induced fluctuations gives also rise to an uncertainty relation of the form

$$\Delta n_{\text{th}}^2 \times \Delta \phi_{\text{th}}^2 \geq \frac{(k_B T)^2}{E_j \left( E_c + \frac{4E_j}{N^2} \right)} . \quad (2.98)$$

For very high temperatures, the product deviates from the uncertainty relation due to two reasons. On the one hand, the assumptions for the derivation of the simplified Hamilton function are not fulfilled, i.e.  $n$  and  $\phi$  are not small, and on the other hand the fluctuations of both variables are bound as  $n \in [-N/2, N/2]$  and  $\phi \in [-\pi, \pi]$ . However, qualitatively, the uncertainty relation reveals the general influence of temperature, leading to an increase of the fluctuations of both dynamical variables with temperature.

#### 2.4.4 Dynamical properties

The general dynamical behavior of the BJJ can also be derived from the single particle picture. If the particle is slightly moved away from its ground state position (i.e. a small phase is imprinted) or the particle has a small initial momentum (i.e. a small initial population imbalance), the particle will perform harmonic oscillations around the minimum of the potential at the characteristic plasma frequency Eq. 2.53, as sketched in the upper graph in Fig. 2.8 (b). The oscillations of the particle correspond to oscillation of the population imbalance and the relative phase around a zero mean value. This dynamical regime is referred to as the plasma oscillation regime.

For larger momenta, the assumption for Eq. 2.94 are not fulfilled and Eq. 2.93 should be considered instead. If the initial kick is large enough such that the particle can reach the top of the potential, as shown in the lower graph in Fig. 2.8 (b), the particle will continue moving through the lattice. In this case, the position coordinate will increase in time and the momentum will always point into the same direction leading to a non zero mean value. This corresponds to the winding up of the relative phase and a non vanishing mean population imbalance. This regime is called the self trapping regime.

The condition for self trapping is, that the initial energy of the particle is just enough to reach the top of the potential (i.e.  $\phi = \pi$  at  $n = 0$ ), which is the case if  $H(n_c, \phi = 0) > H(n = 0, \phi = \pi)$ . Thus, the critical initial imbalance  $n_c$  for a zero initial phase difference is defined as

$$\frac{E_c}{2} n_c^2 - E_j \sqrt{1 - \frac{4n_c^2}{N^2}} = E_j \quad \Rightarrow \quad |n_c| = 2 \sqrt{\frac{E_j}{E_c} \left( 1 - \frac{4E_j}{N^2 E_c} \right)}. \quad (2.99)$$

Also a third dynamical regime exists due to the dependence of the potential height on the momentum leading in certain cases to stable oscillations around the top of the potential, but as this regime is not obvious from the single particle picture, I refer to [28] for more details.

## 2.5 Summary of the theoretical background

A Bose-Einstein condensate confined in a double well potential behaves similarly to a Josephson junction realized with superconductors. This bosonic Josephson junction is accurately described by the Bose-Hubbard model for low energetic excitations and low temperatures, where the number of allowed mean field orbitals is reduced to two. The particles in these two modes are coupled to each other due to the local atom-atom interactions. A convenient choice for the basis are the Fock states with a well defined number of particles in the left and the right well. The relevant quantities for a characterization of the BJJ are apart from the expectation value of the atom number difference, the atom number fluctuations and the coherence. By investigating the behavior of the last two quantities, three dynamical regimes can be distinguished: the Rabi regime, where the coherence is high but also the atom number fluctuations are large, the Josephson regime, where the coherence is high and the atom

number fluctuations are small, and the Fock regime, where both quantities are small. In the Josephson regime the creation and annihilation operators can be exchanged by complex numbers allowing for the description of the system in terms of a mean field model. The mean field model shows, that only two variables are needed to describe the state of the BJJ, namely the atom number difference and the relative phase. The properties of the BJJ can be directly derived from a mechanical analogue, which is a single particle in a momentum dependent periodic potential.

The atom number difference in the Bose-Hubbard and the mean field model are directly related, however, it is difficult to define a quantity in the Bose-Hubbard picture, which corresponds to the relative phase from the mean field description. For this, a new set of basis states, the phase states, is introduced resulting from a Fourier-transformation of the Fock states. The distribution of the relative phases is then obtained by a projection of the state of the BJJ onto these phase states. With the knowledge of the phase distribution, the relevant expectation values are easily calculated.

### 3 Experimental realization of a single bosonic Josephson junction

A bosonic Josephson junction can be realized experimentally, by implementing a double well potential for a Bose-Einstein condensate. In our experiments, the double well potential results from the superposition of a 3-D harmonic confinement and a periodic potential with large periodicity. The harmonic trap is responsible for an overall confinement of the particles and the periodic potential, if adjusted properly, realizes a barrier in the center. The generation and the preparation of the BEC are performed in two vacuum chambers employing optical and magnetic forces.

The schematics of the components used to generate the double well potential are shown in Fig. 3.1 (a). The resulting effective potential, which is a Gaussian trapping potential modulated by the periodic potential is plotted in (b). A zoom into the central region, as shown in (c), reveals that the resulting potential is a double well if the chemical potential of the particles in the trap is lower than the minimal energy of the next neighboring wells.

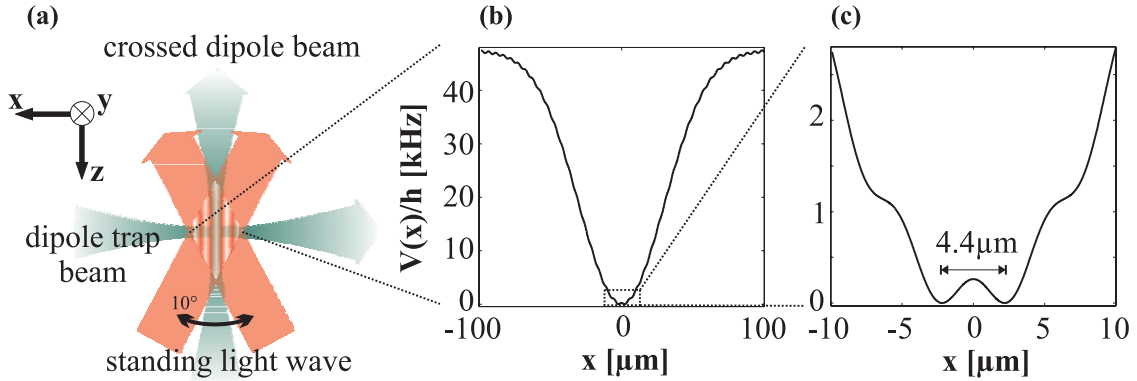


Figure 3.1: Experimental setup and realization of the double well potential by the superposition of a harmonic trap and an optical lattice with large periodicity. (a) is a cut through the center of the laser beams generating the optical potentials. Two orthogonal dipole trap beams at 1064nm (gray) create a 3-D harmonic confinement and two laser beams at 830nm crossing under an angle of about  $10^\circ$  generate the optical lattice (red) with a periodicity of  $\lambda \approx 5 \mu\text{m}$ . (b) shows the effective potential resulting from the superposition of the dipole trap and the optical lattice on the scale of the Gaussian dipole trap beam. (c) is a zoom onto the potential in the center. It reveals that the potential can effectively be described as a double well potential with a separation of the two wells of about  $4.4 \mu\text{m}$ , if the height of the periodic potential is chosen properly.

### 3.1 Experimental apparatus

The experimental apparatus can be divided into two major components, the laser system and the vacuum system. The laser system provides laser light at different frequencies for cooling, trapping and manipulating the atoms and the vacuum system is needed in order to isolate the cooled atomic cloud from the hot environment. Two vacuum chambers are present, the high vacuum chamber (HVC) in which a cold atomic beam is prepared and the ultra high vacuum chamber (UHVC) where the cold atoms are collected, cooled further and where the experiments are performed. A schematic overview of the experimental setup is depicted in Fig. 3.2. The upper part shows the laser setup and the 'darkened area' the vacuum system. The vacuum system is covered in order to prevent scattered light to heat up the atoms.

The schematics of the vacuum setup is shown in Fig. 3.3, where the chamber on the left hand side (funnel) corresponds to the HVC and the chamber on the right hand side to the UHVC (MOT and BEC chamber). In the HVC Rubidium atoms are released from dispensers and a slow atomic beam is generated by a funnel. The funnel is a magneto-optical trap (MOT) [54] with a 2-D transverse confinement and additional cooling in the third direction. The longitudinal cooling is adjusted such that the particles are not trapped but have still a low velocity component in the direction of the UHVC. With this, the atoms are directed through a differential pumping stage and lead into the UHVC, where a 3-D MOT is used to capture them. From the 3-D MOT, the particles are transferred into a time-orbiting-potential (TOP) trap, where they are cooled further via evaporative cooling by reducing the circle of death of the TOP trap. Before Bose-Einstein condensation is reached, the atoms are transferred into the optical dipole trap, where the temperature of the atoms is lowered a last time by evaporative cooling. The evaporation is done by lowering the laser intensities and reducing the trap depth in order to allow hot atoms to leave the trap. After the lowest possible temperatures are reached at the right atom numbers, the cooling is stopped by increasing the light intensity again and the periodic potential is turned on slowly in order to load the atoms adiabatically into the double well potential. For more details on the experimental generation of Bose-Einstein condensates and more detailed discussions on the experimental apparatus I refer to [82, 83, 84, 85].

#### 3.1.1 Laser systems

Four different laser systems are used in our experiments to provide light for manipulating the atoms:

- A Titanium-Sapphire Laser (Ti:Sa I, Coherent - Monolithic-Block-Resonator 110) is pumped by a frequency-doubled Nd:YVO<sub>4</sub> Laser (Coherent, Verdi V10) with 10W optical output power. The Ti:Sa I has a typical output power of 1.4W. It is locked to the ( $F = 2 \rightarrow F' = (3, 1)$ ) crossover transition of the D<sub>2</sub> line of Rubidium-87. The beam is split into three parts for the MOT, for the funnel, and for imaging. Every beam is passed through individual acousto-optical modulators in double-pass configuration in order to shift the frequencies by about 210MHz and address the ( $F = 2 \rightarrow F' = 3$ ) transition (see Appendix D).
- An external cavity diode laser (Repumper, ECDL) in Littrow configuration with a typical output power of 30mW is locked to the ( $F = 1 \rightarrow F' = 2$ ) transition of the D<sub>1</sub>-line. It is used to repump atoms back into the MOT-cycle, which have decayed into the  $5S_{1/2}$  state.

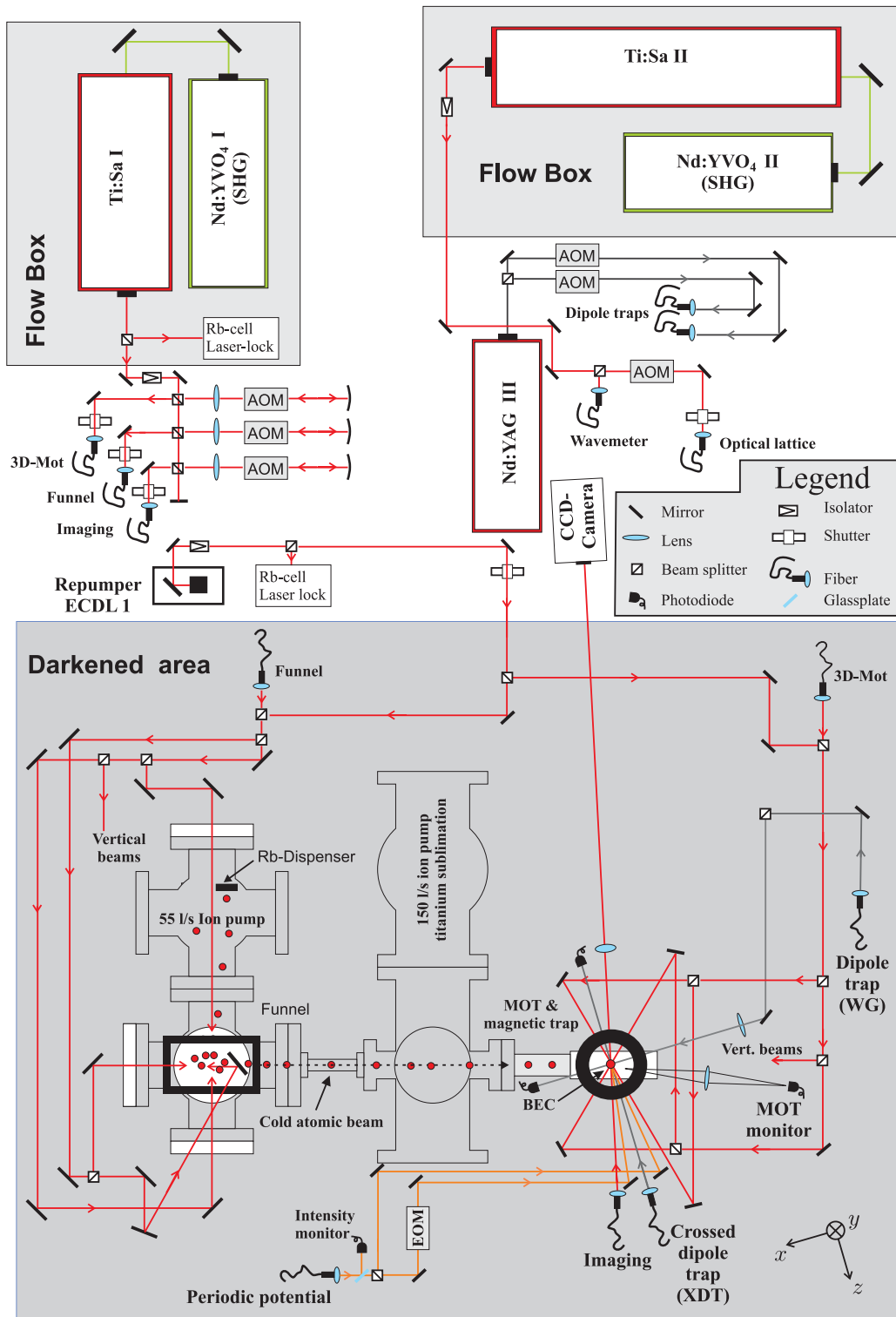


Figure 3.2: Schematics of the experimental setup. The upper part shows the laser system, where laser beams are prepared at the necessary frequencies and the lower part (darkened area) to the vacuum setup containing the experimental chambers with the relevant optical components.

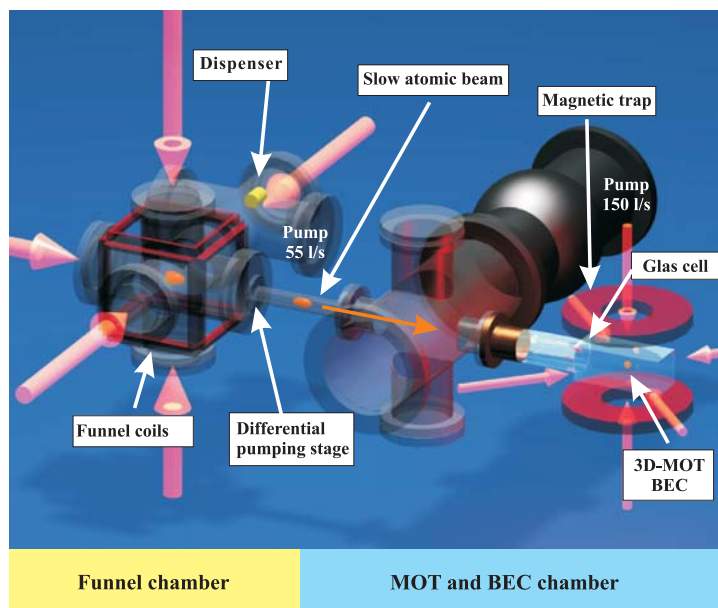


Figure 3.3: Vacuum setup. The pressure in the first chamber is about  $10^{-9}$ mbar (HVC), here the  $^{87}\text{Rb}$  atoms are precooled via a funnel. A differential pumping stage connects the HVC with the UHVC, which is at a pressure of  $\approx 10^{-11}$ mbar. Here, the atoms are collected in a MOT, cooled further in a TOP trap and transferred into the crossed dipole trap, where Bose-Einstein condensation is reached.

- A diode laser pumped Nd:YAG Laser (Spectra-Physics, T40-X30-106QW) with a wavelength of 1064nm and a maximum output power of 8W provides the light for the two beams of the crossed optical dipole trap. The maximal power in the TEM-00 mode, which can be coupled into the two single mode fibres, is about 3W.
- The light for the optical lattice is provided by a second Titanium-Sapphire Laser (Ti:Sa II, Coherent - 899), which is pumped by a Coherent Verdi V10. It has a typical output power of 1.2W and is operated at a wavelength of between 810 and 830nm.

### 3.1.2 Laser induced potential for ultracold neutral atoms

A possibility to generate external potentials for ultra cold atoms is the application of coherent light fields. The electric field of a laser beam interacts with the atom by inducing an electric dipole moment which again interacts with the electric field [86]. The depth of the resulting potential depends directly on the detuning  $\delta = \omega_l - \omega_0$ , which is the frequency difference of the laser  $\omega_l$  and the frequency of the dominant electronic transition  $\omega_0$ . If not only one but multiple electronic transitions are of relevance, the detuning of each transition has to be taken into account multiplied by the corresponding Clebsch-Gordon coefficients.

The effective potential induced by the laser field can be calculated by taking also spontaneous scattering of photons into account and using the steady state solutions of the optical Bloch equations [87]. The resulting dipole potential is given by

$$V_{\text{dipole}}(\mathbf{r}) = \frac{\hbar\delta}{2} \ln \left( 1 + \frac{I(\mathbf{r})/I_{\text{sat}}}{1 + 4\frac{\delta^2}{\Gamma^2}} \right) \quad \text{with} \quad I_{\text{sat}} = \frac{\hbar\Gamma\omega_0^3}{12\pi c^2}, \quad (3.1)$$

where  $I(\mathbf{r})$  is the local intensity of the laser field,  $\Gamma$  is the natural line width of the transition,

and  $c$  is the speed of light. In the limit  $I(\mathbf{r})/I_{\text{sat}} \ll 1 + 4\delta^2/\Gamma^2$ , the dipole potential can be written as

$$V_{\text{dipole}}(\mathbf{r}) \approx \frac{\hbar\delta}{2} \frac{I(\mathbf{r})/I_{\text{sat}}}{1 + 4\frac{\delta^2}{\Gamma^2}}. \quad (3.2)$$

If further  $\delta^2 \gg \Gamma^2$ , the potential can be simplified to

$$V_{\text{dipole}}(\mathbf{r}) \approx \frac{\hbar\Gamma^2 I(\mathbf{r})}{8\delta I_{\text{sat}}}. \quad (3.3)$$

In addition to the dipole force, a second force is acting. It results from the absorption and spontaneous emission of photons and is called the radiation pressure force. As the spontaneous emission is an incoherent process the emission of a photon leads to the removal of the atom from the BEC and thus to a loss or even a heating mechanism. Hence, in order to utilize optical potentials for trapping and manipulating Bose-Einstein condensates the spontaneous scattering rate  $\Gamma_{\text{sp}}$  should be as small as possible

$$\Gamma_{\text{sp}} = \frac{\Gamma/2}{1 + \frac{I_{\text{sat}}}{I} (1 + 4\delta^2/\Gamma^2)} \approx \frac{\Gamma^3 I}{8\delta^2 I_{\text{sat}}}, \quad (3.4)$$

where the last term corresponds to the same conditions as described for Eq. 3.3. For the applicability of optical dipole potentials, large detunings are favorable as the potential is inversely proportional to the detuning  $V_{\text{dipole}} \propto \delta^{-1}$  but the spontaneous scattering rate to the detuning squared  $\Gamma_{\text{sp}} \propto \delta^{-2}$  and thus decreases faster with increasing  $\delta$ .

For negative detunings (red-detuned light) the dipole potential is attractive and can be used to trap atoms in the intensity maxima. For positive detunings (blue-detuned light) the potential is repulsive and the atoms are pushed out of the regions with high intensity into the local minima. With properly tailored intensity profiles optically induced potentials of almost arbitrary shapes can be realized. In experiments, usually two types of optical potentials are used, harmonic and sinusoidal.

### 3.1.3 Ultra-stable harmonic trapping potential

The 3-D harmonic trap in our experiments is generated by two crossed far red-detuned Gaussian Nd:YAG-laser beams at  $\lambda_{\text{Nd:YAG}} = 1064\text{nm}$ . The beams are passed through acousto-optical modulators (AOM) driven at radio frequencies of about 80MHz with a frequency difference of approximately 1MHz between the two beams in order to avoid interference. The intensity profile resulting from a single Gaussian TEM-00 laser beam is given by

$$I(\mathbf{r}) = \frac{I_0}{1 + (z/z_0)^2} \exp\left(-2\frac{x^2 + y^2}{\sigma^2(1 + (z/z_0)^2)}\right) \quad \text{with} \quad z_0 = \frac{\pi\sigma^2}{\lambda_l}, \quad (3.5)$$

where  $I_0$  is the peak intensity,  $\sigma$  is the  $1/e^2$ -waist of the transverse Gaussian profile and  $\lambda_l$  is the wavelength of the laser light. For large detunings  $\delta^2/\Gamma^2 \gg \max(1, I/I_{\text{sat}})$  the effective light induced potential is proportional to the intensity distribution and thus can be approximated in the center ( $|x| \ll \sigma_x$ ,  $|y| \ll \sigma_y$  and  $|z| \ll z_0$ ) by a 3-D harmonic potential

$$V_{\text{harm}}(\mathbf{r}) = V_0 \cdot \left(1 - \frac{2x^2}{\sigma_x^2} - \frac{2y^2}{\sigma_y^2} - \frac{z^2}{z_0^2}\right) \quad \text{with} \quad V_0 = \frac{\hbar\Gamma^2 I_0}{8\delta I_{\text{sat}}}. \quad (3.6)$$



son junction, as the tunneling times and coupling constants depend strongly on the exact shape of the potential. Therefore, both beams are transferred to the experiment via optical fibers and the output couplers are located in a distance of about 20cm from the atoms in order to minimize the drift and the fluctuations of the trap position and provide high passive stability. Furthermore, the output coupler of the XDT is fixed on a piezo actuated mount, which allows for changing the output coupling angle and thus the position of the trap over several micrometers.

The intensity of both dipole trap beams is actively stabilized. For this, the intensity of the reflected light from the experimental chamber is monitored and coupled back onto the AOMs via PI-loops. The stability achieved is better  $10^{-4}$  for the frequency range below 1kHz.

### 3.1.4 Actively stabilized periodic potential

The periodic potential is realized by the interference of two Ti:Sa-laser beams at  $\lambda_{\text{Ti:Sa}} = 810$  to 830nm, crossed under an angle of about  $10^\circ$ . The waist of the two beams is  $500\mu\text{m}$  and the power of each is up to 100mW. The time averaged intensities and the wave vectors of the two beam are  $I_1(\mathbf{r})$ ,  $I_2(\mathbf{r})$  and  $\mathbf{k}_1$ ,  $\mathbf{k}_2$  respectively. The intensity distribution of these two large interfering Gaussian beams (transverse size much larger than the wavelength of the resulting periodic potential) is approximated in the center by the intensity distribution of two interfering plane waves. For simplicity, we consider light fields at the same frequency with  $\omega_1 = \omega_2 = \omega_l$  and  $|\mathbf{k}_1| = |\mathbf{k}_2| = |\mathbf{k}|$ . The intensity profile of the two interfering plane waves is given by

$$\begin{aligned} I(\mathbf{r}, t) &= 2I_1(\mathbf{r}) \cos^2(\omega_l t - \mathbf{k}_1 \cdot \mathbf{r} + \phi_1) + 2I_2(\mathbf{r}) \cos^2(\omega_l t - \mathbf{k}_2 \cdot \mathbf{r} + \phi_2) \\ &+ 2\sqrt{I_1(\mathbf{r})I_2(\mathbf{r})} \cos\left(2\omega_l t - (\mathbf{k}_1 + \mathbf{k}_2) \cdot \mathbf{r} + \phi_1 + \phi_2\right) \\ &+ 2\sqrt{I_1(\mathbf{r})I_2(\mathbf{r})} \cos\left((\mathbf{k}_2 - \mathbf{k}_1) \cdot \mathbf{r} + \phi_1 - \phi_2\right), \end{aligned} \quad (3.8)$$

where  $\phi_1$  and  $\phi_2$  are the phases of the two plane waves at  $t = 0$ ,  $\mathbf{r} = 0$ . This intensity profile corresponds to a plane wave at the optical frequency in the direction  $(\mathbf{k}_1 + \mathbf{k}_2)$  and a perpendicular standing light wave. Time averaging of the intensity profile leads to

$$I_{\text{eff}}(\mathbf{r}) = I_1(\mathbf{r}) + I_2(\mathbf{r}) + 2\sqrt{I_1(\mathbf{r})I_2(\mathbf{r})} \cos\left((\mathbf{k}_2 - \mathbf{k}_1) \cdot \mathbf{r} + \phi_1 - \phi_2\right). \quad (3.9)$$

The resulting periodicity of the standing light wave is

$$\lambda_{\text{sw}} = \frac{2\pi}{|\mathbf{k}_2 - \mathbf{k}_1|} = \frac{2\pi}{2|\mathbf{k}| \sin(\theta/2)} = \frac{\lambda_l}{2 \sin(\theta/2)}, \quad (3.10)$$

where  $\theta$  is the angle between the two wave vectors given by  $\cos \theta = \mathbf{k}_1 \cdot \mathbf{k}_2 / |\mathbf{k}|^2$ . For counter-propagating beams ( $\theta = \pi$ ), the periodicity of the standing wave is  $\lambda_l/2$ , which is the smallest periodicity achievable with laser light at  $\lambda_l$ . By decreasing the angle, the periodicity increases until for  $\theta = 0$  it becomes infinite.

The time averaged potential for large detunings ( $\delta^2/\Gamma^2 \gg \max(1, I/I_{\text{sat}})$ ) is given by

$$V_{\text{sw}}(\mathbf{r}) = V_1(\mathbf{r}) + V_2(\mathbf{r}) + 2\sqrt{V_1(\mathbf{r})V_2(\mathbf{r})} \cos\left((\mathbf{k}_2 - \mathbf{k}_1) \cdot \mathbf{r} + \phi_1 - \phi_2\right), \quad (3.11)$$

where  $V_{1,2}$  corresponds to the potentials independently generated by the two light fields  $V_i(\mathbf{r}) = \hbar\Gamma^2 I_i(\mathbf{r})/8\delta I_{\text{sat}}$ .

The periodic potential realized in the experiment with laser light at a wavelength of 830nm and an angle of  $10^\circ$  between the beams has the form

$$V_{\text{sw}}(\mathbf{r}) = V_0 \left( 1 + \cos(d_{\text{sw}} \cdot x + \phi_{\text{pos}}) \right), \quad (3.12)$$

with  $d_{\text{sw}} \approx 5\mu\text{m}$ .  $\phi_{\text{pos}}$  is the phase difference of the two laser fields and corresponds to the position of the interference maxima. The assumption of plane waves is satisfied as the transverse size of the beams is much larger than the periodicity of the resulting potential and thus the intensity of the two beams does not change on the scale of the double well. At a power of about 50mW per beam the periodic potential has a height of  $V_0/h \approx 6\text{kHz}$ .

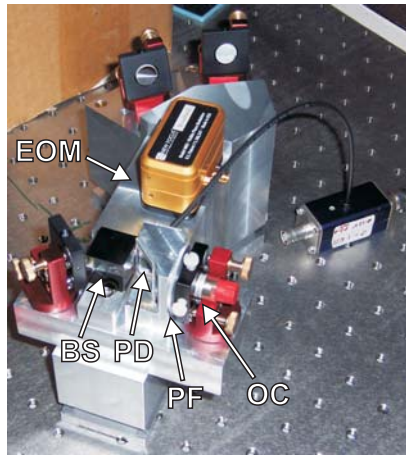


Figure 3.5: Mount of the optics for the standing light wave beams. The laser light enters the setup through an output coupler (OC) and is transmitted through a polarization filter (PF). Then the beam is passed through an antireflection coated glass plate, where a small amount of light is coupled out and brought to a photo diode (PD) to monitor the intensity. A non-polarizing beam splitter is used to divide the beam into two parts at the same intensity. One of the beams is then passed through an electro-optical modulator (EOM) which, if a voltage is applied, changes the optical path of the beam. This component is used for the active stabilization of the resulting interference patterns. The last two mirrors reflect the light into the experimental chamber, where the two beams cross under an angle of about  $10^\circ$ .

The setup for generating the standing light wave is shown in Fig. 3.5. To achieve high passive stability all optical components are mounted on a single aluminium block, which is located only about 30cm away from the experimental chamber. The light is transferred to the setup, after being passed through an AOM, via a polarization maintaining single mode optical fiber and enters the setup through the output coupled (OC). Then, the light is directly passed through a polarization filter (PF) and an antireflection coated glass plate, where a small amount of the light is removed from the beam and directed onto a photo diode (PD). The signal of the photo diode is used to stabilize the intensity of the standing light wave beam by means of a PI-loop that is connected to the AOM, reaching a stability of better than  $10^{-4}$  for the frequency range below 1kHz. The next component in the beam path is a non-polarizing beam splitter (BS) which divides the beam into two parts. Before entering the experimental chamber, one beam is passed through an electro-optical modulator (EOM). The EOM consists of a non-linear crystal, which changes its index of refraction if a voltage is applied (Pockels effect). With this, the optical path of one beam can be modified leading to a change of its phase ( $\phi_{\text{pos}}$ ) and thus to a change of the position of the interference peaks.

The EOM is used for the active stabilization of the position of the interference patterns. For this a small amount of light is removed from the beams by a second anti-reflection coated glass plate, as shown in Fig. 3.6 (a), and brought to interfere on a precision air slit with a width of  $2\mu\text{m}$  and a length of 3mm. The slit is adjusted to be parallel to the interference patterns. As the slit is thinner than the periodicity of the patterns, the transmitted light intensity is proportional to the local phase of the standing wave and is measured by means of a photo diode behind the slit. The stabilization of the phase is done by using a lock-in amplifier driven at 12kHz and coupling the signal via a PI-loop back to the EOM.

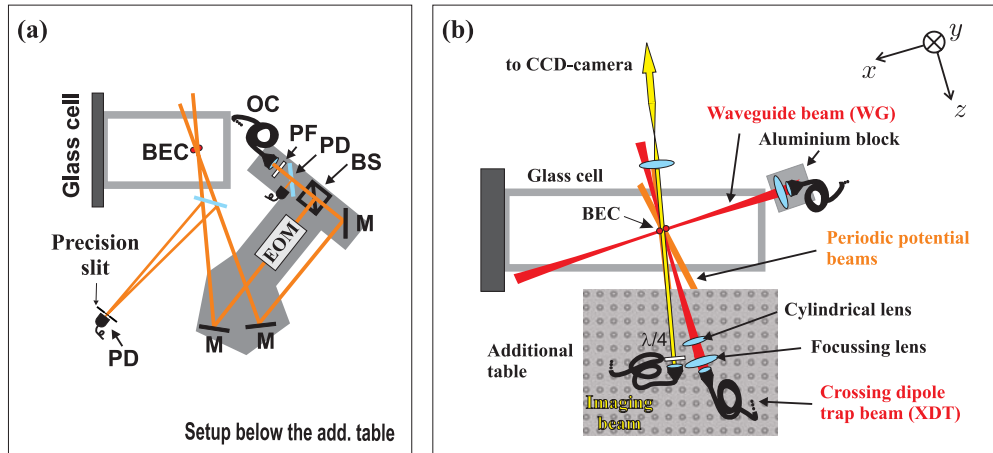


Figure 3.6: Schematics of the setup for stabilizing the standing light wave. (a) shows the setup used for generating the standing light wave, where the same components are listed as in Fig. 3.5. (OC): output coupler, (PF): polarization filter, (PD): photo diode, (BS): beam splitter, (EOM): electro-optical modulator and (M): mirrors. Additionally, the components for monitoring the position of the interference patterns are shown. Some light is coupled out from the two beams by an antireflection coated glass plate and directed onto a precision air slit with a width of  $2\mu\text{m}$ . The resulting interference patterns are monitored with a photo diode, which measures the transmitted light behind the slit. (b) shows the setup for generating the 3-D harmonic trap and the imaging. Underneath the table, on which the crossed dipole trap (XDT) and the output coupler for the imaging beams are mounted, is the setup shown in (a). The setup of the standing light wave is adjusted such that it is symmetric around the (XDT).

### 3.1.5 Double well potential

The superposition of the harmonic trap realized by the far red-detuned Gaussian laser beam and the periodic potential leads to an effective double well potential in the center, if the minimum of the harmonic trap coincides with a maximum of the standing light wave. To be able to generate a symmetric double well potential the setup of the standing light wave is mounted such that the periodic potential is along the WG and symmetric around the XDT as shown in Fig. 3.6 (b). The setup of the periodic potential is located below the additional table, which as shown in this graph holds the output coupler of the XDT and the output coupler of the imaging beam. The second antireflection coated glass plate and the air-slit are mounted onto the table as well to guarantee the highest possible passive stability of the periodic potential with respect to the XDT.

However, as the position of the standing light wave is locked to the slit, but not to the harmonic trap, the symmetry of the double well has to be adjusted by changing the position

of the harmonic trap by means of the piezo actuated mount. To measure the symmetry of the double well potential, the population imbalance of the atoms is observed directly in the trap, which depends critically on the symmetry of the potential (see Sec. 4.1.1). To guarantee that the double well potential has the right symmetry, check measurements are performed after every 10-20 experiments.

The effective double well potential has the form

$$V_{\text{dw}} = \frac{1}{2}m(\omega_x^2 x^2 + \omega_y^2 y^2 + \omega_z^2 z^2) + \frac{V_0}{2} \left( 1 + \cos \frac{2\pi}{d_{\text{sw}}} x \right), \quad (3.13)$$

where  $V_0$  is the height of the periodic potential,  $d_{\text{sw}}$  is its periodicity and the harmonic trap is characterized by the three trapping frequencies  $\omega_x$ ,  $\omega_y$  and  $\omega_z$ .

The resulting potential consists in its center of two wells separated by a barrier only for sufficiently large values of  $V_0$  as shown in Fig. 3.7 (a). The height of the barrier  $V_b$ , which is the difference between the potential at the minimum and the potential in the center, is directly connected to the height of the periodic potential  $V_0$  as depicted in Fig. 3.7 (b). However, a change of  $V_0$  does not only result in a change of the barrier height but also a change of the separation of the two wells, as shown in Fig. 3.7 (c). Below a critical value of the height of the periodic potential  $V_0 < m\omega_x^2 \lambda_{\text{sw}}^2 / 2\pi^2$ , the minimum  $x_1$  is located in the center. Above this value, the distance between the center and the position of the first minimum increases with  $V_0$  and approaches  $\lambda_{\text{sw}}/2$  asymptotically, leading to a maximal separation of the two wells of  $\lambda_{\text{sw}}$ . Fig. 3.7 (d) shows the effective barrier height  $V_b$  as a function of  $V_0$ . For small values of  $V_0$ , the barrier height is zero and it increases with  $V_0$  until for large values of  $V_0$  the barrier height becomes  $V_b \approx V_0 - \frac{1}{2}m\omega_x^2 \left(\frac{\lambda_{\text{sw}}}{2}\right)^2$ .

The experimentally important quantities like the the barrier height, the local trapping frequencies in the two wells, and their separation are dominated by the properties of the periodic potential. However, the additional harmonic confinement is needed in order to shift the energy of the next neighboring wells, as the potential can only be described as a double well potential, if the minimal energies of the next neighboring wells are much larger than the chemical potential of the particles. This condition can be expressed as

$$V_{\text{dw}}(x_2, 0, 0) \approx V_{\text{dw}}(3/2\lambda_{\text{sw}}, 0, 0) = \frac{9}{8}m\omega_x^2 \lambda_{\text{sw}}^2 \gg \mu, \quad (3.14)$$

which leads to a constraint on the longitudinal trapping frequency

$$\omega_x \gg \sqrt{8\mu/9m\lambda_{\text{sw}}^2}. \quad (3.15)$$

For lower values of  $\omega_x$  not only the central two but more wells will be populated.

The energies of higher lying eigenstates of the double well potential are shown in Fig. 3.8 as a function of the height of the periodic potential. In (a), the energy of a single excited particle in the vicinity of the other particles in the ground state is calculated using the method discussed in Appendix B. The solid lines correspond to the energies of symmetric states and the dashed line to the energies of the corresponding antisymmetric states. If the barrier height becomes comparable to the energy of the states, the symmetric and antisymmetric levels become quasi-degenerate. The graph in (b) shows a similar calculation, but here all the particles are excited into the higher lying states and thus describe a collective excitation of the whole cloud. Also in this case for barrier heights comparable to the energy of the states the symmetric and antisymmetric levels become quasi-degenerate.

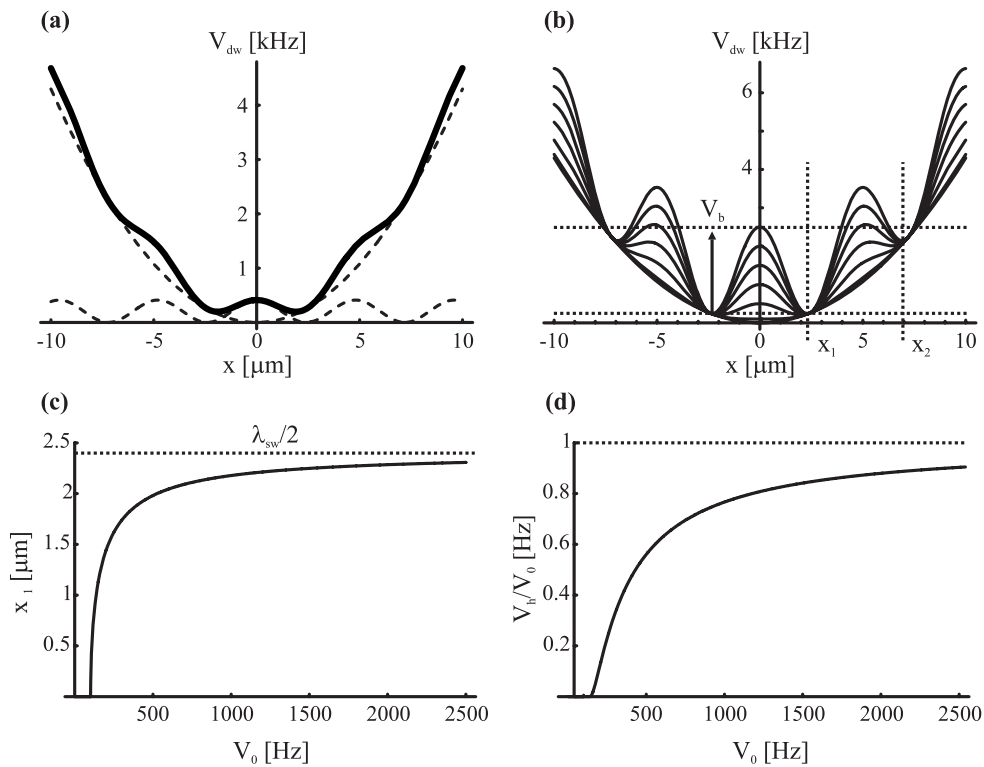


Figure 3.7: Double well potential generated by the superposition of a 3-D harmonic trapping potential and a periodic potential with large periodicity. (a) shows the combination of the harmonic trap (dashed sine) and the periodic potential (dashed parabola) to the double well potential  $V_{dw}$ . The parameters are  $\omega_x = 2\pi \times 100\text{Hz}$ ,  $V_0/h = 400\text{Hz}$  and  $\lambda_{sw} = 4.8\mu\text{m}$ . (b) shows seven double well potential for the same parameters as in (a) but different  $V_0$  ( $V_0 = 0, 100, 500, 1000, 1500, 2000, 2500\text{Hz}$ ). In (c) the position of the first minimum  $x_1$  is plotted as a function of the height of the periodic potential and (d) is the actual barrier height divided by the height of the periodic potential  $V_b/V_0$ .

### 3.1.6 Imaging the density distribution at small atom numbers

The measurement of most of the relevant quantities in our experiments is done by imaging the density distribution of the particles, either in the trap or in time of flight, and extracting the required information from the pictures. The method used in our experiments, which can efficiently be applied to image the density distribution at small atom numbers ( $N < 10^4$ ), is the destructive absorption imaging technique (for details see e.g. [88]). Absorption imaging is done by illuminating the atomic cloud with resonant light and measuring the casted shadow.

In our experiment a collimated Gaussian (TEM-00)  $\sigma^+$  polarized laser beam, which is resonant with the  $F = 2 \rightarrow F' = 3$  transition of the D2-line, with a waist of 1.9mm is used for imaging. In order to keep the atoms spin-polarized inside the optical dipole trap, a homogeneous magnetic field in the direction of the imaging beam is applied. We use high intensities ( $I > I_{\text{sat}}$ ) to saturate the atomic transition. The shadow is 10-fold magnified and detected on a CCD camera (Theta-System SiS s285M) via a commercial aspheric lens system (Zeiss Plan-Apochromat S, focal length  $f = 10\text{cm}$ ). The CCD-chip consists of  $1040 \times 1392$  pixels with a pixel size of  $6.45\mu\text{m} \times 6.45\mu\text{m}$  and has a quantum efficiency of approximately 30%. During the  $5\mu\text{s}$  of the illumination, each atom absorbs and scatters about 30 photons, leading to an average temperature increase of 0.3mK. This is far above the critical temperature and thus destroys the BEC. However, the broadening of the cloud during the exposure time is

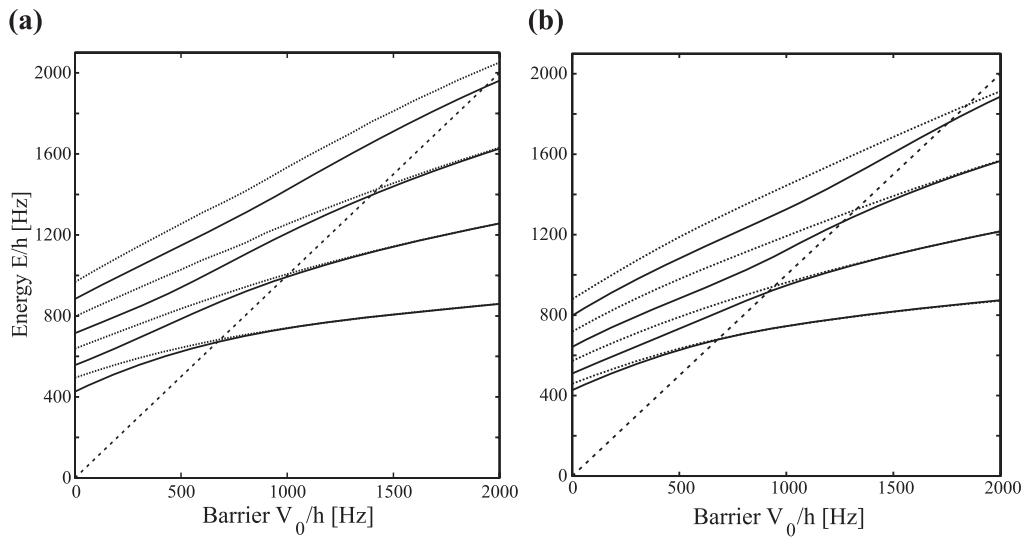


Figure 3.8: First eight eigenstates of the double well potential. (a) shows single particle excitations, where the states are calculated by minimizing the energy of a single particle in the presence of all other particles occupying the ground state. The solid lines correspond to the symmetric wave functions and the dashed lines to the energy of the antisymmetric wave functions. In (b) the energy of the eigenstates are shown, if not only one but all particles are excited into the higher lying states.

below  $1\mu\text{m}$  and therefore small compared to the optical resolution (see Sec. 3.2.2). For each measurement, we take three images. The first image  $I_{\text{pic}}$  is the picture of the imaging light in the presence of the atoms, the second  $I_{\text{ref}}$  is a picture of only the imaging light and the third is a picture of the background light  $I_{\text{back}}$  without the imaging beam. The incident and the transmitted intensity distributions are with this given by

$$I_{\text{in}} = I_{\text{ref}} - I_{\text{back}} \quad \text{and} \quad I_{\text{out}} = I_{\text{pic}} - I_{\text{back}}, \quad (3.16)$$

and can also be understood as the intensity distribution of the imaging beam before and after the particles.

The reduction of the intensity in the presence of the atoms can be calculated by assuming a homogenous density and intensity distribution locally (in a small neighborhood around  $x_0, y_0$ ) [87] and is governed by the differential equation

$$\frac{dI(\mathbf{r})}{dz} = -\sigma_{\text{scat}}(I(\mathbf{r})) \cdot n(\mathbf{r}) \cdot I(\mathbf{r}), \quad (3.17)$$

where  $n(\mathbf{r})$  is the local density distribution,  $I(\mathbf{r})$  the intensity distribution and  $\sigma_{\text{scat}}$  the scattering cross section of the atoms. The scattering cross section is proportional to the number of spontaneous emissions per particle  $\Gamma_{\text{sp}}$  (Eq. 3.4) and is given by

$$\sigma_{\text{scat}}(I(\mathbf{r})) = \frac{\Gamma \hbar \omega_l}{2I_{\text{sat}}} \left( 1 + \frac{I(\mathbf{r})}{I_{\text{sat}}} \right)^{-1}, \quad (3.18)$$

leading to a differential equation for the intensity, which cannot be solved without precise knowledge of the longitudinal density distribution. However, the experimentally accessible quantity is not the density distribution, but the density distribution integrated along the line of sight and integrated over the effective area of a pixel of the CCD-camera. This 'column'

density can be expressed as

$$N(x_0, y_0) = \int_{x_0-dx/2}^{x_0+dx/2} \int_{y_0-dy/2}^{y_0+dy/2} \int_{-\infty}^{\infty} dz dy dx n(x, y, z), \quad (3.19)$$

with the effective pixel size  $dx \times dy = A/M^2$ , which is the real pixel size  $A$  reduced by the magnification  $M \times M$ . Using Eq. 3.19 and assuming a transversally slowly varying envelope of the intensity distribution, Eq. 3.17 can be solved analytically with

$$\int_{x_0-dx/2}^{x_0+dx/2} \int_{y_0-dy/2}^{y_0+dy/2} \int_{-\infty}^{\infty} dz dy dx n(x, y, z) = -\frac{A}{M^2} \int_{I_{\text{in}}(x_0, y_0)}^{I_{\text{out}}(x_0, y_0)} dI \frac{2I_{\text{sat}}}{\Gamma \hbar \omega_l} \frac{1 + \frac{I(\mathbf{r})}{I_{\text{sat}}}}{I(\mathbf{r})}, \quad (3.20)$$

where  $I_{\text{in}}(x_0, y_0) = I(x_0, y_0, -\infty)$  and  $I_{\text{out}}(x_0, y_0) = I(x_0, y_0, \infty)$ . The resulting integrated density distribution becomes

$$N(x_0, y_0) = \frac{A}{M^2} \frac{2I_{\text{sat}}}{\Gamma \hbar \omega_l} \left( \frac{I_{\text{in}}(x_0, y_0)}{I_{\text{sat}}} - \frac{I_{\text{out}}(x_0, y_0)}{I_{\text{sat}}} + \ln \frac{I_{\text{in}}(x_0, y_0)}{I_{\text{out}}(x_0, y_0)} \right). \quad (3.21)$$

Usually, the two limiting cases are discussed, the high intensity limit ( $I_{\text{out}}(x_0, y_0) \gg I_{\text{sat}}$ )

$$N_{\text{hi}}(x_0, y_0) = \frac{A}{M^2} \frac{2}{\Gamma \hbar \omega_l} (I_{\text{in}}(x_0, y_0) - I_{\text{out}}(x_0, y_0)), \quad (3.22)$$

and the low intensity limit (Lambert-Beer law,  $I_{\text{in}}(x_0, y_0) \ll I_{\text{sat}}$ )

$$N_{\text{li}}(x_0, y_0) = \frac{A}{M^2} \frac{2I_{\text{sat}}}{\Gamma \hbar \omega_l} \ln \frac{I_{\text{in}}(x_0, y_0)}{I_{\text{out}}(x_0, y_0)}. \quad (3.23)$$

This equation is useful if the absolute value of the imaging intensity is not known accurately, as in this case, only the ratio of incoming to outgoing light is of relevance. Eq. 3.23 can be improved by using an intensity dependent scattering cross section which is assumed to be constant within the sample  $\sigma_{\text{scat}}(I(\mathbf{r})) = \sigma_{\text{scat}}(I_{\text{in}}(x_0, y_0))$  leading to the integrated density distribution

$$N_{\text{cs}}(x_0, y_0) = \frac{A}{M^2} \frac{2I_{\text{sat}}}{\Gamma \hbar \omega_l} \left( 1 + \frac{I_{\text{in}}(x_0, y_0)}{I_{\text{sat}}} \right) \ln \frac{I_{\text{in}}(x_0, y_0)}{I_{\text{out}}(x_0, y_0)}, \quad (3.24)$$

allowing for the application of this equation also for higher intensities, as long as the absorption within the cloud is small  $I_{\text{in}}(x_0, y_0) \gtrsim I_{\text{out}}(x_0, y_0)$ .

Eq. 3.24 is used to deduce the density distribution from the absorption images. In order to make sure that the error done due to this approximation is small, the total number of particles is cross-checked with an independent method (see Sec. 3.2.3).

## 3.2 Calibration of the experimental parameters

Only the precise calibration of the experimental parameters makes a quantitative comparison of the experimental data with the theoretical predictions possible. The relevant quantities for the experimental realization of the BJJ are the magnification of the imaging system, the optical resolution, the number of particles, the three trapping frequencies of the 3-D harmonic trap and the periodicity and the potential height of the standing light wave.

### 3.2.1 Magnification

The magnification of the imaging setup is measured by releasing a Bose-Einstein condensate from the harmonic trap and monitoring its position as a function of time. To release the BEC, both dipole trap beams have to be turned off at the same time, however, this is not possible as a small delay on the order of a few  $100\mu\text{s}$  is present due to the intensity locking electronics. A small delay between the times for turning off the two beams would lead to an initial kicking of the atoms. In order to minimize the kick the longitudinal confinement (XDT) is lowered to a small value and the atoms are only held by the WG, before they are released. The resulting  $y$ -position of the BEC in free fall, as shown in Fig. 3.9, is fitted by a parabola and the magnification is then deduced from its curvature. The magnification is about  $M = 10$  with an accuracy of 2%. The pixel size of the CCD-camera is  $6.45\mu\text{m} \times 6.45\mu\text{m}$  leading to an effective pixel size of about  $645\text{nm} \times 645\text{nm}$ .

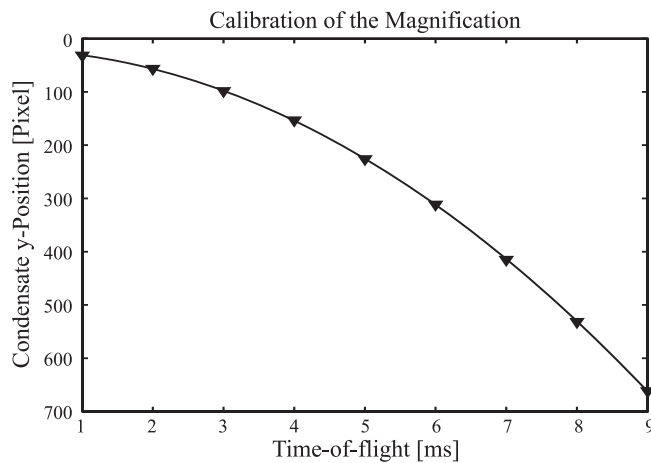


Figure 3.9: Measurement of the magnification of the imaging setup. A dilute Bose-Einstein condensate is released from a shallow harmonic trap and the  $y$ -position measured as a function of time. The magnification is deduced from the curvature of the resulting parabola and is about 1:10 with an accuracy of 2%.

### 3.2.2 Optical resolution

In the ideal situation, the optical resolution is measured by imaging a point-like object, where the resulting intensity profile corresponds to the point-spread function. However, in our experimental setup it is difficult to realize structures, which are much smaller than the optical resolution. The method applied for measuring the optical resolution of our system is shown in Fig. 3.10 (a). A BEC (consisting of a few  $10^4$  atoms) is loaded into a deep periodic potential, in which the atoms become strongly localized in the potential minima. For very deep lattices the width of the matter wave discs becomes much smaller than the optical resolution. Thus, observing the width of these discs yields the information about the point spread function. A difficulty with this method is, that due to technical reasons the symmetry axis of the periodic potential (and also the double well potential) is not parallel to the imaging axis but there is an angle of  $12.3^\circ$  in between. This leads to a smearing out of the structures due to the size of the discs.

Fig. 3.10 (b) shows the comparison of the experimentally obtained profile (solid line) with the best fit (dashed line). The fitting function is calculated by numerically solving the 3-D

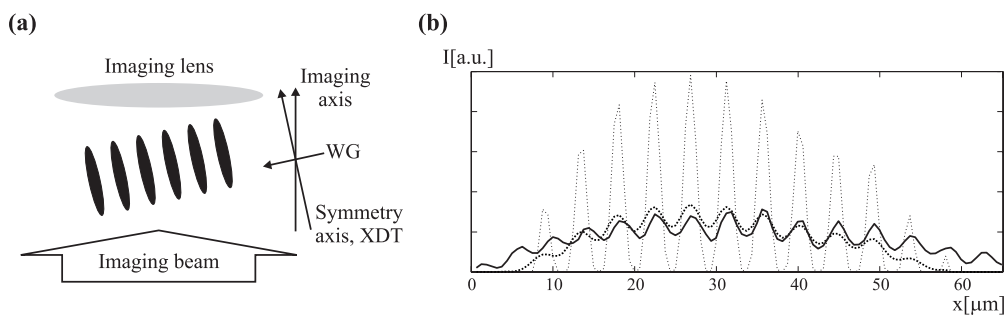


Figure 3.10: Measurement of the optical resolution of the imaging setup. (a) shows schematically the method. A BEC is loaded into a deep periodic potential, where the atoms are strongly localized in the potential minima and the density distribution is imaged along the imaging axis. Due to the angle of  $12.3^\circ$  between the imaging axis and the symmetry axis of the periodic potential, the distribution is smeared out leading to a reduction of the visibility of the resulting pattern. A measured profile (solid line) is shown in (b). The dashed line is the best fit, which results from a numerical simulation of the density distribution with a profile along the symmetry axis indicated by the dotted line. The resulting optical resolution is about  $3\mu\text{m}$  and is limited by the numerical aperture of the imaging lens.

GPE (Appendix B), rotating the density distribution to the right angle (dotted line) and then convolving the distribution with point spread functions at different width. Minimizing the standard deviation of the theoretical predictions to the experimental data leads to an optical resolution of about  $3\mu\text{m}$ . For more details on the deduction and the improvement of the optical resolution I refer to [84].

### 3.2.3 Particle numbers

The coupling constants and tunneling times in the two mode models depend strongly on the exact number of particles of the Bose-Einstein condensate fraction. The number of particles is directly given by the integral over the density distribution displayed on the absorption images. The condensate fraction can be found after an appropriate time of flight, where it separates from the thermal background. However, the number of particles deduced from the absorption images might have a systematic error resulting from uncertainty of the absolute value of the imaging intensity.

In order to cross-check the observed number of particles, we perform further measurements, where a single BEC is confined in a harmonic trapping potential with low longitudinal confinement. In this case, the density distribution is cigar-shaped, where its width along the long axis is strongly connected to the interaction energy and increases with the number of atoms in the BEC. The transverse and the longitudinal width of the cloud for different atom numbers are compared with numerical simulations as shown in Fig. 3.11. Here the optical resolution is also taken into account, which leads to a broadening of the density profiles in the images. The optical resolution is  $2.7\mu\text{m}$ (2) and the uncertainty of the resolution is indicated by the dotted lines. With this method a correction for the number of particles deduced from the absorption images is found. The accuracy achieved with this method is better than 5%.

### 3.2.4 Parameters of the harmonic trap

A straightforward method to measure the local curvature of the trapping potential is to excite collective dipolar oscillations of the atoms and deduce the oscillation frequency from the center of mass motion. However, in 2-D images only two oscillation frequencies can be

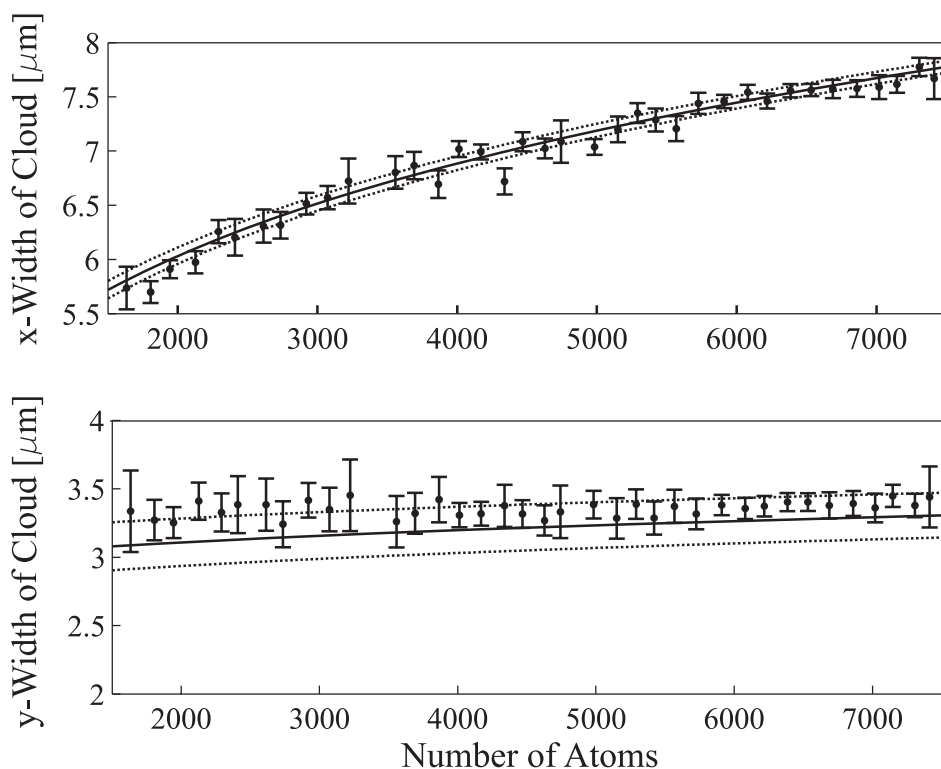


Figure 3.11: Cross-check of the number of particles. The trap parameters are  $\omega_x = 2\pi \times 35(2)\text{Hz}$ ,  $\omega_y = 2\pi \times 98(2)\text{Hz}$ , and  $\omega_z = 2\pi \times 99(2)\text{Hz}$ . The longitudinal and the transverse width of a BEC confined in a harmonic trap with low longitudinal confinement is measured for different atom numbers. The density distribution is calculated numerically, convolved with the optical resolution of  $2.7\mu\text{m}(2)$  and compared with the experimental findings (solid line). The uncertainty of the optical resolution is indicated by the dotted lines. With this method a correction for the number of particles deduced from the absorption images for a specific imaging intensity and a specific atom number range is obtained. The accuracy achieved with this method is better than 5%.

observed directly. The third frequency might be deduced from symmetry arguments for the right range of parameters, e.g. if the transverse trapping potential is cylindrically symmetric and the gravitational sag is negligible. Another possibility, which is used in our experiments, is the observation of a beating of the oscillations with the third direction. Such a beating signal can be found, if the excitation adds an angular momentum to the cloud.

Experimentally, the excitation of the BEC in the  $x$ -direction is done by moving the position of the XDT faster than the inverse trapping frequency. A center of mass motion is excited in the  $y$ -direction by turning off the transverse confinement for about 1ms, which leads to an acceleration of the atoms due to gravity corresponding to an initial kick. The trapping potential has a Gaussian shape and can only in the center be approximated by a harmonic trapping potential. The error, due to the anharmonicity of the Gaussian potential becomes relevant at an oscillation amplitude larger than 10% of the waist, thus the amplitudes of the resulting oscillations are adjusted to be about  $5\mu\text{m}$ <sup>1</sup>. The uncertainty of the deduced frequencies is on the order of 1%.

To measure the trapping frequency in the third ( $z$ -) direction, both excitations are performed at the same time. Due to a small asymmetry in the setup, an angular momentum

<sup>1</sup>The waist of the beams and thus the characteristic length scale of the potential is on the order of  $50\text{-}60\mu\text{m}$ .

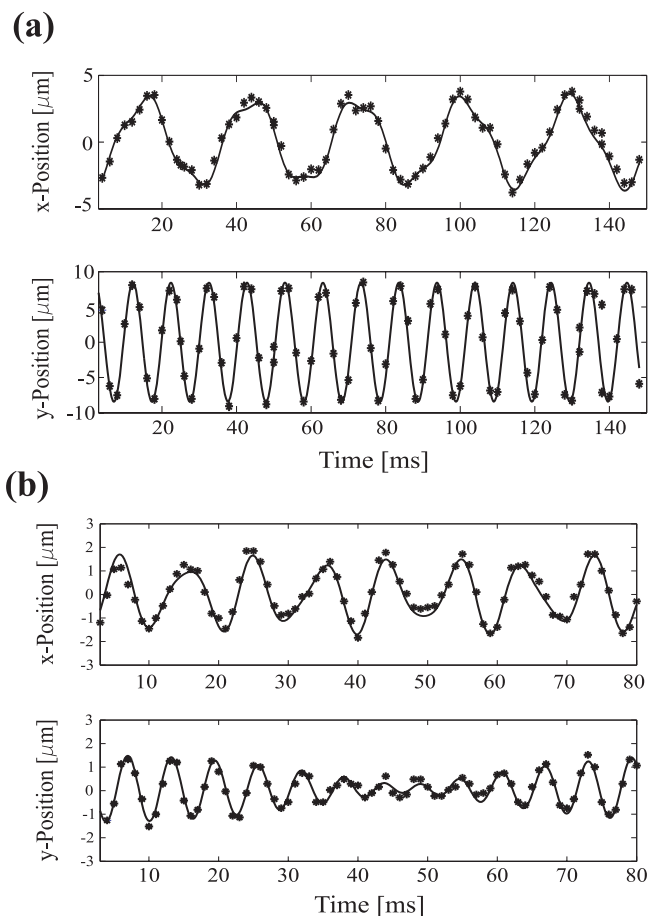


Figure 3.12: Calibration of the harmonic trap. The filled circles correspond to the measured center of mass position of the BEC at different evolution times after the excitation in the trap. The solid lines show a least-square fit of a sinusoidal oscillation including a possible beating with a second frequency. The upper part of the two figures show the evolution in the  $x$ -direction and the lower graphs in the  $y$ -direction. The resulting frequencies are (a)  $\omega_x = 2\pi \times 35.0 \pm 0.5\text{Hz}$ ,  $\omega_{x,\text{beat}} = 2\pi \times 98.7 \pm 0.8\text{Hz}$ ;  $\omega_y = 2\pi \times 98.1 \pm 0.5\text{Hz}$  and (b)  $\omega_x = 2\pi \times 103.1 \pm 0.5\text{Hz}$ ,  $\omega_{x,\text{beat}} = 2\pi \times 160.6 \pm 1.5\text{Hz}$ ;  $\omega_y = 2\pi \times 153.2 \pm 1.2\text{Hz}$ ,  $\omega_{y,\text{beat}} = 2\pi \times 165.0 \pm 0.9\text{Hz}$ . As the beating signal in the  $y$ -direction in (b) has only one node, the beating frequency deduced from it is not accurate. For experiments both beating frequencies are only considered, if also longer evolution times are measured.

is added to the atoms leading to a rotation of the oscillation in the  $xz$ - and in some cases also in the  $yz$ -plane. This rotation manifests itself in a periodic increase and decrease of the oscillation amplitude corresponding to a beating of the harmonic oscillation with a third frequency as shown in Fig. 3.12. The frequencies are adjusted, such that there is at least a difference of 10Hz between the oscillation in the  $x$ - and in the  $z$ -direction leading to a beating frequency more than 10Hz, which can be deduced accurately by measuring the center of mass position for holding times up to 100ms. If the frequency in the  $z$ -direction is close to the frequency in the  $y$ -direction, as is the case in Fig. 3.12 (a), the beating in the  $yz$ -plane is too slow to be observed within 100ms. If the frequencies differ by at least 10Hz, a beating in the  $yz$ -plane becomes evident, as shown in Fig. 3.12 (b).

### 3.2.5 Parameters of the periodic potential

In order to determine the exact shape of the periodic potential two different quantities have to be known, namely the periodicity and the height of the periodic potential. The periodicity can be accessed directly by loading a BEC into a deep periodic potential with only low harmonic confinement and fitting the resulting density distribution with a Gaussian envelope modulated by a cosine function as shown in Fig. 3.13. The spacing of the potential is typically on the order of  $5\mu\text{m}$  and is given by the angle between the two interfering beams and their wavelength as discussed in Sec. 3.1.4. However, also the angle between the symmetry axis of the potential and the imaging axis of  $12.3^\circ$  has to be taken into account (see Fig. 3.10).

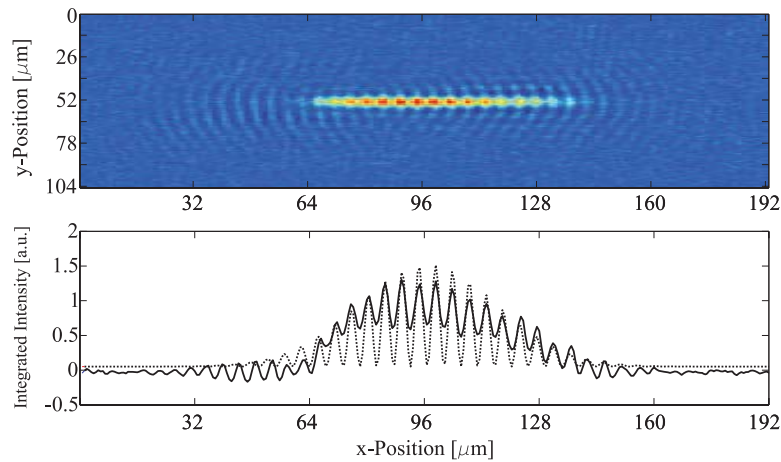


Figure 3.13: Measurement of the periodicity of the periodic potential. (a) shows the absorption image of a BEC confined in a deep periodic potential. (b) shows its density profile integrated perpendicularly to the interference structures and is fitted with a Gaussian envelope modulated by a cosine function. The periodicity of the cosine directly corresponds to the lattice spacing, when the tilt of the periodic structure with respect to the imaging system is taken into account. The periodicity is approximately  $5\mu\text{m}$  with an accuracy of less than 5%.

The calibration of the height of the periodic potential is more involved, as it is not possible to apply standard calibration methods using e.g. Bragg diffraction or other methods involving the transfer of the lattice momenta to the BEC, because the lattice spacing is too large corresponding to only very small momenta ( $v \sim 1\mu\text{m}/\text{ms}$ ). The method used for calibration relies on the excitation of a dipolar oscillation of two BEC in a deep double well potential. In the double well trap, the separation of the two minima depends on the height of the periodic potential (see Sec. 3.1.5). With increasing barrier height and decreasing harmonic confinement the distance of the wells is increased leading to the excitation of a dipolar oscillation of the two matter wave packets in opposite directions.

For this measurement, a BEC is prepared in a shallow double well trap and, to initiate the dynamics and maximize the oscillation amplitude, the periodic potential is ramped up quickly to a high value and at the same time the harmonic longitudinal confinement is turned off. In order not to excite the two BEC too much, the periodic potential is ramped up with  $V_f(t) = V_f - (V_f - V_i) \exp(-t/\tau)$ , where  $\tau = 1\text{ms}$ ,  $V_i$  is the initial potential height and  $V_f$  the final potential height. By monitoring the distance between the two center of mass positions, and comparing them with numeric simulations of the experiment at different final periodic potentials, the height of the standing light wave can be fitted accurately. Numeric simulations have to be used as the size of the matter wave packets is comparable to half the

lattice periodicity leading to non-harmonic oscillations. This method is discussed in more detail in [47]. Fig. 3.14 (a) shows the standard deviation of the experimental data to the numeric simulations at different potential heights. The minimum is around  $1370 \pm 15\text{Hz}$ . (b) shows the comparison of the experimental data and the numeric simulation at the potential height corresponding to the smallest standard deviation. The simulations were performed by solving the 3-D GPE as discussed in Appendix B in the initial potential to find the ground state and subsequently, using real time propagation and changing the potential in time according to the experimental protocol.

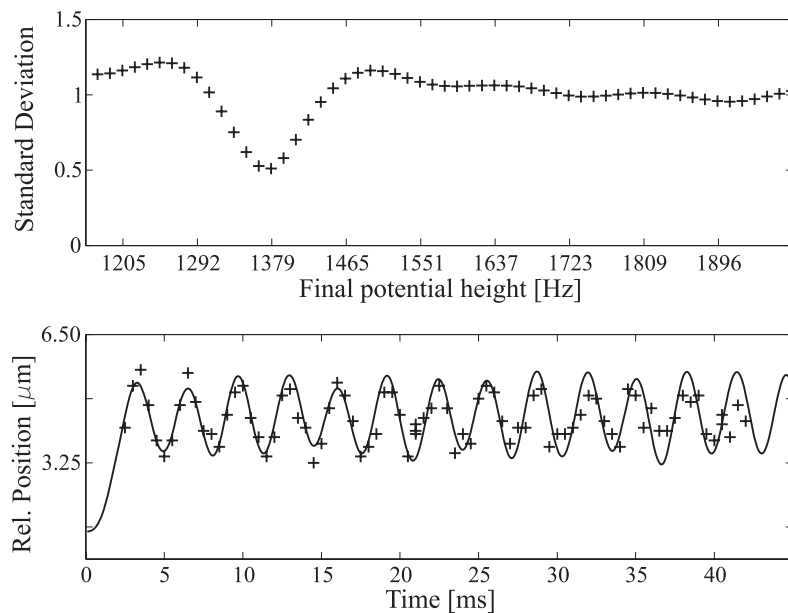


Figure 3.14: Calibration of the height of the periodic potential. The periodic potential is calibrated by exciting dipolar oscillation of the two BEC in a deep double well potential in opposite directions and comparing the center of mass positions with numerical simulations. (a) shows the standard deviation of the experimental data to the numerical simulations for different periodic potential heights. The minimum is around  $1370 \pm 15\text{Hz}$ . In (b) the temporal evolution of the distance between the two center of mass positions is compared with the numerical simulation at the potential height leading to the smallest standard deviation. The agreement is very good even though, the amplitude of the oscillations is only about  $1\mu\text{m}$ .

### 3.3 Experimental access to the observables

With absorption imaging techniques only local density distributions can be measured. The reconstruction of the wave function in the two mode approximation is only possible if both, the density and the momentum distribution are known. The density distribution is accessed by in situ imaging of the atoms in the double well trap and the momentum distribution by imaging the density distribution in the far field, after a time of flight. From these measurements the two dynamical variables, the population imbalance and the relative phase, are deduced.

#### 3.3.1 Density distribution - population imbalance

The population imbalance is obtained by fitting two overlapping Gaussian functions to the density distribution either in 2-D directly to the absorption images or in 1-D by previously

integrating over the image in the transverse direction. However, the accuracy of the fitting is not very good, as the separation of the two matter wave packets in the double well trap ( $\sim 4.4\mu\text{m}$ ) is only slightly larger than the optical resolution ( $3\mu\text{m}$ ). Furthermore, the barrier height is comparable to the chemical potential leading to broad matter wave packets and a large spatial overlap. To improve the accuracy, the distance between the two wave packets is increased by a similar procedure as used for the calibration of the standing light wave. The measurement is done by rapidly (within  $200\mu\text{s}$ ) ramping up the height of the standing light wave and simultaneously turning off the longitudinal confinement (XDT). The minima of the two wells move apart and a dipolar oscillation of the two matter wave packets is induced. As the two BEC move in opposite directions, their distance increases and the overlap of the two matter wave packets is reduced. The images are taken when the separation of the two matter wave packets is maximal. The local trapping frequencies are on the order of  $250\text{Hz}$  leading to a waiting time of about  $2\text{ms}$ . During the  $200\mu\text{s}$  of ramping the tunneling probability is negligible and the final barrier height is chosen such that within the few milliseconds the tunneling rate does not play a role either. With this, the population imbalance is frozen during the few milliseconds of the measurement.

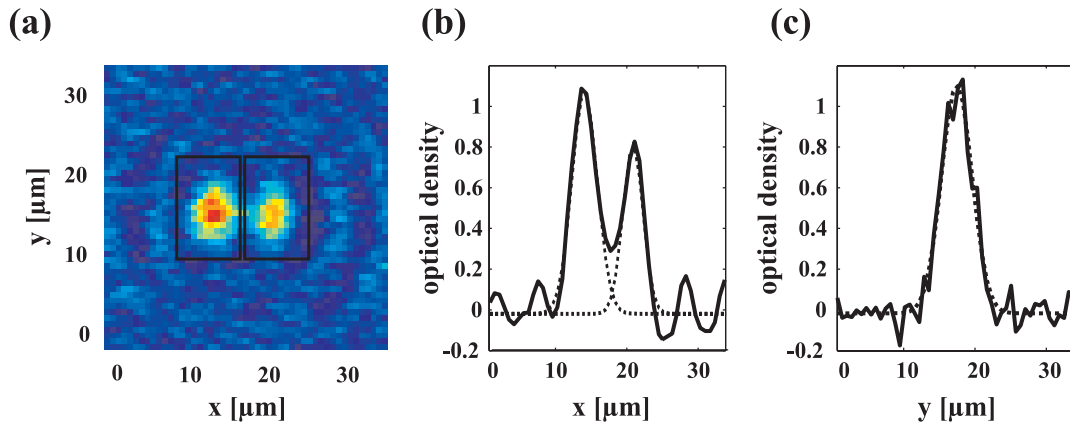


Figure 3.15: Measurement of the population imbalance. In (a) absorption image of the BEC in the double well potential are shown. Here, the distance of the two matter wave packets is increased by exciting dipolar oscillations into opposite directions and imaging, when the separation is maximal. The additional structure around the atomic cloud result from the fact, that the size of the individual matter wave packets in the  $x$ -direction is approximately a factor of two smaller than the optical resolution. In (b) the density profile in the  $x$ -direction (solid line) is plotted. It can be well approximated by a sum of two Gaussian functions (dashed lines). (c) shows the profile in  $y$ -direction, which is fitted by a single Gaussian function. The atom numbers of within the two wells can be calculated from the amplitudes and the waists of the fit.

Fig. 3.15 (a) shows a typical absorption image of atoms in the double well trap. The population imbalance is deduced from such images by fitting the transverse size of the wave packets with a Gaussian function and the longitudinal profile with two overlapping Gaussian functions as shown in (b). The population of the modes is calculated from the amplitudes and waist of the fitted functions.

### 3.3.2 Momentum distribution - relative phase

The relative phase is deduced from time of flight images as shown in Fig. 3.16 (a). The atoms are released from the double well trap by turning off all potentials within  $200\mu\text{s}$  and taking

the images after a time of flight of between 5 and 8ms. During this time, the matter wave packets fall down due to gravity, but also expand due to the stored kinetic and interaction energy and interfere with each other. The resulting patterns are transversally Gaussian and longitudinally a Gaussian envelope modulated by a cosine.

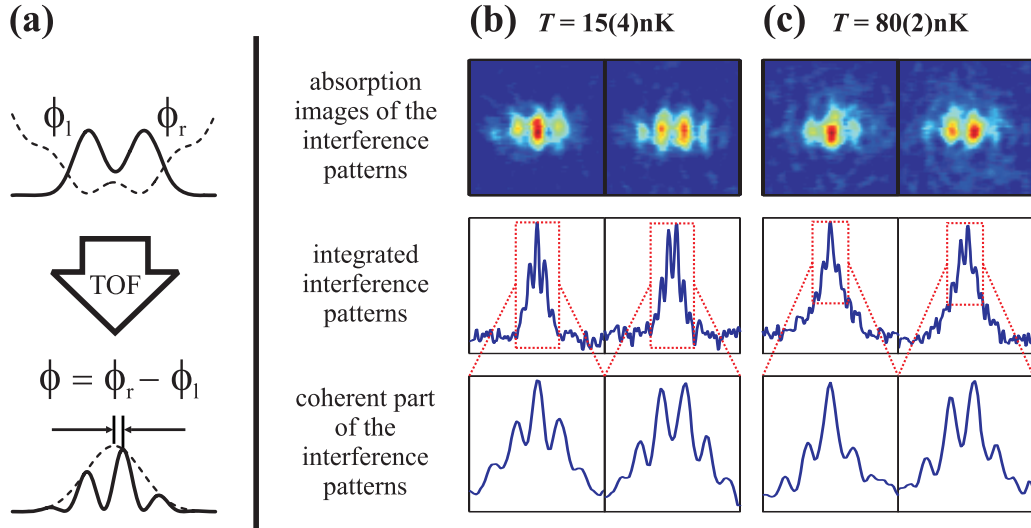


Figure 3.16: Matter wave interference patterns. (a) is a sketch of the interference experiments. Once the double well trap is turned off, the matter wave packets expand, overlap and interfere revealing the relative phase as a shift of the interference peaks with respect to their envelope. (b) corresponds to typical interference patterns at  $\phi \approx 0$  and  $\phi \approx \pi$  at low temperatures and (c) to typical interference patterns at high temperatures. The integrated patterns show a clear interference signal for all temperatures (central graphs). However, for high temperatures also a broad background is visible, corresponding to the distribution of the thermal atoms after the expansion time. In order to find the coherent interference patterns, this background is subtracted (lower graphs).

Typical interference images for low temperature ( $T \ll T_c$ ) are shown in Fig. 3.16 (b) and for high temperature ( $T \lesssim T_c$ ) in (c). The upper part of the graph shows the absorption images, where in (b) the interference patterns are very clear but in (c) a broad background is visible. The middle part of the graphs show the transversally integrated interference profiles revealing that for high temperature the interference patterns are on top of the background, making an accurate phase deduction impossible. Thus, the thermal background is fitted transversally and then subtracted from the interference patterns. The resulting profiles are shown on the lower part of the graphs revealing that the visibility of the interference patterns does not depend on temperature and is typically between 40% and 50%.



---

## 4 Properties of and fluctuations in the bosonic Josephson junction in steady state

The detailed knowledge of the initial state of the system is indispensable for any experiment. Thus, in order to be able to study the behavior of a bosonic Josephson junction, its steady state properties should be known. The state of the BJJ in the two mode approximation can be described by the expectation value of the population imbalance and the relative phase, and their higher momenta. In steady state, due to the symmetry of the Hamiltonian, the expectation values of both quantities have to be zero. However, the higher momenta can vary, which is connected to the fluctuation of the two variables from measurement to measurement. Apart from technical noise, two different kinds of fluctuations are distinguishable, the quantum mechanical fluctuations resulting from the quantum mechanical uncertainty and thermally induced fluctuations. The high and the low temperature limit is reached, if the fluctuations are dominated by thermal or by quantum processes.

### 4.1 Zero temperature limit

In the zero temperature limit for bosonic Josephson junctions the additional energy stored in the system in form of excitations of atoms into higher lying states is low and allows only for a few excitations. In this case, only the two lowest lying single particle mean field orbitals are populated. In the Rabi regime, the lowest two energy levels differ by  $2E_j/N$ , in the Josephson regime by  $\hbar\omega_p$  and in the Fock regime by  $E_c/2$ . So far experiments could not be performed in the double well potential in this limit. However, in periodic potentials it is possible to generate a trap geometry, where the excitation energy is well above the thermal energy scale and thus, thermally induced processes are negligible. In this system, e.g. the transition from the Josephson regime to the Fock regime was observed experimentally by investigating the superfluid properties of a Bose-Einstein condensate confined in a 3-D optical lattice [89]. The transition between the regimes was triggered by increasing the height of the periodic potentials and could be deduced from the loss of coherence in interference experiments. The results were compared to the well-known superfluid to Mott transition in solid-state physics.

At zero temperature in a symmetric double well, the expectation values of the population imbalance and the relative phase vanish, but both variables show quantum mechanical fluctuations as discussed in Sec. 2.4.2. The ground state of the BJJ is characterized by a uniform phase and thus the relative phase between the two wells in steady state is always zero. However, by introducing an energy asymmetry between the two wells, the ground state population imbalance can be manipulated.

### 4.1.1 Asymmetric double well potential

The ground state population imbalance of the bosonic Josephson junction can be manipulated by implementing a double well potential with different potential depths in the two wells. For the double well potential defined in Eq. 3.13, which consists of a harmonic trapping potential and a periodic potential, such an asymmetry is introduced if the position of the harmonic trap with respect to the standing light wave is changed. A shift of  $\Delta x$  leads to the effective potential

$$\begin{aligned} V_{\text{dw-asymm}} &= \frac{1}{2}m(\omega_x^2(x - \Delta x)^2 + \omega_y^2 y^2 + \omega_z^2 z^2) + \frac{V_0}{2} \left( 1 + \cos \frac{2\pi}{d_{\text{sw}}} x \right) \\ &= V_{\text{dw}} - m\omega_x^2 \Delta x x + \text{const.}, \end{aligned} \quad (4.1)$$

where the shift is equivalent to an additional potential gradient. The resulting Bose-Hubbard Hamiltonian for the asymmetric double well potential has the form

$$\begin{aligned} \hat{H}_{2\text{M-asymm}} &= \hat{H}_{2\text{M}} - \Delta x \cdot \delta \cdot \left( \frac{\hat{c}_r^\dagger \hat{c}_r - \hat{c}_l^\dagger \hat{c}_l}{2} \right) \\ &= \frac{E_c}{2} \hat{n}^2 - \Delta x \cdot \delta \cdot \hat{n} - E_j \hat{\alpha}_+ \\ &= \frac{E_c}{2} \left( \hat{n} - \frac{\Delta x \cdot \delta}{E_c} \right)^2 - E_j \hat{\alpha}_+ + \text{const.}, \end{aligned} \quad (4.2)$$

with the coupling constant

$$\delta = 2m\omega_x^2 \int d\mathbf{r} \Phi_s^* x \Phi_a. \quad (4.3)$$

From Eq. 4.2 it follows, that the ground state in the asymmetric double well trap has a population imbalance of  $\Delta n_0 = \Delta x \cdot \delta / E_c$ . The distribution of the relative phase remains unchanged in the asymmetric double well potential, however the coherence is reduced, as  $\langle \hat{\alpha}_+ \rangle$  corresponds to the visibility of averaged interference patterns and their visibility depends on the relative amplitudes of the two interfering modes.

In the Gross Pitaevskii model a similar term appears

$$H_{\text{GP-asymm}} = E_c \frac{n^2}{2} - E_j \sqrt{1 - \frac{4n^2}{N^2}} \cos \phi - \Delta x \cdot \delta \cdot n, \quad (4.4)$$

leading to the same predictions for the ground state population imbalance.

### 4.1.2 Steady state population imbalance in the asymmetric double well

To measure the ground state population imbalance experimentally we prepared a Bose-Einstein condensate in the ground state of an asymmetric double well potential. The asymmetry was experimentally realized by changing the position of the harmonic trapping potential with respect to the standing light wave by means of the piezo actuated mount.

The initial state of the BJJ was prepared by condensing  $1450 \pm 250$  atoms in a 3-D harmonic trapping potential with trapping frequencies  $\omega_x = 2\pi \times 78(1)\text{Hz}$ ,  $\omega_y = 2\pi \times 66(1)\text{Hz}$  and  $\omega_z = 2\pi \times 90(1)\text{Hz}$ . To prepare the BJJ adiabatically the standing light wave with periodicity  $d_{\text{sw}} = 5.2(2)\mu\text{m}$  was raised within 1s to a height of  $580(10)\text{Hz}$ . The tunneling coupling, the charging energy and the energy shift were calculated by solving the Gross-Pitaevskii equation in 3-D and were  $E_j/h = 1.17\text{kHz}$ ,  $E_c/h = 0.32\text{Hz}$ , and  $\delta/h = 231\text{Hz}/\mu\text{m}$ .

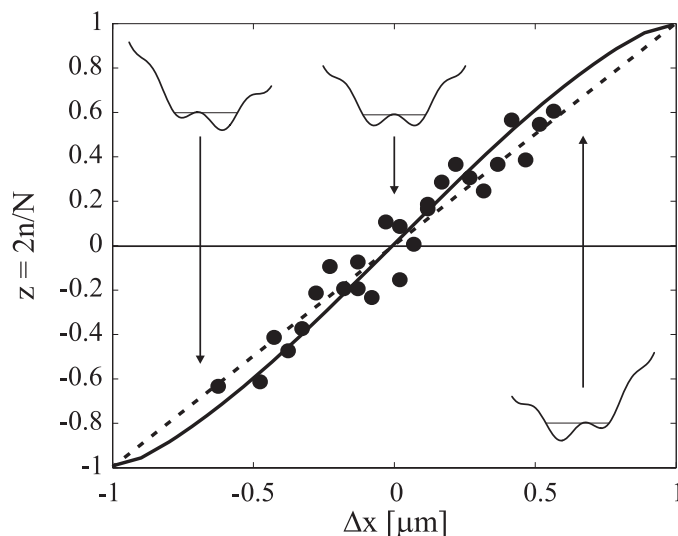


Figure 4.1: Steady state population imbalance as a function of the shift of the harmonic trapping potential. The solid line is the solution of the 3-D Gross-Pitaevskii equation and the dashed line is the prediction of the Bose-Hubbard model. The comparison reveals, that the steady state population imbalance of the bosonic Josephson junction can be predicted accurately using both theoretical models.

The experimentally observed steady state population imbalances are plotted in Fig. 4.1 as a function of the shift of the harmonic trapping potential. The solid line is the solution of the 3-D Gross-Pitaevskii equation and the dashed line is the prediction of the Bose-Hubbard model. The data is in good agreement with both theoretical predictions within the experimental error. The discrepancy between the Bose-Hubbard and the Gross-Pitaevskii model results from the fact, that in the two mode approximation the change of the ground state wave function is not taken into account. Due to the asymmetry, the densities are modified and thus, the atom-atom interactions result in a change of the shape of the wave functions.

## 4.2 Steady state fluctuations at finite temperature

At finite temperature, the fluctuation of the dynamical variables are larger than the corresponding quantum mechanical uncertainties. The reason for these thermally induced fluctuations is the equilibration of the bosonic Josephson junction with its thermal environment due to a coupling of the condensed particles to particles in higher excited states. According to the Bose-Einstein distribution (Eq. 2.1) in a double well potential, not only the ground state but also the first excited state will be macroscopically populated, if the energy difference between the ground and the first excited state is smaller than the thermal energy scale. To calculate the effect of the temperature we neglect the back action of the thermal excitations on the mean field wave functions and the exchange of particles. Thus, the interaction of the BJJ with its thermal background takes place only via a transfer of energy.

The density matrix of the mixed state at finite temperature is given in the eigenstate basis by the population of the eigenstates according to the Boltzmann distribution

$$\hat{\rho}_{\text{th}} = \frac{1}{C} \sum_{e=0}^N \exp\left(-\frac{\langle e|\hat{H}|e\rangle}{k_B T}\right) |e\rangle\langle e|, \quad (4.5)$$

where the states  $|e\rangle$  are the  $N + 1$  eigenstates of the Hamiltonian and  $C$  is a normalization constant.

At finite temperature in steady state, the coherence factor  $\alpha = \langle \hat{\alpha}_+ \rangle = \text{Tr}(\hat{\rho}_{\text{th}} \hat{\alpha}_+)$  defined in Eq. 2.55 is also a good measure for the coherence of the system and is connected to the amount of phase fluctuations in general. It can be understood as the mean fringe visibility of ensemble averaged interference patterns.

#### 4.2.1 Low temperature limit

The low temperature regime is defined as the range corresponding to temperatures on the order of the plasma frequency  $\hbar\omega_p$  up to the tunneling coupling energy  $E_j$ . In this regime, both quantum and thermal fluctuations play a role, but their overall contribution is small enough so that the coherence factor is close to one. Following a Bogoliubov approach, we can calculate analytically the expression of the coherence factor. As shown in [33], starting from the two mode Hamiltonian, the Bogoliubov transformation is straightforward since only one quasiparticle mode can exist. The transformed Bogoliubov Hamiltonian writes

$$\hat{H}_{\text{Bg}} = E_{\text{Bg}}(N) + \hbar\omega_p(\hat{g}^\dagger \hat{g} + 1/2). \quad (4.6)$$

$E_{\text{Bg}}(N)$  is a constant energy term. The excitation creation operator is  $\hat{g}^\dagger = u\hat{c}_e^\dagger + v\hat{c}_e$  where  $u = \cosh \chi$ ,  $v = \sinh \chi$  and  $\tanh 2\chi = E_C/(E_C + 8E_J/N^2)$  [33]. The obtained excitation spectrum corresponds to the linear part of the exact spectrum plotted in Fig. 2.1 (a).

To determine the coherence factor, we calculate the number of atoms in the antisymmetric state by

$$\begin{aligned} n_e &= \langle \hat{c}_e^\dagger \hat{c}_e \rangle \\ &= \langle \hat{g}^\dagger \hat{g} \rangle (u^2 + v^2) + v^2. \end{aligned} \quad (4.7)$$

We find the usual formula for the condensate depletion, the first term corresponds to thermal fluctuations and the second term to the quantum depletion. The coherence factor is then

$$\langle \alpha \rangle = 1 - 2\frac{n_e}{N} \simeq 1 - \frac{1}{2} \sqrt{\frac{E_C}{E_j}} \left( \frac{1}{\exp(\hbar\omega_p/k_B T) - 1} + \frac{1}{2} \right). \quad (4.8)$$

In the last equality, we have used the assumption that the BJJ is in the Josephson regime ( $E_J/N^2 \ll E_C$ ). The decoherence due to quantum fluctuations is proportional to  $\sqrt{E_C/E_J}$  and is always small in the Josephson regime.

#### 4.2.2 High temperature limit

For temperatures much higher than the mean quantum mechanical level spacing, which is approximately given at low energies by the plasma energy ( $\hbar\omega_p$ ), a semi-classical calculation of the thermally averaged fringe visibility is valid. In this limit the many body two mode Hamiltonian (Eq. 2.47) corresponds to the classical Hamilton function (Eq. 2.93) and the coherence factor is the mean value of  $\cos \phi$ , which writes

$$\begin{aligned} \langle \cos \phi \rangle &= \frac{1}{Z} \int d\phi dn \cos \phi \exp(-H_{\text{GP-2M}}/k_B T) \\ \text{with } Z &= \int d\phi dn \exp(-H_{\text{GP-2M}}/k_B T). \end{aligned} \quad (4.9)$$

In the Josephson regime, the relatively strong interaction term prevents any contribution of large values of  $n$  in the previous integral. The coherence factor can then be approximated by ([32])

$$\alpha = \langle \cos \phi \rangle = \frac{\int d\phi \cos \phi \exp\left(-\frac{E_j}{k_B T} \cos \phi\right)}{\int d\phi \exp\left(-\frac{E_j}{k_B T} \cos \phi\right)} = \frac{I_1\left(\frac{E_j}{k_B T}\right)}{I_0\left(\frac{E_j}{k_B T}\right)}, \quad (4.10)$$

where  $I_i(j)$  are the modified Bessel functions of the first kind. At high temperature, this analytic expression is in good agreement with the prediction of the Bose-Hubbard model.

### 4.2.3 Experimental observation of thermal fluctuations in steady state

For the experimental investigation of thermal fluctuations in the bosonic Josephson junction, the distribution of the relative phase was measured as a function of the temperature, the barrier height and the atom numbers [48]. The experiments were performed by condensing about 2000 to 10000 atoms in the 3-D harmonic trap with trapping frequencies  $\omega_x = 2\pi \times 90(2)\text{Hz}$  and  $\omega_y = \omega_z = 2\pi \times 100(2)\text{Hz}$  at the lowest possible temperature of about  $T = 10\text{nK}$ . Subsequently, the temperature was increased by keeping the atoms in the harmonic trap for different holding times, where due to fluctuations of the trap parameters energy was transferred to the atoms. For these experiments, it was crucial that the temperature could be deduced independently, thus the adjusted temperatures were in the range of  $T = 50$  to  $80\text{nK}$ , which could be accurately measured by standard thermometry methods. The atom number of the initial condensate was chosen such that after the heating process the number of the condensed particles stayed in the range of 1900 to 3600 atoms.

Once the Bose gas was prepared in the 3-D harmonic trap, the standing light wave with a periodicity of  $d_{\text{sw}} = 4.8(2)\mu\text{m}$  was raised within 300ms to its final value between  $V_0/h = 500\text{Hz}$  and  $2000\text{Hz}$ . The resulting coupling constants were  $E_j/k_B$  between  $1.6\text{nK}$  and  $640\text{nK}$  and  $E_c/k_B$  between  $13\text{pK}$  and  $21\text{pK}$ . The plasma energy ranged between  $\hbar\omega_p/k_B = 0.1\text{nK}$  and  $4\text{nK}$  and the tunneling times varied between  $\tau_p = 12\text{ms}$  and  $500\text{ms}$ . The precise values depend strongly on the atom numbers and the barrier height and were calculated by solving the GPE in 3-D using the method discussed in Appendix B. The functional dependence of  $E_j$  and  $E_c$  was fitted for the relevant range and the resulting parameters are shown in Appendix C. After the ramp, all potentials were turned off within  $200\mu\text{s}$  and the resulting interference patterns were imaged after 5 or 6ms time of flight.

The qualitative analysis of the phase fluctuations is shown in Fig. 4.2, where polar plots of relative phase measurements are shown. Every open circle corresponds to a single interference experiment and the solid lines sketch twice the standard deviation. In (a), the barrier height was kept constant leading to a tunneling coupling of  $E_j/k_B T = 69(25)\text{nK}$  and the temperature was varied between  $T = 15(4)\text{nK}$  and  $75(2)\text{nK}$ . The fluctuations clearly increase with temperature. In (b) the temperature was kept constant at  $T = 15(4)\text{nK}$  and the barrier height changed such that the tunneling coupling varied between  $E_j/k_B T = 39(17)\text{pK}$  and  $378(90)\text{nK}$ . Here, the fluctuations decrease with increasing coupling.

For the accessible parameter range quantum fluctuations are very small and do not change the theoretical expectation within the experimental error

$$\Delta\phi_{\text{th}}^2 = \frac{k_B T}{E_j} \gg \Delta\phi_{\text{qm}}^2 = \frac{1}{2} \sqrt{\frac{(E_c + 4E_j/N^2)}{E_j}} \Rightarrow k_B T \gg \frac{\hbar}{2} \omega_p, \quad (4.11)$$

where the plasma frequency  $\omega_p$  is defined in Eq. 2.53. In the Josephson regime, quantum

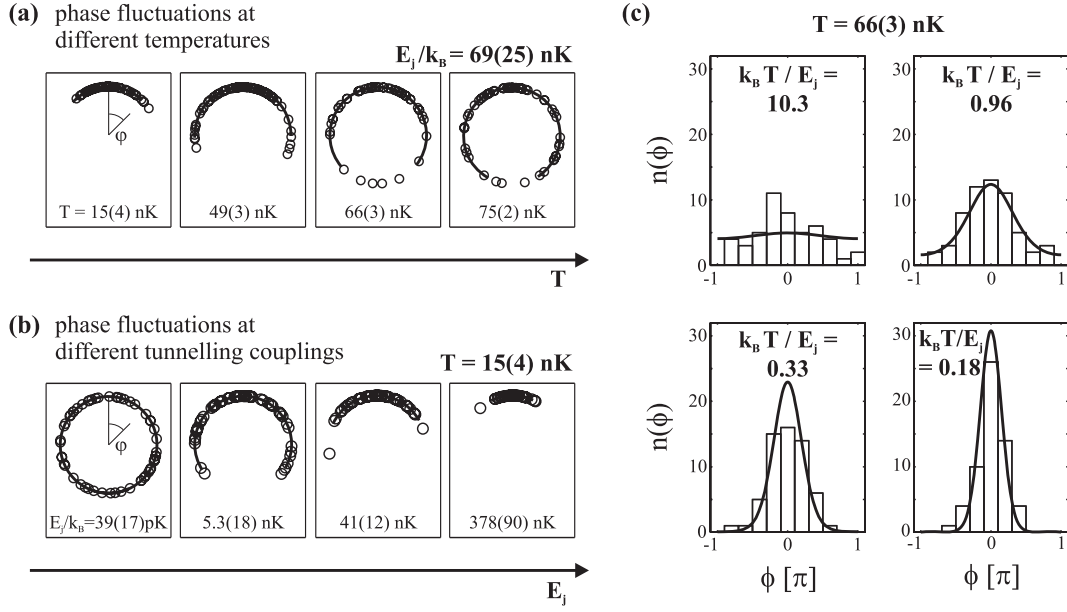


Figure 4.2: Thermally induced fluctuations. (a) shows polar plots of relative phase measurements for a fixed barrier height leading to a constant tunneling coupling and for different temperatures. Every open circle corresponds to a single realization of the interference measurement. The solid lines indicate twice the standard deviation of the phase in both directions. The amount of fluctuations increases with temperature. (b) corresponds to similar experiments, but here the temperature is fixed and the barrier height varied, in order to realize different tunneling couplings. The fluctuations decrease with the tunneling coupling. (c) shows four typical distribution functions in form of histograms for different ratios of  $k_B T / E_j$ . The histograms are compared to the theoretical prediction of the classical model (solid lines) revealing a good agreement.

mechanical fluctuations are negligible if the thermal energy is much larger than the plasma energy. For the performed experiments this yields  $k_B T / \hbar \omega_p > 10$ .

The measured coherence factors  $\alpha$  as a function of the scaling parameter  $k_B T / E_j$  are shown in Fig. 4.3. Here, for every temperature and barrier height, about 100 measurements were performed and every data point in the graph corresponds to a subset extracted from these measurements for different atom number ranges (e.g. 2000 to 2500, 2500 to 3000 etc. atoms in the condensate fraction). Each data point represents at least 28 and on average 40 measurements. The coherence factor was calculated by averaging over the cosine of the fitted phases. The tunneling coupling  $E_j$  was deduced for every point at the given trap parameters and the mean atom numbers in the condensate fraction by numerically solving the Gross-Pitaevskii equation in 3-D. The influence of atoms in excited states was neglected.

The temperatures were determined by using different methods in order to cross check the results. Before and after the measurement of every data set independent time of flight measurements were performed, where the cloud was released from the 3-D harmonic trap. As discussed in Sec. 2.1.3 the temperature could be deduced from the ratio of condensed to the total number of particles. In Fig. 4.4, the results of this method (solid line) are compared to the temperatures deduced from the expansion velocity of the thermal background (stars). The measurements are in good agreement with exception of the first data point. However, this point corresponds to a temperature far below the critical temperature making a fitting of the size of the thermal background difficult.

Furthermore, the temperature could also be deduced from the interference patterns, where

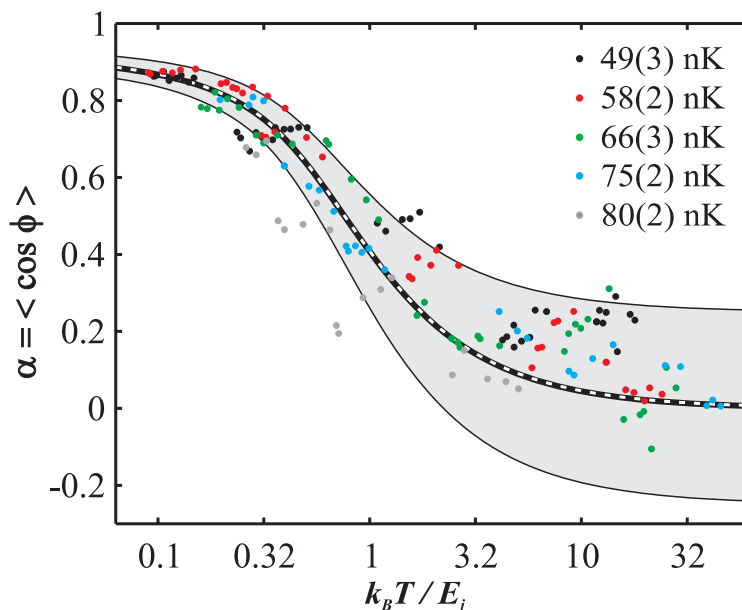


Figure 4.3: Experimental investigation of the coherence factor  $\alpha$ . The graph shows the quantitative behavior of the coherence factor  $\alpha$  as a function of the scaling parameter  $k_B T / E_j$ . Each data point corresponds to the average of at least 28 (typically about 40) single measurements for different  $T$  and  $E_j$ . The temperature is measured independently with a time of flight method and the tunneling coupling is deduced from 3-D simulations of the BJJ using the independently measured system parameters (potential parameters and atom numbers). The experimental error of  $k_B T / E_j$  is about  $\pm 30\%$ . The central black line corresponds to the prediction of the Bose-Hubbard theory and the white dashed line is the prediction of the classical theory, where both calculations take the uncertainty of the phase-fitting into account. The gray shaded area shows twice the expected standard deviation of the coherence factor due to the finite number of measurements. The behavior of the coherence factor is confirmed over a three orders of magnitude change of the scaling parameter.

transversally the thermal background was visible. The squares in Fig. 4.4 correspond to the temperatures deduced from the ratio of condensed to the total number of particles in the interference patterns. The fitting uncertainty of the transverse width of the thermal background was too large for an accurate deduction of the temperature and thus it is not shown in the graph.

The typical error of  $k_B T / E_j$  is  $\pm 30\%$ . The error in  $E_j$  results from the uncertainty of the atom numbers, the trapping frequencies, the barrier height and the lattice spacing of the periodic potential. The error in  $T$  results from the fitting error of the waists and amplitudes of the bimodal distribution of the independent time of flight measurements.

The central black line in Fig. 4.3 shows the theoretical prediction of the Bose-Hubbard model for the coherence factor and the white dashed line is the prediction of the high temperature limit, both are taking the fitting error of the relative phases into account. The influence of the fitting error on the coherence factor is estimated by averaging over an additional fluctuating phase. The distribution of this additional phase is approximated by a box function with a width of  $2\phi_0$  corresponding to the standard deviation of  $\Delta\phi$ , which is the standard deviation resulting from the fitting error. The averaging leads to a reduction of the coherence

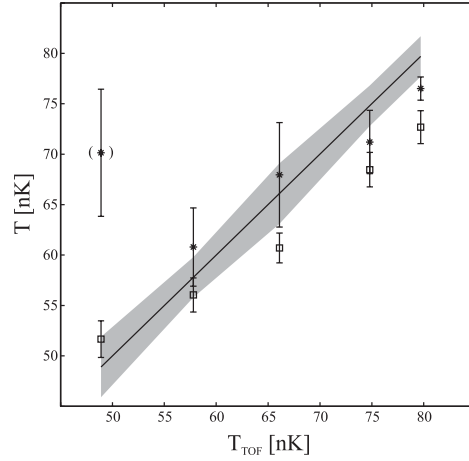


Figure 4.4: Different methods for deducing the temperature of the atoms. The reference (black line) corresponds to the deduction of the temperature from the ratio of the condensed to the total number of particles from independent time of flight measurements. The gray shaded area shows the fitting uncertainty. The stars indicate the temperature deduced from the same measurement, but from the expansion velocity of the thermal background. The boxes correspond to the temperature deduced from the interference patterns, where transversally the thermal background was visible. The temperature is here obtained from the ratio of the condensed to the total number of particles.

factor

$$\begin{aligned}
 \alpha' = \langle \cos(\phi) \rangle' &= \frac{\int_{-\phi_0}^{\phi_0} d\phi' \int_{-\pi}^{\pi} d\phi \cos(\phi - \phi') \exp(E_j/k_B T \cos(\phi))}{\int_{-\phi_0}^{\phi_0} d\phi' \int_{-\pi}^{\pi} d\phi \exp(E_j/k_B T \cos(\phi))} \\
 &= \frac{\sin(\phi_0)}{\phi_0} \frac{\int_{-\pi}^{\pi} d\phi \cos(\phi) \exp(E_j/k_B T \cos(\phi))}{\int_{-\pi}^{\pi} d\phi \exp(E_j/k_B T \cos(\phi))} \\
 &= \frac{\sin(\phi_0)}{\phi_0} \cdot \alpha.
 \end{aligned} \tag{4.12}$$

For our experiments,  $\phi_0$  is equal to  $0.23\pi$  which corresponds to a fitting error of the relative phase of

$$\Delta\phi = \sqrt{\frac{1}{2\phi_0} \int_{-\phi_0}^{\phi_0} d\phi \phi^2} = 0.13\pi, \tag{4.13}$$

and to a reduction of the coherence factor of  $\alpha' = 0.92\alpha$ . The gray shaded area in Fig. 4.3 shows twice the standard deviation of the coherence factor resulting from the statistically expected error. For about 40 measurements, it is approximately  $\Delta\alpha \approx 0.13 \cdot (1 - \alpha)$ .

The dependence of the coherence factor on  $T$  and  $E_j$  is consistent with the prediction of the two mode model over a wide range. For small values of  $k_B T/E_j$ , the coherence factor is in close agreement with the theoretical prediction. However, for  $k_B T/E_j > 2$ , the data points lie within the experimental error but are mainly localized above the curve. This deviation can be explained by the fact that the BJJ is not thermalized for small  $E_j$  (see Sec. 4.2.4). The points corresponding to a high temperature of 80nK lie outside the shaded region revealing a lower degree of coherence. A disagreement in this regime can also be expected as the temperature is close to the critical temperature of  $T_c \approx 87$  nK. The analogy with superconducting Josephson junctions, where a deviation close to  $T_c$  has been predicted [90], is under investigation.

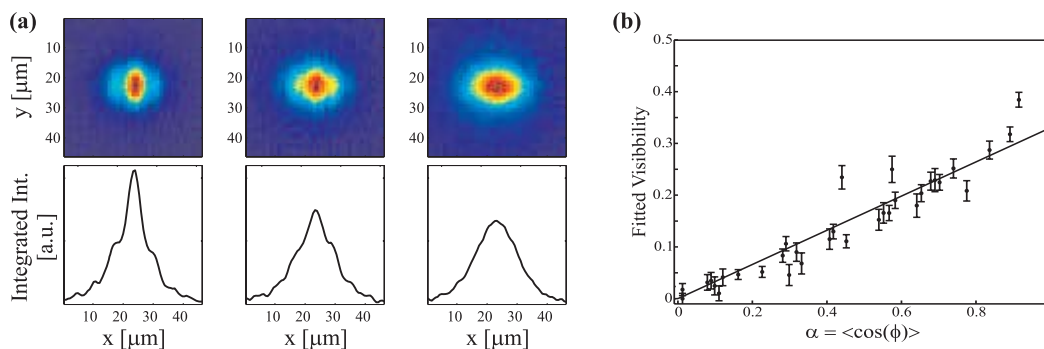


Figure 4.5: Ensemble averaged visibility of the interference patterns. Every graph in (a) corresponds to the average of 60 interference patterns at a temperature of 58(2)nK. In the first graph the tunneling coupling was adjusted to  $E_j/h = 243$ nK, in the second to 15nK, and in the third to 0.8nK. The fluctuations increase with decreasing coupling and the visibility of the interference patterns is reduced until for very small couplings it vanishes. In (b) the coherence factors resulting from the measured phase distributions are compared to the ensemble averaged visibility of the interference patterns. A linear dependence with a slope of 0.3 is found, which corresponds mainly to the visibility of the single interference patterns resulting from the finite optical resolution.

The coherence factor corresponds directly to the ideal visibility of ensemble averaged interference patterns, which is demonstrated in Fig. 4.5. In (a), three typical averaged interference patterns are shown. The temperature was chosen to be 58(2)nK and 60 interference patterns were added up for the graphs. For a large tunneling coupling (first graph  $E_j/k_B = 243$ nK), the phase fluctuates only slightly leading to no reduction of the visibility of the interference patterns with respect to the single realization. With decreasing coupling (second graph  $E_j/k_B = 15$ nK and third graph  $E_j/k_B = 0.8$ nK) the fluctuations increase and the visibility is reduced. The quantitative comparison of the visibility and the coherence factor is shown in (b). Here, a linear dependence with a slope of 0.3 is visible, which corresponds to the visibility of single interference patterns.

#### 4.2.4 Thermalization and thermometry

Using the standard time of flight method, temperatures cannot be measured far below the critical temperature. This method leads to accurate results only if the number of particles in the thermal background is large enough for detection. However, by measuring phase fluctuations it is possible to deduce the temperature accurately, even if the number of particles in excited states is very small. This possibility relies on the scaling behavior of the coherence factor, where for every temperature the tunneling coupling can be adjusted, such that the ratio is close to one and the distribution of the phase is sensitive on the exact temperature.

With this method, the temperature is deduced by measuring the phase distribution, calculating the tunneling coupling numerically and comparing the coherence factor with the theoretical prediction. However, one difficulty for such experiments is the adiabatic preparation of the BJJ. For very low temperatures the tunneling coupling has to be very small ( $E_j < 3k_B T$ ) in order to allow for the observation of phase fluctuations and the tunneling time becomes long. Thus, in order to keep the BJJ in the thermal equilibrium during preparation, the barrier has to be raised at a rate, which is much slower than the typical tunneling time.

To test on what timescale the ramping has to be performed in order to keep the BJJ in

the thermal equilibrium, we compare the coherence factor measurements with the theoretical prediction from Eq. 4.10. We introduce an effective tunneling coupling  $E_j^{\text{eff}}$  to account for non-equilibrium situations and deduce  $k_B T/E_j^{\text{eff}}$  for the experimental data shown in Fig. 4.3. In Fig. 4.6, the ratio  $E_j^{\text{eff}}/E_j$  is plotted as a function of the tunneling time  $\tau_p = 2\pi/\omega_p \propto 1/\sqrt{E_j}$ . We find that for the chosen ramping time of 300ms the effective tunneling coupling is only equal to the expected tunneling coupling for  $\tau_p < 50\text{ms}$ . The observed increase of  $E_j^{\text{eff}}$  for large tunneling times ( $\tau_p > 50\text{ms}$  which corresponds to  $E_j < 60\text{nK}$ ) could be explained by the fact that the system still did not reach the equilibrium after the 300ms ramp.

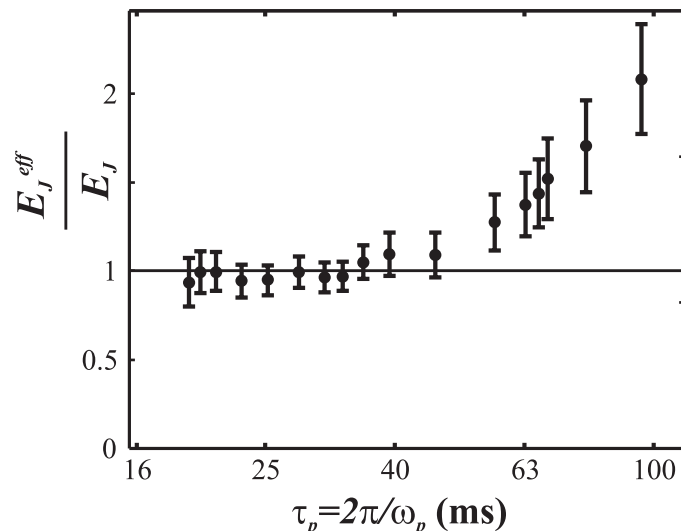


Figure 4.6: Experimental test for thermal equilibration of the BJJ. The graph shows the measured coherence factors as a function of the tunneling time. The experimental  $E_j^{\text{eff}}$  are deduced by fitting the measured coherence factor to the theoretical prediction. For tunneling times  $\tau_p \leq 50\text{ms}$  the ratio is one. For  $\tau_p > 50\text{ms}$  the ratio increases, which can be explained by the fact, that the BJJ is not completely thermalized. With this we can conclude, that thermalization takes only place if the tunneling time is much faster than the ramping time of the barrier  $\tau_p \ll t_{\text{ramp}} = 300\text{ms}$ .

#### 4.2.5 Application of the noise thermometer

To test the applicability of the new thermometer, we measured the heating up of a degenerate Bose gas in a 3-D harmonic trap. For this, the BEC was prepared at the lowest accessible temperature and the distributions of the relative phase were measured after different holding times, by ramping up the barrier within 300ms to barrier heights corresponding to a coupling strength on the order of the thermal energy scale. About 60 interference patterns were produced for every holding time. At higher temperatures, where the thermal fraction became visible, also time of flight measurements from the 3-D harmonic trap were performed. The results are shown in Fig. 4.7. The filled circles correspond to temperature measurements using the phase fluctuation method and the open circles to measurements using the standard time of flight method. For these measurements, the total number of atoms in the trap was kept constant. Thus, the phase fluctuation measurements could only be performed within the first 6s, as long as the condensate fraction was large enough to observe clear interference patterns. Below 30nK, the time of flight method could not be applied as the number of particles in excited states was too small for detection.

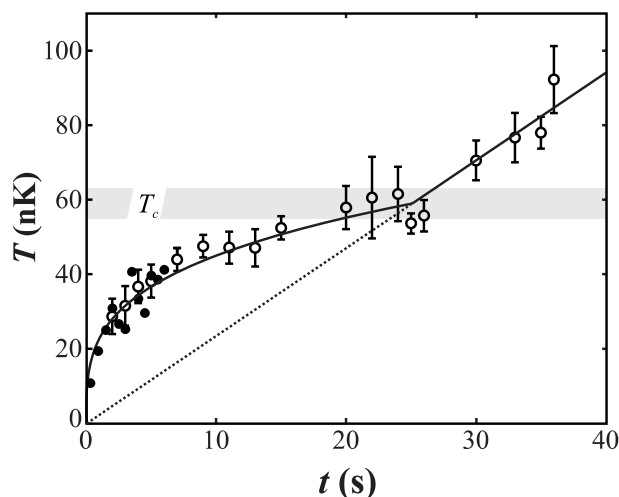


Figure 4.7: Thermometry using phase fluctuation measurements. The graph shows the application of the phase thermometer. The temperature of a degenerate Bose gas is plotted as a function of the holding time in the harmonic trap. The filled circles correspond to measurements using the phase fluctuation method (for the points with  $\tau_p > 50$  ms, we correct the deduced temperatures using the effective tunneling couplings plotted in Fig. 4.6 (b)). The open circles are temperature measurements applying the standard time of flight method. In the overlap region both methods lead to the same results, showing the applicability of the noise thermometer. The black line is a fitting function assuming a constant transfer rate of energy, a power law for the temperature dependent heat capacity below the critical temperature and a constant heat capacity above. The measurements demonstrate the deviation of the heat capacity of the Bose gas from the classical gas as expected due to the third law of thermodynamics.

The non-linear increase in temperature can be explained by assuming a constant and state-independent transfer rate of energy per particle and taking the temperature dependence of the heat capacity of a degenerate Bose gas into account. For short holding times, a fast increase of the temperature corresponding to a large heating rate was found. The heating rate decreased then continuously until at 25s the critical temperature was reached. Above the critical temperature, the heating rate stayed constant. To deduce the dependence of the heat capacity on the temperature from the measurement, we assume a power law dependence on temperature  $(T/T_c)^d$  below  $T_c$  and a constant value above [91]. The expected temporal evolution is then approximately governed by

$$T(t) = \begin{cases} \sqrt[d+1]{h_0 T_c^d t + T(0)^{d+1}} & \text{for } T_{\text{fit}} < T_c \\ h_0 t + T(0) & \text{for } T_{\text{fit}} \geq T_c, \end{cases} \quad (4.14)$$

where  $h_0$  is the constant energy transfer rate. The critical temperature was deduced from independent measurements of the trap parameters and atom numbers and lead to  $T_c = 59.1$ nK. Using the function given in Eq. 4.14 to fit the observed temperature increase, we obtain  $h_0 = 2.4(1)$ nK and a dimensionality parameter  $d = 2.4(4)$ .

The most likely source of heating in these experiments are fluctuations of the trap position and the trapping frequencies. The heating due to fluctuations of the trap position corresponds to a constant increase of energy per time and particle and the heating due to fluctuations of the trapping frequencies (parametric heating) to an exponential increase of the energy [92]. The fitting with a function taking both heating processes into account reveals that the additional increase due to parametric heating is very small and results in a correction of

the temperature of below 7% after 36s and leads to  $d = 2.7(7)$ . Thus, the assumption of a constant transfer rate of energy describes the experimental situation very well.

The observation of the heating for temperatures far below the critical temperature is the low temperature extension of the heat capacity measurements already performed in the early days of BEC [93]. The dimensionality deduced from our data is slightly smaller than the theoretical prediction, as expected due to the presence of atom-atom interactions [94]. Clearly, the dependence of the heat capacity on the temperature with  $d > 1$  confirms the prediction of the third law of thermodynamics [95] stating, that the heat capacity of any real system has to vanish in the zero temperature limit.

---

## 5 Dynamical properties of the bosonic Josephson junction

The dynamical response of the bosonic Josephson junction to low energetic excitation can be calculated in the many body two mode description as discussed in [24, 25, 33, 73, 96, 97, 98]. The temporal evolution of the wave function is governed by the time propagation of the density matrix with

$$\hat{\rho}(t) = e^{-i\hat{H}t/\hbar} \hat{\rho}(t=0) e^{i\hat{H}t/\hbar} \quad \text{with} \quad \hat{\rho} = |\hat{\Psi}\rangle\langle\hat{\Psi}|. \quad (5.1)$$

In the eigenstate basis, the time propagation operator corresponds to a phase propagation of the eigenstates according to their energy.

The expected dynamical behavior of the BJJ in the three dynamical regimes (Rabi, Josephson, Fock) can be understood by the structure of the energy spectrum and the eigenstate wave functions. In Fig. 5.1 the eigenstates and the eigenenergies of the Bose-Hubbard Hamiltonian for  $N = 100$  are shown in the Rabi regime (a), in the Josephson regime (b) and in the Fock regime (c). The eigenstates in the Rabi regime are the SU(2) coherent states and show a linear, harmonic oscillator like energy spectrum. In the Fock regime, the eigenstates are localized atom number states and the energy spectrum is similar to the energy spectrum of a free particle. In the Josephson regime for low energies  $E < 2E_j$ , the eigenstates are similar to coherent states with a well defined phase and for high energies  $E > 2E_j$  they are similar to Fock states with a well defined atom number. Thus, the energy spectrum is linear below  $2E_j$  and quadratic above.

In the Rabi regime, the eigenstate wave functions and the energy spectrum are similar to that of a harmonic oscillator. Consequently, the dynamical response of the BJJ to low energetic excitations are harmonic oscillations (plasma oscillation). In the Fock regime, the eigenstates are localized in the atom number basis and every energy (except of the ground state at an even number of particles) consist of a quasi degenerate doublet of a symmetric and an antisymmetric state. The preparation of a Fock state in a single well, hence consists of the superposition of such two degenerate states and will show no temporal evolution. The preparation of many Fock states however, will keep the mean population imbalance constant, as the populated doublets are not evolving, but the energy difference between the doublets will lead to a rapid oscillation on top. The dynamical response in the Josephson regime depends on the preparation of the initial state. For low energetic excitations ( $E < 2E_j$ ) the BJJ shows plasma oscillations and for high energetic excitations ( $E > 2E_j$ ) self trapping, in analogy to the dynamics in the Fock regime.

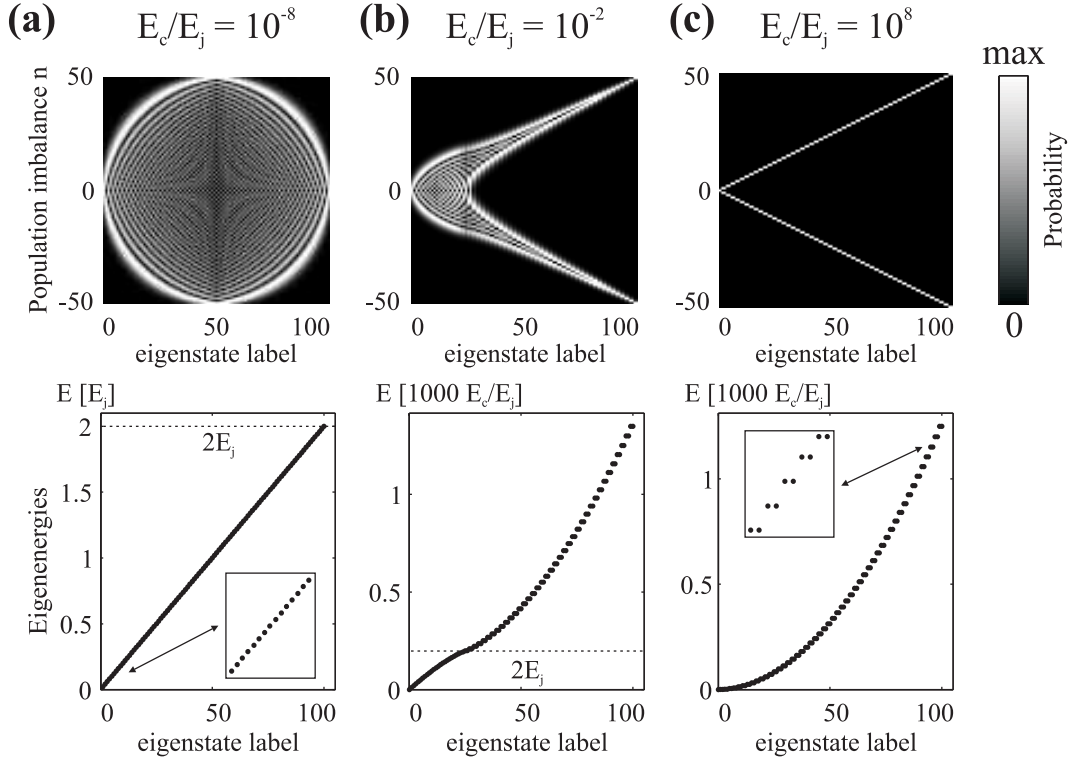


Figure 5.1: Eigenstates and energy spectra of the Bose-Hubbard Hamiltonian in the three dynamical regimes. (a) shows the coherent eigenstates in the Rabi regime, which are strongly delocalized. The energy scale is only determined by the tunneling coupling and the eigenenergies increase linearly with the eigenstate label. (b) corresponds to the Josephson regime, where the low lying excitations are delocalized and coherent and the higher excitations are well localized atom number states. In (c) the eigenstates in the Fock regime are shown. The strong localization is evident and the energy, which is dominated by the interaction energy, shows a quadratic increase. Every eigenenergy is two fold degenerate and corresponds to well defined atom number states at  $n$  and  $-n$ .

## 5.1 Dynamical regimes

For a quantitative understanding of the dynamical response in the Bose-Hubbard picture the temporal evolution has to be calculated numerically. However, insight can be won by using the Gross-Pitaevskii two mode description and deriving the equation of motion for  $n$  and  $\phi$  from the Gross-Pitaevskii two mode Hamilton function (Eq. 2.93) using the Hamilton formalism (see e.g. [24, 25, 26, 27, 28, 98, 99, 100, 101]). The equations of motion are

$$\frac{dn}{dt} = -\frac{1}{\hbar} \frac{\partial H}{\partial \phi} = -\frac{E_j}{\hbar} \sqrt{1 - \frac{4n^2}{N^2}} \sin \phi \quad (5.2)$$

$$\frac{d\phi}{dt} = \frac{1}{\hbar} \frac{\partial H}{\partial n} = \frac{E_c}{\hbar} n + \frac{E_j}{\hbar} \frac{4n}{N^2} \left( \sqrt{1 - \frac{4n^2}{N^2}} \right)^{-1} \cos(\phi). \quad (5.3)$$

For the initial conditions  $n = 0$  and  $\phi = 2\pi j$  with  $j \in \mathbb{N}$ , the equations of motion vanish and the system is in the ground state at rest. In the case  $n = 0$  and  $\phi = \pi(1 + 2j)$  with  $j \in \mathbb{N}$  the system is at rest as well, but this state corresponds to a meta-stable state only. If one of the two variables is prepared to a different initial value, a particle flow will start through the barrier and compensate for the imbalance. In the case of an energetic asymmetry between

the two wells, an additional term (from Eq.4.4) appears in the time derivative of the phase leading to

$$\frac{d\phi}{dt} = \frac{E_c}{\hbar} n + \frac{E_j}{\hbar} \frac{4n}{N^2} \left( \sqrt{1 - \frac{4n^2}{N^2}} \right)^{-1} \cos(\phi) - \delta\Delta x. \quad (5.4)$$

From the equations of motion, three dynamical regimes can be distinguished. The zero phase modes, the self trapped modes, and the  $\pi$ -phase modes.

### 5.1.1 Plasma oscillations

The zero phase modes, are periodic oscillations of both dynamical variables  $n$  and  $\phi$  around zero. For small initial amplitudes (i.e.  $\sin \phi_0 \approx \phi_0$  and  $n_0^2 \ll N^2$ ) the equation of motion can be linearized

$$\frac{dn}{dt} \approx -\frac{E_j}{\hbar} \phi, \quad \frac{d\phi}{dt} \approx \left( \frac{E_c}{\hbar} + \frac{4E_j}{\hbar N^2} \right) n, \quad (5.5)$$

and give rise to harmonic oscillations of the dynamical variables

$$n(t) = \sin(\omega_p t + \theta_{\text{init}}), \quad (5.6)$$

where  $\theta_{\text{init}}$  is an initial phase depending on the initial conditions. The frequency of the small amplitude oscillations is called the plasma frequency and the oscillations are referred to as plasma oscillations. For larger amplitudes, the oscillations become anharmonic and the equations of motion can be solved in terms of Jacobian elliptic functions as discussed in [28]. The oscillation frequency in this regime depends on the initial conditions and decreases with the oscillation amplitude.

### 5.1.2 Self trapping

Self trapping corresponds to dynamical modes, for which the population imbalance shows only small oscillation around a non-zero value and the phase winds up. Self trapping occurs if the dynamics of the BJJ is initiated at a zero relative phase by a population imbalance, which is larger than a critical value  $n(t=0) > n_c$  (see Eq. 2.99). With increasing initial phase difference the critical population imbalance decreases.

Fig. 5.2 shows the comparison of the predictions of the equations of motion (solution of Eq. 5.2 and Eq. 5.3, dashed lines) and the numeric simulation of the many body system (solid lines) for  $N = 100$  and  $E_c/E_j = 0.01$ . The gray shaded areas corresponds to plus/minus the expectation value of the fluctuation operators of the respective quantities. In the upper graphs the temporal evolution of the population imbalance is plotted and in the lower graphs the temporal evolution of the relative phase. For the three graphs, different initial conditions are prepared, by starting with the ground state of different asymmetric double well potentials. The initial population differences are  $n(0) = 9.6$  (a), 19.2 (b), and 28.7 (c). The dynamics is initiated, when the energy asymmetry is lifted.

In the zero-phase mode regime, the GP prediction is in good agreement with the many body calculation. A small reduction of the oscillation amplitude in the many body case can be found for long oscillation times. In the case of self trapping, the GP prediction is in good agreement with the many body calculation for short times, but the oscillations disappear rapidly due to a dephasing of the populated atom number states. Close to the critical population imbalance however, the GP prediction is only valid for a very short time. It starts to deviate strongly from the many body description, when the relative phase approaches

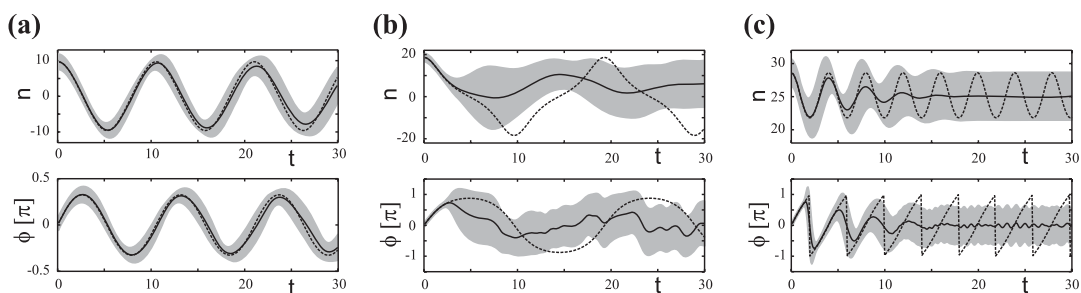


Figure 5.2: Dynamics of the bosonic Josephson junction at  $N = 100$  and  $E_c/E_j = 0.01$  at  $T = 0$ . The graphs show the temporal evolution of the dynamical variables  $n$  (upper graphs) and  $\phi$  (lower graphs) calculated with the GP model (dotted lines) and the many body model (solid lines). The gray shaded area corresponds to plus/minus the fluctuations of the respective quantities. The dynamics in (a) is initiated by a population imbalance of  $n(0) = 9.6$  and shows the plasma oscillation. In (b) it starts with a population imbalance of  $n(0) = 19.2$ , which is slightly below the critical population imbalance of  $n_c = 19.6$ . In (c) the dynamics is initiated with a population imbalance of  $n(0) = 28.7$  and shows self trapping.

$\pi$ . This is due to the fact, that in the many body case not only a single Fock state, but many atom number states are populated. Thus, at the critical population imbalance there are states which are self trapped but also states which are not. By increasing the number of particles, the deviations become less relevant and the classical equations can be used to predict the behavior of the BJJ also for longer times.

### 5.1.3 Phase plane portrait

The dynamical response of the bosonic Josephson junction can be visualized in the phase plane portrait, where the population imbalance is plotted versus the relative phase (modulo  $2\pi$ ). A typical phase plane portrait is shown in Fig. 5.3 (a) for  $N = 100$  and  $E_c/E_j = 0.01$  (Josephson regime). In the central part of the graph, the periodic oscillations in the plasma oscillation regime are indicated by ellipsoids. Above and below the self trapped states are plotted. The two regimes are separated by the separatrix, which is characterized by the initial condition  $n_0 = \pm n_c$  at  $\phi_0 = 0$ .

### 5.1.4 $\pi$ -Phase modes

Plasma oscillations and self trapping can also be observed in superconducting and superfluid Josephson junctions. However, due to the nonlinear character of the atom-atom interactions, a new regime becomes also accessible. In this regime, the average value of the relative phase is not zero but  $\pi$ . In the  $\pi$ -oscillation regime, small amplitude oscillations exist but also self trapped states. As this regime was experimentally not accessible so far, I refer to the discussion of  $\pi$ -oscillations in [28].

## 5.2 Experimental observation of the dynamical response

The experimental investigation of the dynamics of a single bosonic Josephson junction was discussed in [46]. The initial state of the BJJ was prepared by condensing 1150 atoms (where the number of atoms was fixed by post selection to be between 1000 and 1300) in a 3-D harmonic trapping potential with trapping frequencies  $\omega_x = 2\pi \times 78(1)\text{Hz}$ ,  $\omega_y = 2\pi \times 66(1)\text{Hz}$

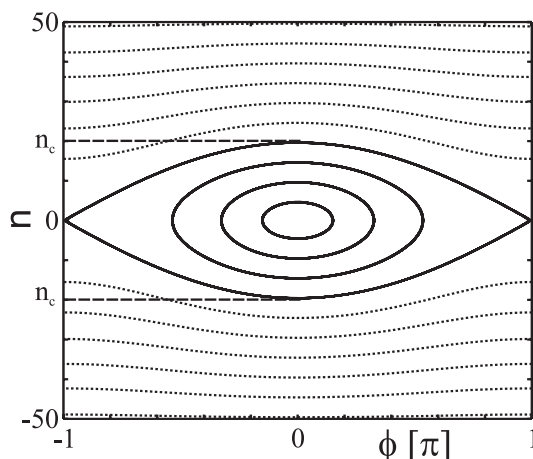


Figure 5.3: Dynamics of the bosonic Josephson junction at  $N = 100$  and  $E_c/E_j = 0.01$  in the phase plane portrait. The graph shows the two relevant dynamical regimes, where the ellipsoids correspond to the zero-phase modes and the dotted lines to the self trapped modes. The separatrix, which has the initial conditions  $n = \pm n_c$  and  $\phi = 0$ , divides the phase plane into these two regimes.

and  $\omega_z = 2\pi \times 90(1)\text{Hz}$ . The temperature of the Bose gas was below 20nK. To prepare the BJJ adiabatically, the standing light wave with periodicity  $d_{\text{sw}} = 5.2(2)\mu\text{m}$  was raised within 1s to a height of  $V_0/h = 420(5)\text{Hz}^1$ . The ramping time was chosen to be much slower than the tunneling times at the final barrier height, which was expected to be on the order of 30ms. The coupling constants were calculated by solving the Gross-Pitaevskii equation in 3-D and were  $E_j/h = 3.15\text{kHz}$ ,  $E_c/h = 0.33\text{Hz}$ ,  $\delta E/h = 0.14\text{mHz}$  and  $\delta/h = 204\text{Hz}/\mu\text{m}$  leading to the plasma frequency of  $\omega_p = 2\pi \times 33\text{Hz}$  and the thermally induced fluctuations of the dynamical variables of  $\Delta\phi = 0.1\pi$  and  $\Delta n = 36$ . The thermal fluctuations were small compared to the change of the dynamical variables during the evolution and thus lead only to a small uncertainty of the initial conditions.

To initiate the dynamics, different population imbalances were prepared by changing the initial position of the harmonic trapping potential with respect to the periodic potential. The initial population imbalances are shown in Fig. 5.4. The plasma oscillation regime (indicated by the gray shaded area) is separated from the self trapping regime by the critical initial population imbalance of  $n_c = 193$ . The three data points correspond to the symmetric double well for  $\Delta x = 0$  leading to  $n(0) = 0$ , the plasma oscillation regime for  $\Delta x = 240(80)\text{nm}$  leading to  $n(0) = 161(35)$  and the self trapping regime for  $\Delta x = 500(80)\text{nm}$  leading to  $n(0) = 357(35)$ . The theoretical expectation resulting from the solution of the 3-D GPE is indicated by the solid line.

After the preparation of a Bose-Einstein condensate in the asymmetric double well potential, the tunneling dynamics was initiated by slowly moving the harmonic trap to  $\Delta x = 0$  and realizing a symmetric double well. In order not to excite any dynamics within the wells the shift was performed slower than the inverse local trapping frequencies of  $2\pi/\omega_{\text{loc}} \approx 3\text{ms}$ , but much faster than the tunneling time of about 30ms. The time constant for moving the harmonic trap was chosen to be  $\tau_{\text{xdt}} = 5\text{ms}$  with a time dependence of the position of  $x_{\text{xdt}} = \Delta x \cdot \exp(-t/\tau_{\text{xdt}})$ . The temporal evolution of the density distribution and its compar-

<sup>1</sup>The difference between the previously in [46] reported value of  $V_0/h = 412(20)\text{Hz}$  and the new value of  $V_0/h = 420(5)\text{Hz}$  for the barrier height results from an improved method for deducing the height of the standing light wave by using 3-D numerical simulations instead of the non-polynomial Schrödinger equation for calibrating  $V_0$ .

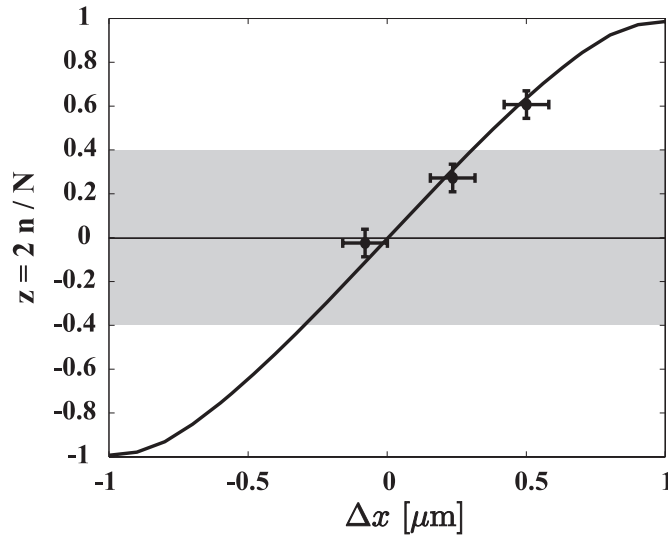


Figure 5.4: Initial population imbalance as a function of the shift of the harmonic trapping potential. The three data points correspond to the initial population imbalances in the symmetric double well, in the plasma oscillation regime and in the self trapping regime. The solid line is a prediction resulting from the numerical solution of the 3-D Gross-Pitaevskii equation. The gray shaded area shows the plasma oscillation regime, below and above there is the self trapping regime.

Comparison with numerical simulations are shown in Fig. 5.5. The simulations have been performed by propagating the 3-D Gross-Pitaevskii equation in imaginary time to find the ground state wave functions and subsequently propagating in real time for the temporal evolution as discussed in Appendix B. Two initial conditions were chosen, a population imbalance below the critical value for self trapping (a) and an initial value above (b). The initial relative phase in both cases was zero. For the population imbalance below the critical value, the tunneling dynamics is visible, where particles move from the left well to the right and back. For the initial value above, the BJJ is self trapped and no dynamics is visible in the density. The comparison to the numerical simulations reveals, that the density distribution behaves as expected. The differences between the graphs of the numerical simulations and the experimental data are dominantly resulting from the optical resolution of the imaging setup.

The measurement of the temporal evolution in both dynamical regimes (plasma oscillations and self trapping) is shown in Fig. 5.6. In the Josephson regime (Fig. 5.6 (a)), both variables oscillate around a zero mean value. The population imbalance starts with the prepared initial value and the relative phase with zero. In the self trapping regime as shown in Fig. 5.6 (b), the population imbalance is locked (within the experimental error) and the phase winds up. The error bars of the relative phases correspond to the standard deviation of the measured phases at the corresponding evolution time.

The theoretical prediction of the temporal evolution is indicated by the solid lines, which are calculated by performing 3-D simulations of the Gross-Pitaevskii equation using only the independently measured trap parameters, atom numbers and shifts of the harmonic trap. Quantitative agreement with the experimental data is only achieved, if also the finite shifting time of  $\tau_{\text{xdt}} = 5\text{ms}$  is taken into account. Furthermore, a detailed analysis showed that the harmonic trap did not reach the designated position, but stopped in average about 40nm before, which is well within the experimental uncertainty of 80nm. The gray shaded regions in Fig. 5.6 correspond to the experimental uncertainties of the respective quantities and

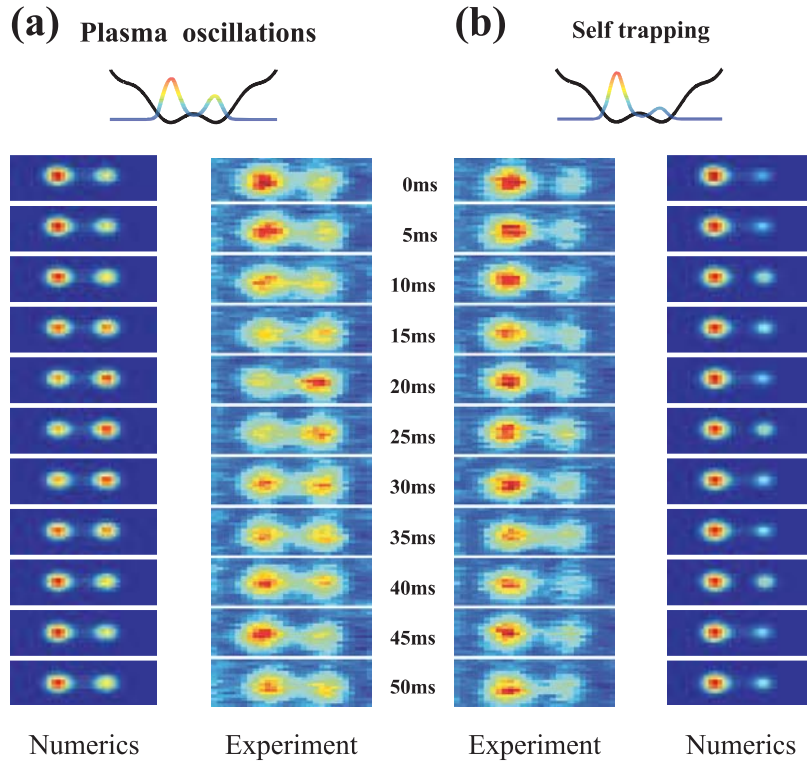


Figure 5.5: Tunneling dynamics in the double well trap. The temporal evolution of the density distribution in the double well trap is shown for a small initial imbalance (a) and a large initial imbalance (b). For an imbalance below the critical value for self trapping the BJJ is in the plasma oscillation regime and shows a tunneling dynamics of atoms from the left well to the right and back. If the initial population imbalance is above the critical value, the BJJ is in the self trapping regime and no dynamics is visible in the density distribution. The difference between the numerical simulations (see Appendix B) and the experimental data are mainly resulting from the optical resolution of the imaging setup.

were calculated by performing numerical simulations of the experiment with different atom numbers and initial position of the harmonic trap. The atom numbers ranged between 1000 and 1300 and the position of the harmonic trap in the plasma oscillation regime was  $-240 \pm 40\text{nm}$  (the jump was 200nm) and in the self trapping regime of  $-500 \pm 40\text{nm}$  (with a jump of 460nm). The coupling constants resulting from the 3-D calculation of the ground and the first excited state are basically unchanged in the case of  $\Delta x = -40\text{nm}$  and lead for the experimental parameters to  $E_j/h = 3.14\text{kHz}$ ,  $E_c/h = 0.33\text{Hz}$ ,  $\delta E/h = 0.14\text{mHz}$  and  $\delta/h = 204\text{Hz}/\mu\text{m}$ . However, the uncertainty of the barrier height, the atom numbers and the spacing of the standing light wave lead to a large uncertainty of the coupling constants of  $E_j \pm \Delta E_j = h \times 2.33$  to  $4.14\text{kHz}$ ,  $E_c \pm \Delta E_c = h \times 0.30$  to  $0.35\text{Hz}$  and  $\delta E \pm \Delta(\delta E) = h \times 0.12$  to  $0.16\text{mHz}$ .

The expected tunneling frequency according to the two mode model varies between  $\tau_p = 29\text{ms}$  and  $37\text{ms}$ , which is faster than the experimentally found  $40(2)\text{ms}$ . This deviation might be a result of the change of the transverse size of the matter wave packets during the tunneling (by  $\sigma_{\min}/\sigma_{\max} = 0.7$ ), which is not taken into account by the two mode model. However, the amplitudes of the oscillations are correctly accounted for as shown in the phase plane diagram in Fig. 5.7, where the normalized population imbalance is plotted versus the relative phase.

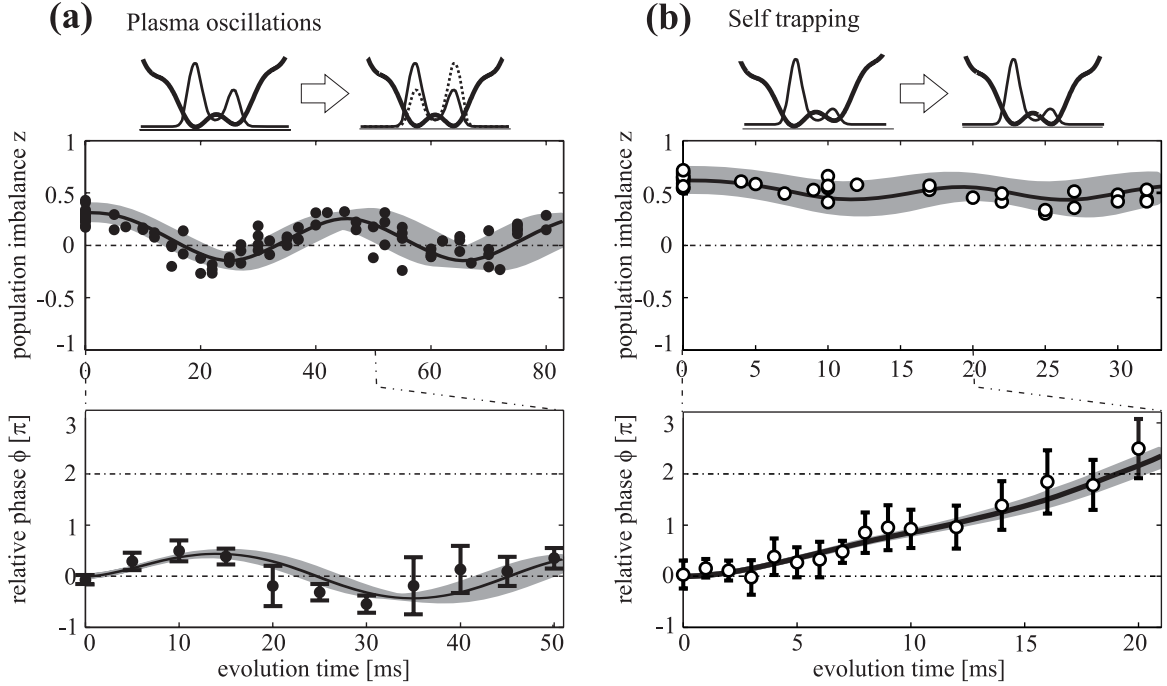


Figure 5.6: Dynamical response of the bosonic Josephson junction. (a) shows the measurement of the temporal evolution of the population imbalance (upper graph) and the relative phase (lower graph) in the Josephson regime. The dynamics is initiated by a population imbalance of  $n(0) = 161(35)$ . Both dynamical variables show oscillations with a zero mean value. The deduced timescale of the oscillations is  $40(2)$ ms. (b) shows the measurement of the temporal evolution of the two dynamical variables in the self trapping regime, where the dynamics is initiated by a population imbalance of  $n(0) = 357(35)$ . Here, the initial population imbalance does not change within the experimental error and the phase winds up. The solid lines correspond to the solution of the 3-D Gross-Pitaevskii equation with only independently measured parameters and also taking the time dependant position of the harmonic trap into account. However, for a quantitative agreement a  $40$ nm smaller jump of the harmonic trap is assumed, which is well within the experimental error of about  $80$ nm. The gray shaded area corresponds to the variation of the initial shift of the harmonic trap ( $\pm 40$ nm) and the variation of the total number of atoms ( $1000$  to  $1300$ ) within the experimentally expected range.

The filled circles show the data in the plasma oscillation regime and the open circles in the self trapping regime. The solid lines result from numerical simulations of the two mode model, where the time dependent shift of the harmonic trap is taken into account as well. For this the equation of motion in the case of an energy asymmetry (Eq. 5.4) are used with  $\Delta x(t) = \Delta x_0 \cdot \exp(-t/\tau_{\text{xdt}})$ . The gray shaded area corresponds to the experimental uncertainty and is calculated by using the same numerical integration for different initial population imbalances. In the Josephson regime the population imbalances are  $n(0) = 161 \pm 35$  and in the self trapping regime  $n(0) = 357 \pm 35$ .

To estimate the effect of the finite shifting time, we solve the equation of motion in the small amplitude limit and find for  $t \gg \tau_{\text{xdt}}$  that the temporal evolution of the population imbalance is governed by

$$n(t) = \frac{n(0)}{\sqrt{1 + \tau_{\text{xdt}}^2 \omega_p^2}} \times \cos(\omega_p t - \arctan(\omega_p \tau_{\text{xdt}})). \quad (5.7)$$

The oscillation amplitudes for our parameters are reduced due to this finite shifting time by

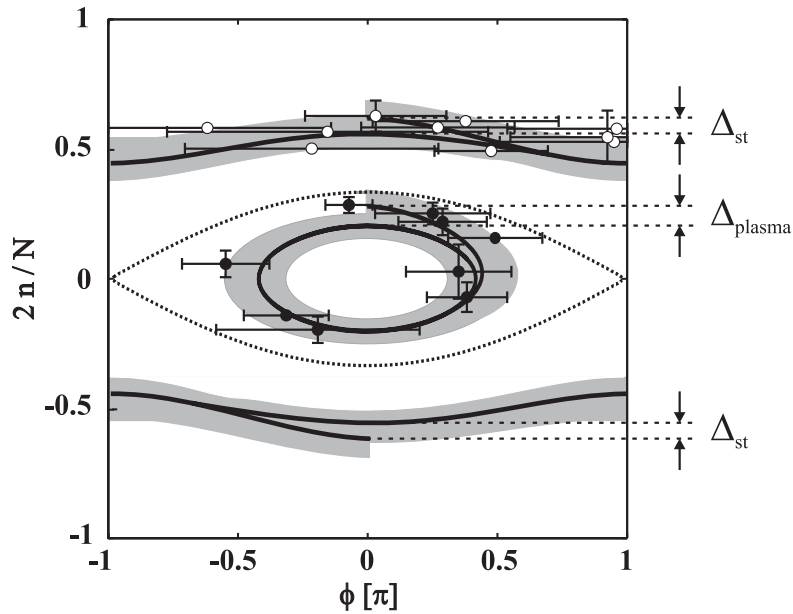


Figure 5.7: Phase plane diagram of the bosonic Josephson junction. In this graph the population imbalance is plotted versus the relative phase. The filled circles correspond to the measurement in the plasma oscillation regime and the open circles to the measurements in the self trapping regime. The two regimes are separated by the separatrix (dashed line). The solid lines depict the expected behavior of the dynamical variables based on the Gross-Pitaevskii two mode model, where also the time dependence of the shift of the harmonic trapping potential is taken into account. As the tunneling dynamics is already initiated during the shift of the energy-asymmetry, the oscillation amplitudes for longer times differ from the initial values, as indicated by  $\Delta_{plasma}$  and  $\Delta_{st}$ . The gray shaded area corresponds to the uncertainty of the initial parameters.

25% as indicated in Fig. 5.7 by  $\Delta_{plasma}$  and  $\Delta_{st}$ , leading to an effective critical population imbalance of  $n_c^{\text{eff}} = 238$  instead of  $n_c = 193$ . This can be understood by considering that already during the change of the position of the harmonic trap the tunneling dynamics is initiated and thus energy is taken out of the motion. Fig. 5.7 reveals that the dynamical response of the BJJ in the phase plane portrait is very well described by the two mode model.



---

## 6 Conclusions and Outlook

In the presented work, I have discussed the first successful experimental implementation of a single Josephson junction with Bose-Einstein condensates. For this, a double well potential is generated by the superposition of two independent trapping potentials, a 3-D harmonic potential for the overall confinement and a periodic potential with large periodicity acting as a barrier in the center. Both potentials are realized by the application of far red-detuned Gaussian laser beams. The Bose-Einstein condensates are usually consisting of a few thousand 87-Rubidium atoms. To prepare the bosonic Josephson junctions adiabatically a Bose-Einstein condensate is trapped in the 3-D harmonic trap and subsequently, the barrier is raised slowly in order to split it into two localized matter wave packets. If the barrier is not too high, particles can tunnel through the barrier on the timescale of the experiments leading to a coherent coupling of the two modes.

Within the mean field two-mode approximation, the behavior and the state of the Josephson junction can conveniently be described by two dynamical variables, the population imbalance, which is the atom number difference between the two matter wave packets, and the relative phase. We find that, in this picture, the equations of motion become analogous to the equations describing a single quantum mechanical particle in a sinusoidal potential. However, this simple model of the bosonic Josephson junction is only appropriate if the system is in the Rabi or the Josephson regime, i.e. the tunneling coupling of the two modes is strong enough to maintain a high coherence. In, or close to the Fock regime, where the system is dominated by atom number fluctuations, the coherence is low and a relative phase can not be defined. Thus, in the Fock regime the Josephson junction cannot be described by means of a mean field description.

### 6.1 Experimental results

The investigation of the steady state properties of the bosonic Josephson junction revealed that, at finite temperature, the two dynamical variables are not constant but fluctuate from measurement to measurement. The amount of fluctuations is directly connected to the temperature and the coupling constants. As, in the presented setup, the charging energy could only be changed slightly, the experimental investigation of the thermally induced fluctuations was focused on the properties of the relative phase. We found, that the fluctuations of the relative phase can be exactly predicted by a classical model, where the phases are populated according to the Boltzmann distribution. The amount of fluctuations depends only on a single scaling parameter, which is the ratio of the thermal energy scale to the tunneling coupling. For a quantitative comparison, not only the phase fluctuations but also the temperature and the tunneling coupling have to be known precisely. The temperature was deduced from independent time of flight measurement and the tunneling coupling was calculated numerically, using the first two mean field eigenstates of the Bose-Einstein condensate in the 3-D double

well potential. The agreement of coherence factor, which is a measure for the fluctuations in steady state, with the theoretical prediction was confirmed over a three orders of magnitude variation of the scaling parameter.

Due to the quantitative agreement between the theoretical prediction and the experimental findings, the measurement of the thermally induced fluctuations can be applied for measuring the temperature of a degenerate Bose gas at temperatures far below the critical temperature. This new method for thermometry is very useful, as the standard methods cannot be applied in a temperature range where the number of thermal particles is too small for detection. However, in the bosonic Josephson junction, it is always possible to tune the tunneling coupling, such that it is comparable to the thermal energy scale and thus, the relative phase is sensitive on thermally induced processes.

The application of the phase thermometer was demonstrated by measuring the heating up of a degenerate Bose gas in the 3-D harmonic trapping potential. For low temperatures, as long as matter wave interference patterns were observable, the temperature was deduced from the thermally induced fluctuations of the relative phase. For higher temperature, when the thermal distribution became observable in time of flight experiments, the temperature was also measured using the standard method. In the overlap region both methods lead to the same results confirming the applicability of the new thermometer. Furthermore, the non-linear temperature increase of the Bose gas could be consistently explained by a constant transfer rate of energy per particle, and a temperature dependent heat capacity. The deduced temperature dependence deviated from the prediction for an ideal Bose gas, which is expected theoretically, as the interatomic interactions modify the thermodynamic properties of the Bose gas slightly.

The experimental investigation of the dynamical response of the bosonic Josephson junction revealed, that for small atom number ranges at a precisely adjusted barrier height, both dynamical regimes, plasma oscillations and self trapping, are accessible in a fixed double well potential by initiating the dynamics at different population imbalances. For an initial population imbalance below the critical value for self trapping, the Josephson junctions showed oscillations of both dynamical variables with a zero mean value. When the initial population imbalance was raised above the critical value, the tunneling dynamics became suppressed and the population imbalance was approximately locked to a non-zero mean value. At the same time, the relative phase wound up at an approximately constant rate. The experimental observations were in excellent agreement with 3-D simulations of the temporal evolution of the wave function. However, the prediction of the two mode model could not predict the relevant tunneling time scale accurately. Nevertheless, the oscillation amplitudes of both variables were in excellent agreement and the phase plane portrait of the two mode model was consistent with the experimental findings.

## 6.2 Outlook

Since the investigations presented in this thesis were performed with the first realization of a Josephson junction with Bose-Einstein condensates, there are still many open questions, which should be tackled in the future.

In our experiments, it was difficult to manipulate the charging energy ( $E_c$ ). By improving the experimental setup and being able to change either the local densities by increasing the transverse confinement, or by accessing Feshbach resonances and tuning the interaction strength between the atoms, the charging energy could be varied over a wider range. With this, the thermally induced fluctuations of the atom number differences would also become

accessible and could be compared to the theoretical prediction [32]. The thermal uncertainty relation might be tested and the behavior of the Josephson junction in or close to the Fock regime investigated.

By tuning the quantum mechanical energy scale with respect to the thermal energy scale, it might also be possible to investigate the quantum mechanical fluctuations of the dynamical variables in steady state. The fundamental quantum mechanical uncertainty relation could be tested as a function of the ratio of the charging energy and the tunneling coupling. Furthermore, the investigation of the dynamical properties of the uncertainties should also lead to interesting observations. Effects like collapse and revival of the coherence are accessible, if the properties of the Josephson junction are changed rapidly, e.g. by decreasing or turning off the tunneling coupling.

Another interesting but experimentally difficult question is the possibility to observe  $\pi$ -oscillations in the bosonic Josephson junction [28]. These oscillations can be triggered by imprinting a phase difference close to  $\pi$ . Due to the nonlinearity for specific ratios of the charging energy to the tunneling coupling, a stable oscillation is initiated around a  $\pi$  mean value of the phase. However, these oscillations can only be accessed in a very narrow range and thus, a fine tuning of the parameters is inevitable.

Furthermore, finite temperature phenomena, which can already be observed experimentally but, due to the lack of a theoretical description, were not investigated in detail, are the damping of the Josephson dynamics and the thermally triggered decay of self trapped states. As the condensed particles collide with particles from higher excited states, energy might be transferred out of the coherent oscillations causing a heating of the ensemble. The damping rate as a function of the temperature, the tunneling coupling and the charging energy might lead to insight into the mechanism behind the damping and help building up a theoretical model to describe the process accurately.

The bosonic Josephson junction can also be used as discussed in [102] to generate a fan of dark solitons. For this, a Bose-Einstein condensate is split into two matter wave packets, which are strongly connected to each other such that the relative phase stays approximately zero and the fluctuations are small. By rapidly removing the barrier in the center, the two matter wave packets expand and interfere in the trap leading to the generation of wave packets with alternating phases. The zero crossing of the wave functions become stabilized due to the interaction of the particles and an array of dark solitons is formed. These, if prepared properly, oscillate back and forth within the trap. With this, it is also possible to generate only two dark solitons and study their collision and interaction.

A wide range of other theoretical questions might also be answered in the future by experiments with bosonic Josephson junctions. Small Bose-Einstein condensates in double well traps are even considered to test the validity of the mean field description, as for certain cases, not only one but two independent orbitals might become macroscopically populated leading to a fragmented state (see e.g. [30, 31, 103]). Thus, future experiments with weakly coupled Bose-Einstein condensates might help to gain more insight into quantum mechanical processes, as the observables can be accessed directly in this system and do not have to be measured via other indirect quantities. Furthermore, the interatomic interaction enriches the dynamical properties and leads to new phenomena, which are difficult to realize in other systems.



---

## A Heat Capacity close to the critical temperature

As discussed in Sec. 2.1.2, the heat capacity of the degenerate Bose gas in a 3-D harmonic trap below the critical temperature is given by

$$C(T < T_c) = N12k_B \frac{\zeta(4)}{\zeta(3)} \left(\frac{T}{T_c}\right)^3. \quad (\text{A.1})$$

To calculate the heat capacity in the high temperature limit the Bose-Einstein distribution can be approximated by the Boltzmann distribution leading to a heat capacity for temperatures above the critical temperature of

$$C(T > T_c) = 3Nk_B \left(1 + \frac{\zeta(3)}{8} \left(\frac{T_c}{T}\right)^3\right). \quad (\text{A.2})$$

The calculation of the heat capacity close to the critical temperature is more involved. The heat capacity at the transition is discontinuous as the chemical potential below  $T_c$  can be set to zero but above it is finite and below the ground state energy. The discontinuity can for an ideal Bose gas be expressed as

$$\Delta C = C(T_{c+}) - C(T_{c-}) = 3N \frac{\partial \mu}{\partial T}_{T=T_{c+}} = -9 \frac{\zeta(3)}{\zeta(2)} Nk_B. \quad (\text{A.3})$$

For more details on the heat capacity of ultracold and degenerate gases we refer to [50] or [54].

---

## B Numerical solution of the Gross-Pitaevskii equation in 3-D

The prediction of the properties of the bosonic Josephson junction and also the calculation of the temporal evolution of the dynamical variables rely on the precise knowledge of the system parameters  $E_c$  (Eq. 2.43) and  $E_j$  (Eq. 2.44) (and also the energy asymmetry  $\delta$  Eq. 4.3). If the parameters of the potential and the atom numbers are known, the 3-D Gross-Pitaevskii equation (Eq. 2.5) can be used to find the single particle mean field eigenstates which are needed for the calculation of the system parameters.

Furthermore, by using the GPE for the temporal evolution of the wave functions, it is not necessary to restrict the number of the allowed states to two, but all higher excited states up to the numerical resolution are taken into account. This is only accurate, if the BJJ is in the Josephson regime and thus the fluctuations of the dynamical variables are negligible. Usually, higher excited states in the double well potential are not playing a role, but transverse excitations can affect the dynamics. Thus, to compare the different models, we implemented two numeric algorithm in order to calculate the temporal evolution and to calculate the eigenstates of arbitrary potential in 3-D.

The temporal evolution of the 3-D Gross-Pitaevskii equation is calculated efficiently with a split-step method [104]. The main idea is that the Laplace operator acting on a 3-D field can be much faster calculated in momentum space than in real space. Thus, as only small time steps are considered, the time propagation is split into a spatial part, consisting of the potential and the interaction term, and a momentum space part, consisting of the kinetic term

$$\begin{aligned}
\Psi(\mathbf{r}; t + \Delta t) &= \hat{U}(\Delta t)\Psi(\mathbf{r}; t) = e^{-\frac{i\hat{H}(\mathbf{r};t)\Delta t}{\hbar}}\Psi(\mathbf{r}; t) \\
&= e^{\frac{i\hbar\nabla^2\Delta t}{2m}} e^{-\frac{iV_{\text{ext}}(\mathbf{r};t)+gN|\Psi(\mathbf{r};t)|^2\Delta t}{\hbar}}\Psi(\mathbf{r}; t) \\
&= e^{\frac{i\hbar\nabla^2\Delta t}{2m}}\Psi'(\mathbf{r}; t) \\
&= e^{\frac{i\hbar\mathbf{k}^2\Delta t}{2m}}\tilde{\Psi}'(\mathbf{k}; t), \tag{B.1}
\end{aligned}$$

where  $\Psi'(\mathbf{r}; t)$  denotes the wave function, which was partially propagated in real space and  $\tilde{\Psi}'(\mathbf{k}; t)$  to the Fourier transform of this wave function. To minimize the numerical errors due to the finite time steps  $\Delta t$ , the propagation in momentum space is split into two half steps  $\Delta t/2$  and applied to the wave function before and after the propagation in real space. This method can be used for time steps fulfilling  $\langle\Psi|\hat{H}|\Psi\rangle\Delta t \ll 2\pi$ .

By slightly modifying the former algorithm, it becomes also possible to find the stationary states of the external potential. The propagation in this case is performed in imaginary time. The effect of the propagation in imaginary time can be directly seen, if the time propagation operator is written in the diagonal basis  $\Psi(\mathbf{r}) = \sum_d \psi_d \Phi_d(\mathbf{r})$  and the ground state energy  $E_0$

---

is set as the reference energy

$$\begin{aligned}
\hat{U}(-i\Delta t)\Psi(\mathbf{r}) &= e^{-\frac{(\hat{H}-E_0)\Delta t}{\hbar}}\Psi(\mathbf{r}) \\
&= \sum_d e^{-\frac{(\hat{H}-E_0)\Delta t}{\hbar}}\psi_d\Phi_d(\mathbf{r}) \\
&= \sum_d e^{-\frac{(E_d-E_0)\Delta t}{\hbar}}\psi_d\Phi_d(\mathbf{r}) \\
&= \psi_0\Phi_0(\mathbf{r}) + e^{-\frac{(E_1-E_0)\Delta t}{\hbar}}\psi_1\Phi_1(\mathbf{r}) + e^{-\frac{(E_2-E_0)\Delta t}{\hbar}}\psi_2\Phi_2(\mathbf{r}) + \dots \quad (\text{B.2})
\end{aligned}$$

Due to the exponential dependence, the wave functions are damped according to their energies. Thus, the states with low energy are damped less than the states with higher energy and after long propagation times only the states with the lowest energy can survive.

This method has a difficulty to distinguish between two states which are quasi degenerate, and the propagation has to be done for very long times in order to damp out the slightly higher lying states. In the case of the double well potential, the energy of the ground state and the energy of the first excited state are close. However, by choosing the trial wave function properly, the two eigenstates can be calculated without extra effort. This is possible, as the propagation conserves the symmetry of the trial wave function and by choosing it to be symmetric we find the ground state, by choosing it to be antisymmetric we find the first excited state.

In order to increase the spatial resolution and to reduce the time for simulations in certain cases the 3-D GPE can be approximated by the non-polynomial Schrödinger equation (NPSE) [105]. Here, the wave functions are assumed to be cylindrically symmetric and have a Gaussian profile transversally. In this case, it is possible to analytically integrate out the transverse degrees of freedom. The transverse width of the wave function at every point can then be calculated from the local density and the interaction strength. With this the 3-D GPE is reduced to a more complicated 1-D Schrödinger equation, which can be solved faster with higher spatial resolution. The NPSE has the form

$$\begin{aligned}
i\hbar\frac{\partial}{\partial t}f(x) &= \left[ -\frac{\hbar^2}{2m}\frac{\partial^2}{\partial x^2} + V(z) + \frac{gNm\omega_{y,z}}{2\pi\hbar}\frac{|f(x)|^2}{\sqrt{1+2aN|f(x)|^2}} \right. \\
&\quad \left. + \frac{\hbar\omega_{y,z}}{2}\left(\frac{1}{\sqrt{1+2aN|f(x)|^2}} + \sqrt{1+2aN|f(x)|^2}\right) \right]f(x), \quad (\text{B.3})
\end{aligned}$$

where the wave function is defined as  $\Psi(x, y, z; t) = \psi(y, z; t) \times f(x; t)$ , the potential  $V(x, y, z; t) = V(x; t) \times V(y, z; t)$  and  $a$  is the s-wave scattering length. The transverse width is given by  $\sigma_{y,z;t} = (\hbar/m\omega_{y,z})\sqrt{1+2aN|f(x)|^2}$ . This formalism can be applied for elongated, cigar-shaped BEC if the transverse dynamics is negligible.

---

## C Tunneling coupling and on-site interaction energy deduced from 3-D GPE

For the experimental investigation of thermally induced fluctuations (Sec. 4.2.3) a large number of measurements at different atom numbers and barrier heights were performed. In order to compare the measurements with the theoretical prediction the system parameters  $E_j$  and  $E_c$  have to be known. These coupling constants can be calculated numerically by Eq. 2.43 and Eq. 2.44 if the ground state and the first excited state wave function are known. With the method discussed in Appendix B, we can calculate the first two eigenstates of the particles in the double well trap for different atom numbers and barrier heights. The resulting  $E_c(V_0, N)$  and  $E_j(V_0, N)$  are fitted with the functional dependence shown below

$$E_j(V_0, N) = 10^{a_j(N) \cdot V_0^3 + b_j(N) \cdot V_0^2 + c_j(N) \cdot V_0 + d_j(N)} \quad (\text{C.1})$$

$$\begin{aligned} a_j(N) &= -1.370 \times 10^{-8} \cdot N^{-0.2037} + 3.226 \times 10^{-9} \\ b_j(N) &= -1.157 \times 10^{-7} \cdot N^{0.4719} + 3.527 \times 10^{-6} \\ c_j(N) &= 8.734 \times 10^{-4} \cdot N^{0.3060} - 1.142 \times 10^{-2} \\ d_j(N) &= -2.307 \times 10^{-3} \cdot N^{0.6696} + 4.407, \end{aligned} \quad (\text{C.2})$$

and

$$E_c(V_0, N) = a_c(N) \cdot V_0^2 + b_c(N) \cdot V_0 + c_c(N) \quad (\text{C.3})$$

$$\begin{aligned} a_c(N) &= -2.955 \times 10^{-7} \cdot N^{-0.6235} \\ b_c(N) &= 6.581 \times 10^{-4} \cdot N^{-0.5542} \\ c_c(N) &= 5.628 \times 10^{-1} \cdot N^{-0.5042}. \end{aligned} \quad (\text{C.4})$$

The fitting functions are validity in the atom number range of  $2000 < N < 3500$  and in the range of the barrier heights of  $500\text{Hz} < V_0/h < 1600\text{Hz}$ . The lattice spacing is set to  $d_{\text{sw}} = 4.8\mu\text{m}$  and the trapping frequencies of the harmonic trap are  $\omega_x = 2\pi \times 90\text{Hz}$  and  $\omega_{y,z} = 2\pi \times 100\text{Hz}$ . The errors of both fits ( $E_c(V_0, N)$  and  $E_j(V_0, N)$ ) are on the order of a few percent.

## D Rubidium-87

Alkali atoms are commonly used for laser cooling and magnetic trapping because of their relatively simple hydrogen-like term scheme and advantageous properties. Especially Rubidium has earned itself a reputation as a workhorse for BEC experiments, because it is relatively easy to handle. Its relevant transitions are located around 780nm, which can be accessed by commercial diode and Titanium-Sapphire laser systems. Due to its high vapor pressure at room temperature, Rubidium can be generated efficiently in the gas phase.

The two most abundant isotopes of Rubidium in nature are  $^{85}_{37}\text{Rb}$  with 72% and  $^{87}_{37}\text{Rb}$  with 28%. In our experiment,  $^{87}_{37}\text{Rb}$  is used because  $^{85}_{37}\text{Rb}$  has a negative scattering length at magnetic field strengths common for magnetic trapping and  $^{87}_{37}\text{Rb}$  has favorable collision parameters.  $^{87}_{37}\text{Rb}$  is radioactive but stable on the usual timescale of the experiment. It decays by a  $\beta^-$ -transition into  $^{87}_{38}\text{Sr}$ , with a lifetime of  $4.88 \cdot 10^{10}$  years [106]. 32 other isotopes are known, the most stable isotopes are  $^{83}_{37}\text{Rb}$  ( $\tau = 86.2\text{days}$ ),  $^{84}_{37}\text{Rb}$  ( $\tau = 32.77\text{days}$ ) and  $^{86}_{37}\text{Rb}$  ( $\tau = 18.631\text{days}$ ).

Some physical properties of  $^{87}_{37}\text{Rb}$  are shown below

Mass	m	86.909 180 520(15) $1.443 160 60(11) \times 10^{-25}$	u kg
Melting point at 1013mbar	$T_M$	39.31	$^{\circ}\text{C}$
Boiling point at 1013mbar	$T_B$	688	$^{\circ}\text{C}$
vapor pressure at $25^{\circ}\text{C}$	$P_V$	$4 \times 10^{-7}$	mbar
<b>D<sub>2</sub>-line</b>		$5^2\text{S}_{1/2} \rightarrow 5^2\text{P}_{3/2}$	
Wavelength (vacuum)	$\lambda$	780.246 291 692(11)	nm
Wavelength (air)	$\lambda_{\text{air}}$	780.037 08	nm
Frequency	$\omega_0$	$2\pi \cdot 384.2279818773(55)$	THz
Lifetime $5^2\text{P}_{3/2}$	$\tau$	26.24(4)	ns
Linewidth (FWHM)	$\Gamma$	$2\pi \cdot 6.065(9)$	MHz
Saturation intensity	$I_{\text{sat}}$	1.67	mW/cm <sup>2</sup>
Recoil temperature at 780nm	$T_{\text{rec}}$	$(\hbar k)^2/mk_B = 361.95$	nK
Recoil velocity at 780nm	$v_{\text{rec}}$	$\hbar k/m = 5.8845$	mm/s

For more details on 87-Rubidium we refer to [107, 108]. Fig. D.1 shows the hyperfine structure of the  $D_2$ -line of  $^{87}\text{Rb}$ . The wavelengths to which the four laser systems are locked, are indicated by the arrows in the center. The spectroscopic details of the  $D_2$ -line can be found in [109].

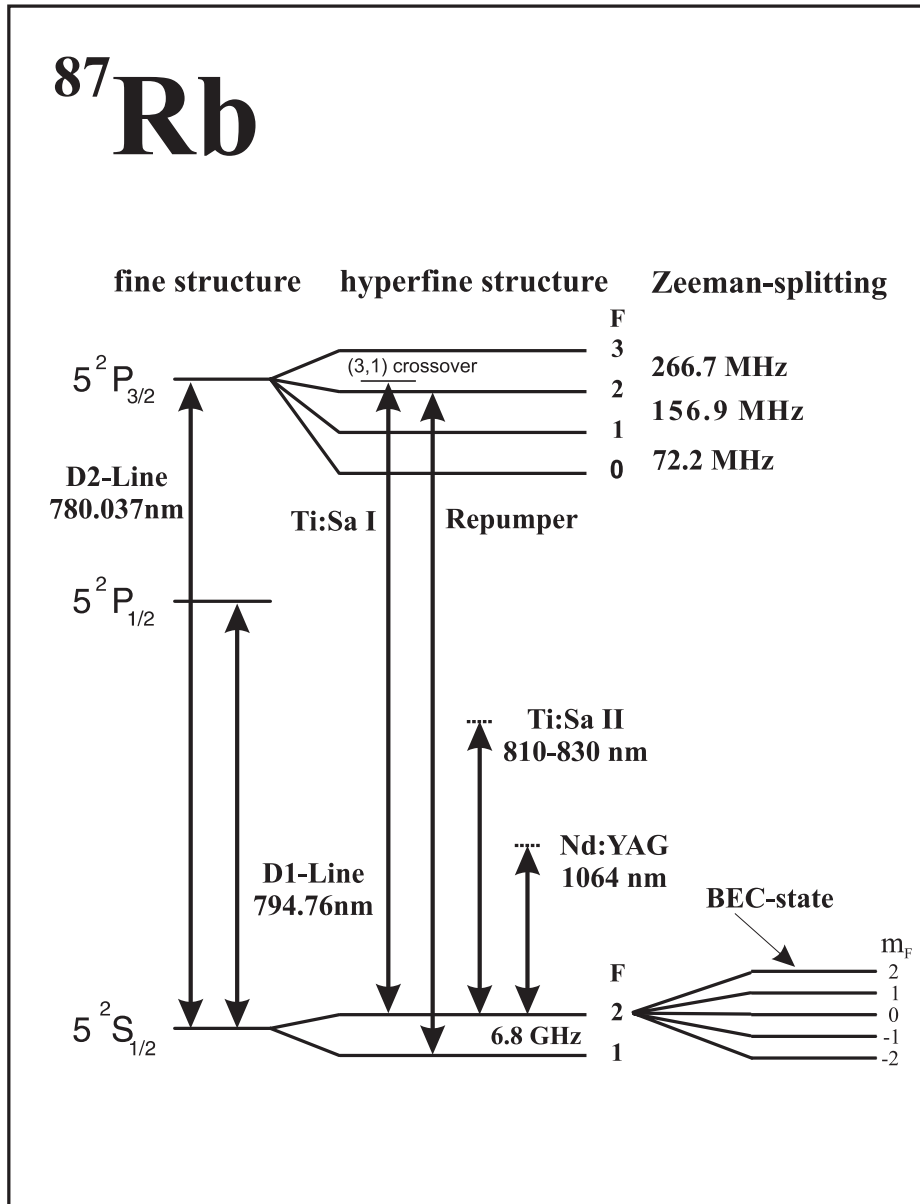


Figure D.1: Hyperfine levels of <sup>87</sup>Rubidium and the D<sub>1</sub>- and D<sub>2</sub>-line. The arrows in the center correspond to the wavelengths to which the four laser systems are adjusted and the transitions they are driving. The Bose-Einstein condensate is prepared in the  $F = 2, m_F = 2$  state. The funnel and the MOT - transitions are to the  $F = 3, m_F = 3$  state, and also the optical pumping and the imaging is done by coupling to this state (Ti:Sa I). During the funnel and the MOT cycle atoms can fall to the  $F = 1$  level, from where they are transferred back into the cycle by the Repumper. The crossed dipole trap (Nd:YAG) and the standing light wave (Ti:Sa II) are far red-detuned with respect to the transitions and lead to dipole potentials only, where the spontaneous scattering rate can be neglected on the timescale of the experiments.

---

## Bibliography

- [1] L. de Broglie. Recherches sur la théorie des quanta. PhD Thesis, Paris, 1924.
- [2] C. Davisson and L. H. Germer. Diffraction of Electrons by a Crystal of Nickel. *Phys. Rev.*, **30**(6):705, 1927.
- [3] O. Carnal and J. Mlynek. Young's double-slit experiment with atoms: A simple atom interferometer. *Phys. Rev. Lett.*, **66**(21):2689, 1991.
- [4] D. W. Keith, Ch. R. Ekstrom, Q. A. Turchette, and D. E. Pritchard. An interferometer for atoms. *Phys. Rev. Lett.*, **66**(21):2693, 1991.
- [5] F. Riehle, Th. Kisters, A. Witte, J. Helmcke, and Ch. J. Bordé. Optical Ramsey spectroscopy in a rotating frame: Sagnac effect in a matter-wave interferometer. *Phys. Rev. Lett.*, **67**(2):177, 1991.
- [6] M. Kasevich and S. Chu. Atomic interferometry using stimulated Raman transitions. *Phys. Rev. Lett.*, **67**(2):181, 1991.
- [7] A. Einstein. Quantentheorie des einatomigen idealen Gases. *Sitzungsber. Preuss. Akad. Wiss.*, page 261, 1924.
- [8] S. N. Bose. Plancks Gesetz und Lichtquantenhypothese. *Z.Phys.*, **26**(6):178, 1924.
- [9] M. Anderson, J. Ensher, M. Matthews, C. Wieman, and E. Cornell. Observation of Bose-Einstein condensation in a dilute atomic vapor. *Science*, **269**:198, 1995.
- [10] K. Davis, M.-O. Mewes, M. Andrews, N. van Druten, N. Durfee, D. Kurn, and W. Ketterle. Bose-Einstein condensation in a gas of Sodium atoms. *Phys. Rev. Lett.*, **75**(22):3969, 1995.
- [11] C. C. Bradley, C. A. Sackett, J. J. Tollet, and R. G. Hulet. Evidence of Bose-Einstein condensation in an atomic gas with attractive interactions. *Phys. Rev. Lett.*, **75**(9):1687, 1995.
- [12] M. R. Andrews, C. G. Townsend, H.-J. Miesner, D. S. Durfee, D. M. Kurn, and W. Ketterle. Observation of Interference Between Two Bose Condensates. *Science*, **275**:637, 1997.
- [13] B. D. Josephson. Possible new effects in superconducting tunneling. *Phys. Lett.*, **1**:251, 1962.
- [14] P. W. Anderson and J. M. Rowell. Probable Observation of the Josephson Superconducting Tunneling Effect. *Phys. Rev. Lett.*, **10**(6):230, 1963.
- [15] K. K. Likharev. Superconducting weak links. *Rev. Mod. Phys.*, **51**(1):101, 1979.
- [16] A. Barone and G. Paterno. Physics and applications of the Josephson effect. Wiley, New York, 1982.
- [17] S. Pereverzev, A. Loshak, S. Backhaus, J. C. Davis, and R. E. Packard. Quantum oscillations between two weakly coupled reservoirs of superfluid  $^3\text{He}$ . *Nature*, **388**:449, 1997.
- [18] S. Backhaus, S. Pereverzev, A. Loshak, J. C. Davis, and R. E. Packard. Direct measurement of the Current-Phase relation of a Superfluid  $^3\text{He}$ -B weak link. *Science*, **278**:1435, 1997.
- [19] J. C. Davis and R. E. Packard. Superfluid  $^3\text{He}$  Josephson weak links. *Rev. Mod. Phys.*, **74**(3):741, 2002.

- [20] K. Sukhatme, Y. Mukharsky, T. Chui, and D. Pearson. Observation of the ideal Josephson effect in superfluid  $^4\text{He}$ . *Nature*, **411**:280, 2001.
- [21] J. Javanainen. Oscillatory exchange of atoms between traps containing Bose condensates. *Phys. Rev. Lett.*, **57**(25):3164, 1986.
- [22] O. Morsch and M. K. Oberthaler. Dynamics of Bose-Einstein condensates in optical lattices. *Rev. Mod. Phys.*, **78**(1):179, 2006.
- [23] A. Imamoglu, M. Lewenstein, and L. You. Inhibition of Coherence in Trapped Bose-Einstein Condensates. *Phys. Rev. Lett.*, **78**(13):2511, 1997.
- [24] D. Ananikian and T. Bergeman. Gross-Pitaevskii equation for Bose particles in a double-well potential: Two-mode models and beyond. *Phys. Rev. A*, **73**(1):013604, 2006.
- [25] G. J. Milburn, J. Corney, E. M. Wright, and D. F. Walls. Quantum dynamics of an atomic Bose-Einstein condensate in a double-well potential. *Phys. Rev. A*, **55**(6):4318, 1997.
- [26] A. Smerzi, S. Fantoni, S. Giovanazzi, and S. R. Shenoy. Quantum Coherent Atomic Tunneling between Two Trapped Bose-Einstein Condensates. *Phys. Rev. Lett.*, **79**(25):4950, 1997.
- [27] I. Zapata, F. Sols, and A. J. Leggett. Josephson effect between trapped Bose-Einstein condensates. *Phys. Rev. A*, **57**(1):R28, 1998.
- [28] S. Raghavan, A. Smerzi, S. Fantoni, and S. R. Shenoy. Coherent oscillations between two weakly coupled Bose-Einstein condensates: Josephson effects,  $\pi$  oscillations, and macroscopic quantum self-trapping. *Phys. Rev. A*, **59**(1):620, 1999.
- [29] P. Nozières. Bose-Einstein condensateion. Edited by A. Griffin, D. W. Snoke, and S. Stringari, Cambridge University Press, Cambridge, England, 1982.
- [30] R. W. Spekkens and J. E. Sipe. Spatial fragmentation of a Bose-Einstein condensate in a double-well potential. *Phys. Rev. A*, **59**(5):3868, 1999.
- [31] E. J. Mueller, T.-L. Ho, M. Ueda, and G. Baym. Fragmentation of Bose-Einstein condensates. *Phys. Rev. A*, **74**(3):033612, 2006.
- [32] L. Pitaevskii and S. Stringari. Thermal vs Quantum Decoherence in Double Well Trapped Bose-Einstein Condensates. *Phys. Rev. Lett.*, **87**(18):180402, 2001.
- [33] Gh.-S. Paraoanu, S. Kohler, F. Sols, and A. J. Leggett. The Josephson plasmon as a Bogoliubov quasiparticle. *At. Mol. Opt. Phys.*, **34**:4689, 2001.
- [34] E. M. Wright, D. F. Walls, and J. C. Garrison. Collapses and Revivals of Bose-Einstein Condensates Formed in Small Atomic Samples. *Phys. Rev. Lett.*, **77**(11):2158, 1996.
- [35] J. Javanainen and M. Wilkens. Phase and Phase Diffusion of a Split Bose-Einstein Condensate. *Phys. Rev. Lett.*, **78**(25):4675, 1997.
- [36] J. Javanainen and M. Yu. Ivanov. Splitting a trap containing a Bose-Einstein condensate: Atom number fluctuations. *Phys. Rev. A*, **60**(3):2351, 1999.
- [37] F. S. Cataliotti, S. Burger, C. Fort, P. Maddaloni, F. Minardi, A. Trombettoni, A. Smerzi, and M. Inguscio. Josephson Junction Arrays with Bose-Einstein Condensates. *Science*, **293**:843, 2001.
- [38] Th. Anker, M. Albiez, R. Gati, S. Hunsmann, B. Eiermann, A. Trombettoni, and M. K. Oberthaler. Nonlinear Self-Trapping of Matter Waves in Periodic Potentials. *Phys. Rev. Lett.*, **94**(2):020403, 2005.
- [39] S. Hofferberth, I. Lesanovsky, B. Fischer, J. Verdu, and J. Schmiedmayer. Radiofrequency-dressed-state potentials for neutral atoms. *Nat. Phys.*, **2**:710, 2006.

- 
- [40] T. Schumm, S. Hofferberth, L. M. Andersson, S. Wildermuth, S. Groth, I. Bar-Joseph, J. Schmiedmayer, and P. Krüger. Matter-wave interferometry in a double well on an atom chip. *Nat. Phys.*, **1**:57, 2005.
- [41] Y. Shin, G.-B. Jo, M. Saba, T. A. Pasquini, W. Ketterle, and D. E. Pritchard. Optical Weak Link between Two Spatially Separated Bose-Einstein Condensates. *Phys. Rev. Lett.*, **95**(17):170402, 2005.
- [42] J. Williams, R. Walser, J. Cooper, E. Cornell, and M. Holland. Nonlinear Josephson-type oscillations of a driven, two-component Bose-Einstein condensate. *Phys. Rev. A*, **59**(1):R31, 1999.
- [43] P. Öhberg and S. Stenholm. Internal Josephson effect in trapped double condensates. *Phys. Rev. A*, **59**(5):3890, 1999.
- [44] Gh.-S. Paraoanu, M. Rodriguez, and P. Törmä. Josephson effect in superfluid atomic Fermi gases. *Phys. Rev. A*, **66**(4):041603, 2002.
- [45] V. M. Galitski. Internal Josephson effect in a Fermi gas near a Feshbach resonance. *Phys. Rev. A*, **72**(1):013612, 2005.
- [46] M. Albiez, R. Gati, J. Fölling, S. Hunsmann, M. Cristiani, and M. K. Oberthaler. Direct Observation of Tunneling and Nonlinear Self-Trapping in a Single Bosonic Josephson Junction. *Phys. Rev. Lett.*, **95**(1):010402, 2005.
- [47] R. Gati, M. Albiez, J. Fölling, B. Hemmerling, and M. K. Oberthaler. Realization of a single Josephson junction for Bose-Einstein condensates. *Appl. Phys. B*, **82**:207, 2006.
- [48] R. Gati, B. Hemmerling, J. Fölling, M. Albiez, and M. K. Oberthaler. Noise Thermometry with Two Weakly Coupled Bose-Einstein Condensates. *Phys. Rev. Lett.*, **96**(13):130404, 2006.
- [49] R. Gati, J. Esteve, B. Hemmerling, T. B. Ottenstein, J. Appmeier, A. Weller, and M. K. Oberthaler. A primary noise thermometer for ultracold Bose gases. *N. J. Phys.*, **8**:189, 2006.
- [50] F. Schwabel. *Statistische Mechanik*. Springer, 2000.
- [51] A. Griesmaier, J. Werner, S. Hensler, J. Stuhler, and T. Pfau. Bose-Einstein Condensation of Chromium. *Phys. Rev. Lett.*, **94**(16):160401, 2005.
- [52] O. Penrose and L. Onsager. Bose-Einstein Condensation and Liquid Helium. *Phys. Rev.*, **104**(3):576, 1956.
- [53] L. Pitaevskii and S. Stringari. *Bose-Einstein condensation*. Clarendon Press, Oxford, 2003.
- [54] C. J. Pethick and H. Smith. *Bose-Einstein condensation in dilute Bose gases*. Cambridge University Press, 2002.
- [55] F. Dalfovo and S. Stringari. Bosons in anisotropic traps: Ground state and vortices. *Phys. Rev. A*, **53**(4):2477, 1996.
- [56] P. C. Hohenberg. Existence of Long-Range Order in One and Two Dimensions. *Phys. Rev.*, **158**(2):383, 1967.
- [57] Z. Hadzibabic, P. Krüger, M. Cheneau, B. Battelier, and J. Dalibard. Berezinskii-Kosterlitz-Thouless crossover in a trapped atomic gas. *Nature*, **441**:1118, 2006.
- [58] D. S. Petrov, M. Holzmann, and G. V. Shlyapnikov. Bose-Einstein Condensation in Quasi-2D Trapped Gases. *Phys. Rev. Lett.*, **84**(12):2551, 2000.
- [59] Y. Castin and R. Dum. Bose-Einstein Condensates in Time Dependent Traps. *Phys. Rev. Lett.*, **77**(27):5315, 1996.
- [60] Y. Kagan, E. L. Surkov, and G. V. Shlyapnikov. Evolution of a Bose-condensed gas under variations of the confining potential. *Phys. Rev. A*, **54**(3):R1753, 1996.

- [61] F. Dalfovo, S. Giorgini, L. P. Pitaevskii, and S. Stringari. Theory of Bose-Einstein condensation in trapped gases. *Rev. Mod. Phys.*, **71**(3):463, 1999.
- [62] L. You and M. Holland. Ballistic expansion of trapped thermal atoms. *Phys. Rev. A*, **53**(1):R1, 1996.
- [63] A. I. Streltsov, O. E. Alon, and L. S. Cederbaum. General variational many-body theory with complete self-consistency for trapped bosonic systems. *Phys. Rev. A*, **73**(6):063626, 2006.
- [64] D. Masiello, S. B. McKagan, and W. P. Reinhardt. Multiconfigurational Hartree-Fock theory for identical Bosons in a double well. *Phys. Rev. A*, **72**(6):063624, 2005.
- [65] J. I. Cirac, M. Lewenstein, K. Mølmer, and P. Zoller. Quantum superposition states of Bose-Einstein condensates. *Phys. Rev. A*, **57**(2):1208, 1998.
- [66] M. J. Steel and M. J. Collett. Quantum state of two trapped Bose-Einstein condensates with a Josephson coupling. *Phys. Rev. A*, **57**(4):2920, 1998.
- [67] J. A. Dunningham, K. Burnett, and M. Edwards. *Phys. Rev. A*, **64**(1):015601, 2001.
- [68] K. W. Mahmud, H. Perry, and W. P. Reinhardt. Phase engineering of controlled entangled number states in a single component Bose-Einstein condensate in a double well. *J. Phys. B*, **36**:265, 2003.
- [69] A. I. Streltsov, L. S. Cederbaum, and N. Moiseyev. Ground-state fragmentation of repulsive Bose-Einstein condensates in double-trap potentials. *Phys. Rev. A*, **70**(5):053607, 2004.
- [70] W.-M. Zhang, D. H. Feng, and R. Gilmore. Coherent states: Theory and some applications. *Rev. Mod. Phys.*, **62**(4):867, 1990.
- [71] L. Amico and V. Penna. Dynamical Mean Field Theory of the Bose-Hubbard Model. *Phys. Rev. Lett.*, **80**(10):2189, 1998.
- [72] P. Buonsante, V. Penna, and A. Vezzani. Attractive ultracold Bosons in a necklace optical lattice. *Phys. Rev. A*, **72**(4):043620, 2005.
- [73] A. J. Leggett. Bose-Einstein condensation in the alkali gases: Some fundamental concepts. *Rev. Mod. Phys.*, **73**(2):307, 2001.
- [74] P. A. M. Dirac. The quantum theory of the emission and absorption of radiation. *Proc. R. Soc. London, Ser. A*, **114**:243, 1927.
- [75] L. Susskind and J. Gloglower. Quantum mechanical phase and time operator. *Physics*, **1**:49, 1964.
- [76] E. C. Lerner. Harmonic oscillator phase operators. *Nuovo Cimento B*, **56**:183(L), 1968.
- [77] S. M. Barnett and D. T. Pegg. Phase in quantum optics. *J. Phys. A*, **19**:3849, 1986.
- [78] D. T. Pegg and S. M. Barnett. Phase properties of the quantized single-mode electromagnetic field. *Phys. Rev. A*, **39**(4):1665, 1989.
- [79] S. M. Barnett and D. T. Pegg. On the Hermitian optical phase operator. *J. Mod. Phys.*, **36**(1):7, 1989.
- [80] Y. Castin and J. Dalibard. Relative phase of two Bose-Einstein condensates. *Phys. Rev. A*, **55**(6):4330, 1997.
- [81] W. J. Mullin, R. Krotkov, and F. Laloe. The origin of the phase in the interference of Bose-Einstein condensates. *American Journal of Physics*, **74**(10):880, 2006.
- [82] B. Eiermann. Kohärente nichtlineare Materiewellendynamik - Helle atomare Solitonen. PhD Thesis, Universität Konstanz, 2004.
- [83] M. Albiez. Observation of nonlinear tunneling of a Bose-Einstein condensate in a single Josephson junction. PhD Thesis, Universität Heidelberg, 2005.

- 
- [84] J. Fölling. Bose-Einstein Josephson Tunnelling and Generation of Arbitrary Optical Potentials. Diploma Thesis, Universität Heidelberg, 2005.
- [85] B. Hemmerling. Thermally induced fluctuations in a bosonic Josephson junction. Diploma Thesis, Universität Heidelberg, 2006.
- [86] C. Cohen-Tannoudji, J. Dupont-Roc, and G. Grynberg. Atom-Photon Interactions. Wiley, New York, 1992.
- [87] H.J. Metcalf and P. van der Straten. Laser Cooling and Trapping. Springer Verlag, 1999.
- [88] W. Ketterle, D.S. Durfee, and D.M. Stamper-Kurn. Making, probing and understanding Bose-Einstein condensates. In M. Inguscio, S. Stringari, and C. Wieman, editors, *Bose-Einstein Condensation in Atomic Gases*, Amsterdam: IOS Press, 1999. Società Italiana di Fisica.
- [89] M. Greiner, O. Mandel, T. Esslinger, T. W. Hänsch, and I. Bloch. Quantum phase transition from superfluid to a Mott insulator in a gas of ultracold atoms. *Nature*, **415**:39, 2002.
- [90] V. Ambegaokar and A. Baratoff. Tunneling Between Superconductors. *Phys. Rev. Lett.*, **10**(11):486, 1963.
- [91] S. R. De Groot, G. J. Hooyman, and C. A. ten Seldam. On the Bose-Einstein condensation. *Proc. Roy. Soc. Lond. A*, **203**:266, 1950.
- [92] T. A. Savard, K. M. O'Hara, and J. E. Thomas. Laser-noise-induced heating in far-off resonance optical traps. *Phys. Rev. A*, **56**(2):R1095, 1997.
- [93] J. R. Ensher, D. S. Jin, M. R. Matthews, C. E. Wieman, and E. A. Cornell. Bose-Einstein Condensation in a Dilute Gas: Measurement of Energy and Ground-State Occupation. *Phys. Rev. Lett.*, **77**(25):4984, 1996.
- [94] A. Minguzzi, S. Conti, and M. P. Tosi. The internal energy and condensate fraction of a trapped interacting Bose gas. *Journal of Physics: Condensed Matter*, **9**(5):L33, 1997.
- [95] R. P. Feynman, R. B. Leighton, and M. Sands. The Feynman Lectures on Physics Vol. 1. Addison-Wesley, Reading, MA, 1963.
- [96] M. W. Jack, M. J. Collett, and D. F. Walls. Coherent quantum tunneling between two Bose-Einstein condensates. *Phys. Rev. A*, **54**(6):R4625, 1996.
- [97] J. Ruostekoski and D. F. Walls. Bose-Einstein condensate in a double-well potential as an open quantum system. *Phys. Rev. A*, **58**(1):R50, 1998.
- [98] K. W. Mahmud, H. Perry, and W. P. Reinhardt. Quantum phase-space picture of Bose-Einstein condensates in a double well. *Phys. Rev. A*, **71**(2):023615, 2005.
- [99] E. A. Ostrovskaia, Y. S. Kivshar, M. Lisak, B. Hall, F. Cattani, and D. Anderson. Coupled-mode theory for Bose-Einstein condensates. *Phys. Rev. A*, **61**(3):031601, 2000.
- [100] S. Giovanazzi, A. Smerzi, and S. Fantoni. Josephson Effects in Dilute Bose-Einstein Condensates. *Phys. Rev. Lett.*, **84**(20):4521, 2000.
- [101] J. R. Anglin, P. Drummond, and A. Smerzi. Exact quantum phase model for mesoscopic Josephson junctions. *Phys. Rev. A*, **64**(6):063605, 2001.
- [102] T. Ottenstein. New objective for high resolution imaging of Bose-Einstein condensates. Diploma Thesis, Universität Heidelberg, 2006.
- [103] A. I. Streltsov and L. S. Cederbaum. Properties of fragmented repulsive condensates. *Phys. Rev. A*, **71**(6):063612, 2005.
- [104] P. L. DeVries. Application of the Split Operator Fourier Transform Method to the Solution of the Nonlinear Schrödinger Equation. *AIP Conference Proceedings*, **160**:269, 1986.

- [105] L. Salasnich, A. Parola, and L. Reatto. Effective wave equations for the dynamics of cigar-shaped and disk-shaped Bose condensates. *Phys. Rev. A*, **65**(4):043614, 2002.
- [106] D. R. Lide. CRC handbook of chemistry and physics. CRCnetBase, 1999.
- [107] D. A. Steck. Rubidium 87 D-line data. <http://steck.us/alkalidata>, 2003.
- [108] A. A. Radzig and B. M. Smirnov. Reference data on atoms, molecules and ions. Springer Verlag, Berlin, 1985.
- [109] S. Kraft, A. Deninger, Ch. Trück, J. Fortagh, F. Lison, and C. Zimmermann. Rubidium spectroscopy at 778-780nm with a distributed feedback laser diode. *Laser Phys. Lett.*, **2**(2):71, 2004.

---

# Acknowledgements

The success of the presented work wouldn't have been possible without the help and support of many people, whom I would like to thank:

- First of all I would like to thank Prof. Markus K. Oberthaler for giving me the possibility to participate to the exciting field of atom optics, for his guidance and his support. I also would like to thank him for his trust and faith in me and for allowing me to think, work, and decide on my own. Furthermore, I am deeply grateful for all the discussions, not only concerning physics, the great time I had in his group, and the deep insight I gained into the fundamentals of physics during my time in his group.
- I also would like to thank Thomas Gasenzer for all the discussions, his support and for writing the joint report.
- My special thanks go to my former coworker Michael Albiez, who was initially the driving force behind the experiments. Together we spent a lot of time in the lab and with discussion and with his energy and enthusiasm we managed to successfully implement our ideas experimentally. Even though he had much more experience in the lab, we worked as a team and shared all the good but also the more difficult times during my first year.
- I thank Jonas Fölling for his contribution to the experiments and for all the fun we had not only in the lab, but also in the breaks and at the conferences. I learned a lot from him, as he usually knew to ask the right questions.
- Without Börge Hemmerling the second part of the experiments wouldn't have been possible (and I probably would have starved in the lab). Together we managed to do an incredible amount of work and succeeded in realizing the experiments. With his dedication and his passion he made it possible to get more out of the experiments than what we expected. I also enjoyed his way of seeing and understanding things, which enriched my time and pushed me forward.
- Stefan Hunsmann helped in the initial phase of building up the experiment. At this time we tried to understand the physics behind and thus had discussions all the time. His work and his ideas were very important for our later work.
- When I think back to the time Matteo Christiani was working in our lab I always have to smile. We had a great time and some of his ideas were irreplaceable for our experiments.
- Our 'Hiwis' Jan Krieger, Michael Scherer, and Enrico Vogt contributed a lot to the success of the experiments as well. Their work was focused on problems we had to solve but couldn't spare time for.
- I am also deeply grateful that Jerome Esteve joined our group. The numerous discussions we had, helped me to understand the underlying physical principles and I gained a very different, more fundamental view on the theoretical background. He thought me not to stop asking questions, even if I think I have the answer.
- Furthermore, I would like to thank Tom Bergeman and David Ananikian, as only with their contribution we were able to interpret our finite temperature measurements. I will always remember the discussions we had and the time we could spend together.

- My thanks also go to Andrea Trombettoni, who visited our group several times and gave us new insight into the theoretical description and the underlying physics.
- I am also deeply grateful to Prof. Yuri Kivshar, Elena Ostrovskaya, Chaohong Lee and Tristram Alexander, who I was allowed to visit in Australia. They shared their knowledge with me and supported me in solving and understanding theoretical problems, which I couldn't solve before.
- I also thank Prof. Peter Schmelcher for the many fascinating discussions during which I always learned a lot.
- I would like to thank Bernd Eiermann and Thomas Anker for the great time we had together, their advice, their patience while explaining the details of the setup, and for sharing their knowledge.
- Timo Ottenstein, Jens Appmeiner, Andreas Weller and Christian Gross I thank for the great atmosphere and the fun during the final part of my work.
- I also would like to mention our coworkers from the *Argon* experiment, Ralf Stützle, Lisa Kierig, Thomas Hörner, Ramona Ettig, Ute Schnorrberger, and Martin Göbel who contributed to the great time and the fun in the group.
- The members, who joined our group just recently I also would like to thank for the great atmosphere and all the discussion and help, Karsten Joho, Marc Repp, Arne Schietinger, Tobias Schuster, Jiri Tomkovic, Stefan Weis, Joachim Welte, and Tilman Zibold.
- Finally I would like to thank the Landesgraduiertenförderung Baden-Württemberg for the financial support and the Kirchhoff-Institut für Physik for providing an excellent professional environment for our research.